The Electron-Phonon Interaction in GaAs/(AlGa)As Quantum Wells

Andrew John Cross

Submitted to the
Faculty of Science, University of Nottingham
for the Degree of
Doctor of Philosophy (PhD)

May 2001

Acknowledgements

I would like to take the opportunity to mention the following people who have contributed in some way to this thesis.

Firstly my supervisor, Dr Tony Kent, for his invaluable guidance and unquestionable enthusiasm for the work. To my colleagues in the Phonon Imaging Group at Nottingham (1995-1998) for providing an enjoyable working atmosphere and no shortage of assistance with experiments: Phil Hawker, Andy Naylor, Alasdair Pentland, Stuart Cavill and Nicola Stanton.

I am grateful to Dietmar Lehmann (Institut für Theoretische Physik, Technische Universität, Dresden) and Wojtek Gancza (Institute of Theoretical Physics, University of Wroclaw) for helpful theoretical discussions.

To the Engineering and Physical Sciences Research Council (EPSRC) for funding my PhD research studentship.

Finally and most importantly, my sincere thanks go to all whose encouragement has led to the completion of this work, in particular to my family, and especially for the support and assistance of my wife Michelle.

Abstract

This thesis presents a study of the electron-phonon interaction in two dimensional electron gases (2DEGs), by measuring of the acoustic phonon emission from a sequence of *n*-type doped GaAs/(AlGa)As quantum wells.

Previous studies of emission from 2DEGs confined in GaAs heterojunctions (Chin *et al.*, 1984) have shown a surprising absence of longitudinal acoustic (LA) mode phonon emission, in contrast with theoretical studies (Vass, 1987) which predict that deformation potential coupled LA mode emission should dominate the energy relaxation processes. This may be attributed to the finite width of the quasi-2D sheet, which imposes a restriction on the maximum emitted phonon wavevector component perpendicular to the 2DEG, leading to a suppression of the emission (the "$1/a_0$ cutoff") at smaller phonon wavevectors than predicted by the earlier theory.

By using the quantum well width w as a means of modulating the thickness of the 2DEG, the dependence of the $1/a_0$ cutoff on the phonon emission can be directly measured. In the present work, significant LA phonon emission from the quantum well samples is observed.

To complement the experimental measurements, the theory of emission from a 2DEG has been modelled in detail using computer simulation techniques. Calculations of the electron-phonon interaction, including matrix element anisotropy and dynamic screening, as well as phonon focusing effects, can be combined to produce accurate predictions of the experimentally detected phonon emission energy spectra.

Chapter 1

Introduction

1 Introduction

1.1 Introduction and Overview

Over the past twenty years, the electron-phonon interaction has attracted a great deal of theoretical and experimental interest in the field of low-dimensional semiconductor physics. Below the temperature of liquid helium (4.2K), the dominant mechanism by which the energy relaxation of excited electrons occurs is the emission of acoustic phonons. At room temperature, phonon scattering limits the 2D mobility of electrons and holes in semiconductors. Studies of the electron-phonon interaction in these systems therefore provide much useful data about the limiting performance of manufactured devices based upon such technology.

1.2 Acoustic Phonons

Acoustic phonons are lattice vibrations travelling at the speed of sound, in the frequency range GHz to THz, and exist in two "modes", differentiated by the polarisation of the lattice vibration energy. The longitudinal acoustic (LA) mode causes lattice site displacement along the propagation direction, whereas the transverse acoustic (TA) mode produces displacement perpendicular to the direction of propagation. Since there are two directions perpendicular to the direction of the phonon wavevector q, two such modes, called the fast (FT) and slow (ST) transverse modes, exist. In high symmetry crystal orientation directions and isotropic media, however, these two modes are degenerate.

In the present work, acoustic phonon emission experiments are performed to measure the energy relaxation rate of hot electrons in a two-dimensional electron gas (2DEG). By studying the relative channelling of phonon energy into the two modes, an insight into the electron-phonon coupling mechanisms is obtained. LA mode phonons couple to electrons primarily through the deformation potential (DP), while TA modes favour the

piezoelectric (PZ) interaction. At higher temperatures, optic phonon emission takes over as the dominant energy relaxation mechanism.

1.3 Measurement of Energy Relaxation Rate in 2DEG systems

To determine the overall electron energy relaxation rate from a two dimensional electron gas (2DEG) system, it is necessary to be able to accurately determine the equilibrium electron temperature T_e resulting from a response to an input power P_e. This temperature may be determined from the carrier mobility and applied electric field by:

$$e\mu E_{SD}{}^2 = \frac{P_e(T_e)}{N_s} \tag{1.1}$$

where: μ = electron mobility, E_{SD} = source-drain electric field.

In addition to phonon emission studies, a number of other methods have been employed to measure the electron temperature, and thus energy relaxation rate, in low-temperature semiconductor systems. An early experiment by Fang and Fowler (1970) used the temperature dependence of the electron mobility in the *n*-inversion layer of a Silicon MOSFET as a method of determining electron temperatures at low electron concentrations.

Broadband Far Infra-red (FIR) emission has also been used (Hopfel *et al.*, 1984, Akimov *et al.*,1991) to determine the electron temperatures and energy relaxation rates in Silicon MOSFETs. High purity *n*-type GaAs detectors are used to measure the emitted FIR radiation; by comparing the emitted spectrum with that of an ideal Planckian emitter, an estimate of T_e is obtained. The Hopfel group obtained a $P \sim T_e^4$ dependence in the temperature range $8K < T_e < 25K$, while the Akimov group found a dependence of $P \sim T_e^2$ in the $20K < T_e < 50K$ temperature range. In each case the experimental data does not show good agreement with later theoretical calculations of the relaxation rate. (*Figure 1.1*, from Kent, 1998)

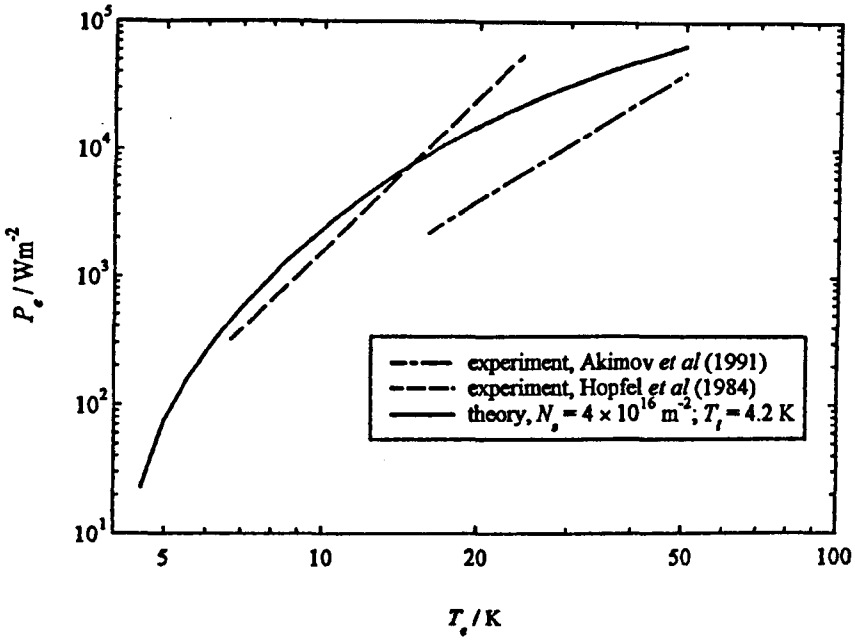

Figure 1.1: Far Infra-red measurements of the electron energy relaxation rate, compared to theoretical calculations.

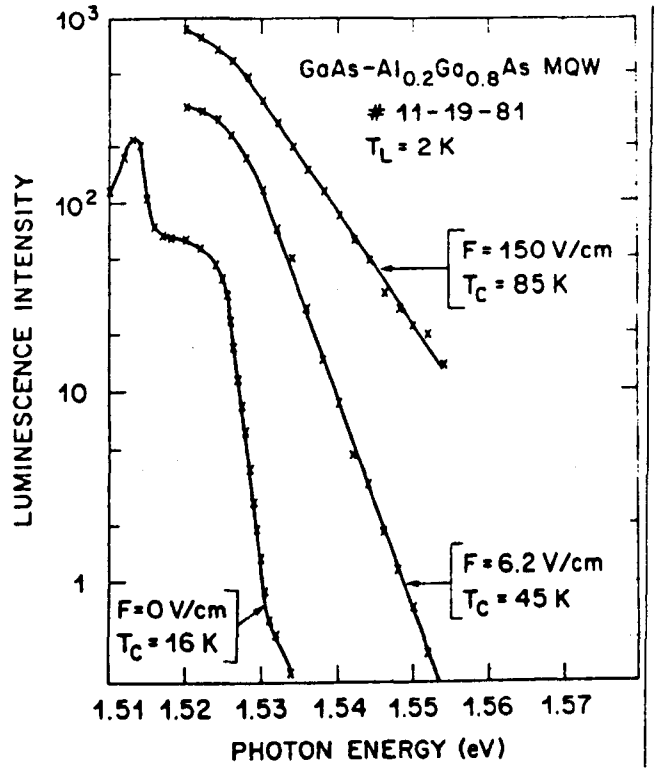

Figure 1.2: Photoluminescence measured as a function of incident photon energy. The carrier temperature is derived from the slope of the linear graph region.

Steady-state photoluminescence spectroscopy (Shah *et al.*, 1983; Balkan *et al.*, 1989) has been used to measure the electron temperature in GaAs/(AlGa)As quantum wells. A 2DEG is excited by a continuous-wave (cw) infra-red dye laser (input power ~ 2mW) . When the photoexcited carriers recombine, a spectrum of luminescence is emitted. For incident photon energies $h\upsilon > E_g + E_F$ (where E_F = Fermi energy, E_g = bandgap energy), the logarithm of the luminescent intensity falls linearly with increasing photon energy. The slope of this part of the spectrum gives the carrier temperature (*Figure 1.2*, from Shah *et al.*, 1983). This technique is most useful for carrier temperatures T_e > 20K, the upper part of the acoustic emission regime. Due to spectral line-broadening effects, the luminous intensity of the emitted radiation is too weak to be used to measure lower electron temperatures.

1.4 Direct Phonon Measurements

Direct phonon measurements offer a number of advantages over the methods discussed above, in that details of the phonon modes, frequencies and angles of the emitted phonons may be experimentally obtained. With a greater quantity of observable data, such methods are therefore able to provide a better test for theoretical models of the electron-phonon interaction.

The heat pulse technique was developed by von Gutfeld and Nethercot (1964) as a means of directly studying the time-of-flight spectra of ballistically propagated phonons. A 2DEG is excited by a short electrical pulse, with electrons in the 2D layer relaxing their energy through the emission of non-equilibrium acoustic phonons. These phonons propagate ballistically to the opposite face of the crystal, where they can be detected by means of a superconducting tunnel junction or thin film bolometer.

Tunnel junctions consist of two superconducting films, about 150nm thick, separated by a thin oxide layer, creating a voltage and energy gap which

must be traversed by incident phonons. Such a detector allows frequency-selective phonon detection to a resolution of a few MHz at a base operating frequency of ~200GHz. Superconducting bolometers allow for highly sensitive, non frequency-selective phonon detection. With the experimental system balanced at the transition temperature of the bolometer, incident phonons cause a localised warming effect that corresponds to an obervable increase in the bolometer resistance.

Both tunnel junctions and bolometers have a fast response time, so by choosing a sufficiently short pulse width, typically shorter than 100ns, (dependent upon the crystal thickness) the different phonon modes (longitudinal, fast and slow transverse) are separately resolved. The ratio of LA to TA modes in the time-of-flight spectra enable deductions to be made regarding the relative strength of the electron-phonon coupling mechanisms. By positioning the detector at different locations on the crystal face, or using an array of detectors, the angular distribution of emitted phonons may also be investigated.

The advent of modulation doping techniques for device fabrication, resulting in improved low-temperature electron mobilities, enabled the first measurements of the energy relaxation rate of a heated 2DEG using the heat-pulse technique to be made by Chin *et al.* (1984). A superconducting aluminium bolometer with transition point $T \sim 1.5$K was used to detect the phonon emission from a 2DEG GaAs/(AlGa)As heterojunction, grown on a 0.5mm-thick (100) GaAs semi-insulating substrate. The bolometer was positioned directly opposite the 0.1mm^2 2DEG device, which was heated with short electrical pulses of 0.03mW to 2.5mW power. *Figure 1.3* shows that at low powers, a single peak was seen, corresponding to the flight time of transverse acoustic (TA) phonons, while at higher input powers, a broad, slow pulse followed the transverse peak, attributed to rapidly decaying longitudinal optic (LO) mode phonons. No signal was observed at the flight time expected to correspond to longitudinal acoustic (LA) mode emission.

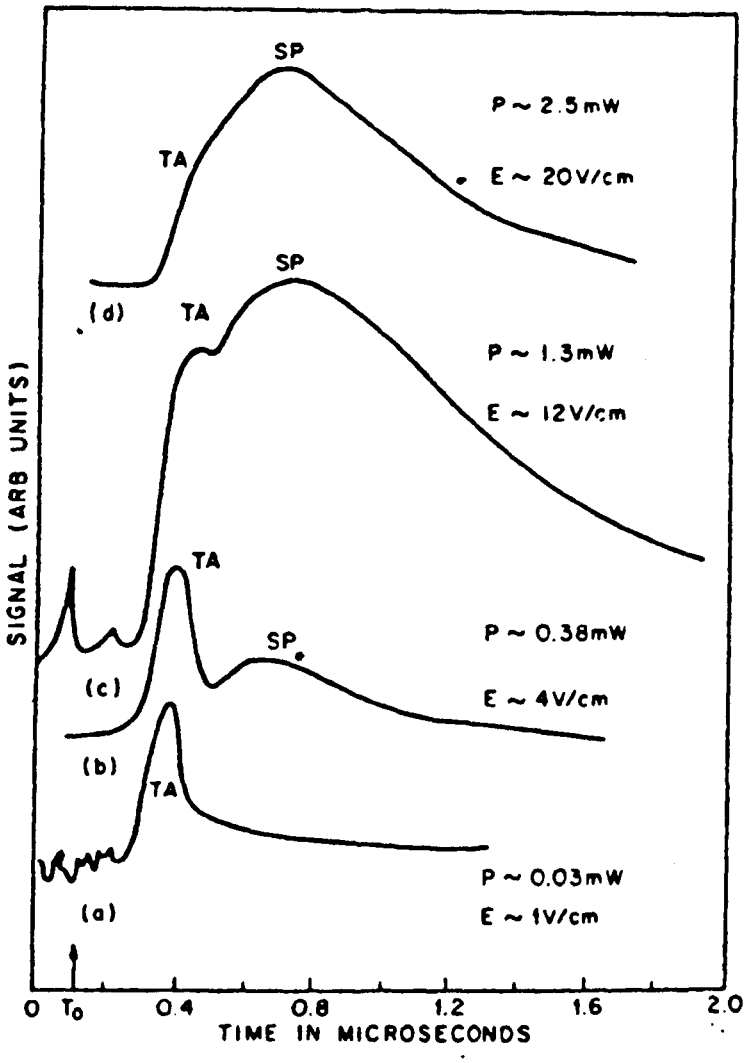

Figure 1.3: Time-of-flight phonon spectra obtained by Chin *et al.* (1984). At low powers a peak corresponding to transverse phonons is observed. As the power is increased, a broad, slow pulse appears, attributed to LO phonons.

The lack of an LA emission peak contrasts strongly with theoretical models (e.g. Vass, 1987) that predict dominant LA emission in the region $5K < T_e < 50K$, due to strong deformation potential coupling. The deformation potential coupling strength varies proportionally with the phonon wavevector q (and thus energy $h\omega = hq/v$), whereas the piezoelectric interaction varies as q^{-1}.

A number of other heat-pulse studies of phonon emission from 2DEGs (e.g. Rothenfusser *et al.*, 1986, Hawker *et al.*, 1992) followed the initial experiment of the Chin group, again observing little or no LA mode emission.

Hawker *et al.* offered an initial explanation for the lack of LA response in terms of phonon focusing effects. Phonon focusing (Taylor *et al.*, 1969) describes the phenomenon by which phonon energy is preferentially channelled along certain axes of high crystal symmetry in a anisotropic medium. This arises due to the non-collinearity of the phase velocity (wavevector) and group velocity (energy) directions of emitted phonons in such media. Moreover, longitudinal and transverse phonon modes are focused in different crystal directions, so that the relative height of the LA and TA peaks in the phonon time-of-flight spectra becomes a function not only of the relative power emitted into these modes at source, but also of the focusing effect. Monte-Carlo theoretical simulations of phonon focusing (Gancza and Paskiewicz, 1995) allow a phonon flux enhancement factor to be calculated for each mode.

For a small area, comparable in size to a typical experimental phonon detector, positioned directly opposite the source, an isotropic distribution of phonons emitted from a 2D layer in the (100) plane of GaAs results in a focusing enhancement factor of approximately 11:1 in favour of the TA mode; however, this is still unable to sufficiently account for the size of the discrepancy between the theoretical and experimental observations of the LA mode intensity.

An alternative explanation for the missing longitudinal mode can be formed in terms of momentum conservation requirements in the plane perpendicular to the 2DEG. Applying momentum conservation rules to the 2DEG plane gives rise to the well-known "$2k_F$ cutoff" (see e.g. Toombs *et al.*, 1987), imposing a maximum wavevector for an emitted phonon, equivalent to scattering from a point on the Fermi circle to a diametrically opposite position. By applying the same principles to the perpendicular plane, a "$1/a_0$" cutoff is obtained, where a_0 is the Fang-Howard parameter, a measure of the effective 2DEG "thickness".

Heat-pulse experiments were performed by Strickland *et al.* (1994) to investigate the $1/a_0$ cutoff, by measuring the phonon emission from two-dimensional hole gases (2DHGs) in GaAs/(AlGa)As heterojunction devices. Due to the greater effective mass of holes compared to electrons, the a_0 parameter is shorter: Walukiewicz (1988) gives a_0 (2DHG) = 2nm, compared to a_0 (2DEG) = 5nm (Ando *et al.*, 1982). The cutoff was therefore expected to be less severe for a 2DHG than for a comparable 2DEG. The experiments did indeed show an observable signal at the flight time corresponding to LA mode phonon emission.

It was further shown that the difference between results obtained for two similar 2DHGs grown in the (100) and (311)A crystal planes respectively could be explained by Monte-Carlo focusing predictions.

A further heat-pulse study of the $1/a_0$ cutoff was carried out by Hawker *et al.* (1995, 1996), using 2DEG GaAs/(AlGa)As quantum wells. In the first experiment, a quantum well of width 20nm, having two occupied electron subbands was used. Significant longitudinal mode emission was observed (*Figure 1.4)* at a bolometer positioned at an angle of 45° to the 2DEG normal. This LA emission was attributed to intersubband transitions. The second experiment used quantum wells of widths 5nm and 10nm, with a single

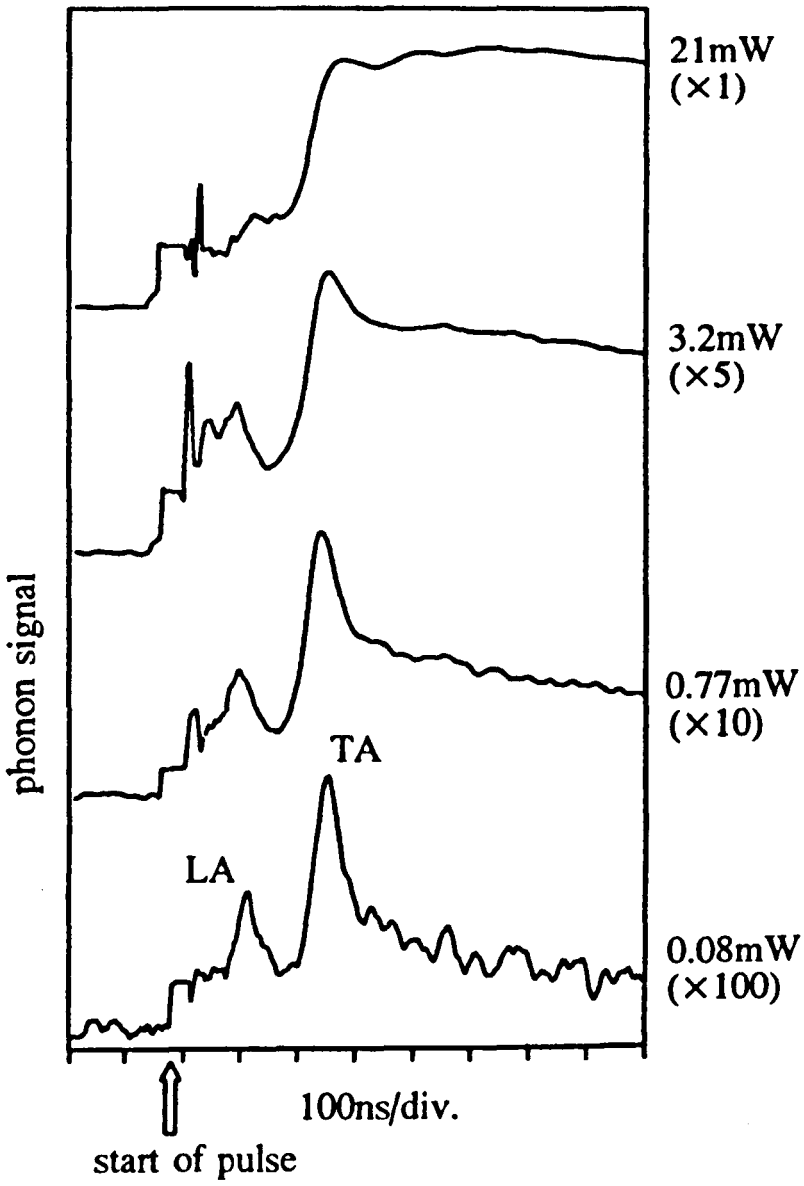

Figure 1.4: Both longitudinal and transverse phonons were observed by Hawker *et al.* (1995) in a study of phonon emission from a 2DEG quantum well.

subband occupied by electrons. The 2D areal density of the devices was $1.6x10^{16}m^{-2}$ and $1.8x10^{16}m^{-2}$ for the 5nm and 10nm wells respectively. A single bolometer was used to detect the emitted phonons, positioned at an angle of 50° to the 2DEG normal. Unlike the heterojunction cases discussed above, it was found that LA mode emission was significant for both wells. This can be attributed to the stronger electron confinement in a square quantum well compared to an equivalent width triangular-well heterojunctions. The choice of bolometer angle coincides with a focusing direction for LA phonons (and defocusing direction for TA), which also contributes to the strong longitudinal response. The proportion of LA emission was found to be stronger for the narrower well, due to the weaker $1/a_0$ cutoff for this device.

This thesis presents a comprehensive study of the "missing LA mode" effect, through a systematic investigation of the acoustic phonon emission from heated GaAs/(AlGa)As *n*-type single quantum well devices. By varying the quantum well width parameter, the effective 2DEG thickness a_0 can be modulated to a degree not seen in previous experimental studies.

A sequence of five different well widths, from 3nm to 15nm are used in the study, having similar transport characteristics (2D areal density and electron mobility). The wider wells (12nm and 15nm) have a 2DEG thickness similar to the "effective" 2DEG width, $3a_0$, of a GaAs heterojunction. The specific effect of the different form factors of heterojunctions and quantum wells may therefore be investigated. The samples have a lower electron density ($N_s \sim 2x10^{15}m^{-2}$) than those used by the Hawker group, so it follows that the $2k_F$ cutoff of emission in the 2DEG plane is therefore more severe in these devices, since $k_F = (2\pi N_s)^{1/2}$. Emission at angles close to the 2DEG normal is thus increased, further enhancing the dependence of emission on electron confinement.

Additionally, the emission is studied at three angles normal to the 2DEG: 0, 14 and 27 degrees. In these directions, the LA mode is not as strongly focused as at the wider angle bolometers used by Hawker *et al.* Any longitudinal response observed will therefore be due to dominant deformation potential-coupled emission.

1.5 Summary

Previous studies of two dimensional carrier gases (2DEGs and 2DHGs) have provided much valuable detail on the physical processes of the energy relaxation mechanisms of hot electrons. The work of Strickland (1996) and Hawker (1995) on 2DHG heterojunctions and 2DEG quantum wells respectively, have indicated that reducing the effective "thickness" of the 2D sheet results in a lifting of the suppression of the deformation potential coupled emission of LA phonons.

This thesis experimentally investigates the effect of the 2D sheet thickness on phonon emission, in a thorough and systematic manner, using a sequence of quantum well widths to vary the $1/a_0$ cutoff strength. A detailed theoretical model has been developed in parallel to the experimental work, implemented as a PC computer simulation; the predictions of the model agree well with the experimental results obtained.

It is shown that as the quantum well width is narrowed, deformation-potential coupled LA phonon emission becomes increasingly dominant. The energy loss rate at which the acoustic-optic phonon emission crossover occurs is also found to increase for narrower wells; it is argued that the weakening of the $1/a_0$ effect causes new pathways to become available for acoustic emission.

Chapter 2

Theory

2 Theory

2.1 Introduction

In this chapter, I shall discuss several important theoretical aspects of ballistic phonon spectroscopy in two dimensional electron gases (2DEGs).

The propagation of thermal phonons through a GaAs crystal medium at liquid helium temperatures is outlined and a full treatment of the electron-phonon interaction in 2D systems follows.

An understanding of the effects of the lattice dynamics of Gallium Arsenide is highly important, as the effects of elastic anisotropy of the medium strongly affect both the electron-phonon coupling matrix elements and the propagation of phonon energy through the crystal lattice; as such, this topic is considered in some depth before the main discussion of the electron-phonon system.

The chapter concludes with a description of an approach taken to develop a complete computer-modelled simulation of the electron-phonon system, suitable for making predictions of the expected experimental observations of phonon emission from GaAs 2DEGs. Detailed numerical calculations of the 2D electron system are presented in the following chapter.

2.2 Properties of Two Dimensional Electron Gases

2.2.1 Two Dimensional Electron Gases in GaAs Quantum Wells

Two dimensional electron gases (2DEGs) are of considerable interest in the experimental study of the energy relaxation of hot electrons in semiconductors; such a system can be well approximated using the simple model of a flat, conducting sheet of non-interacting Fermi particles, the physics of which is well known and described.

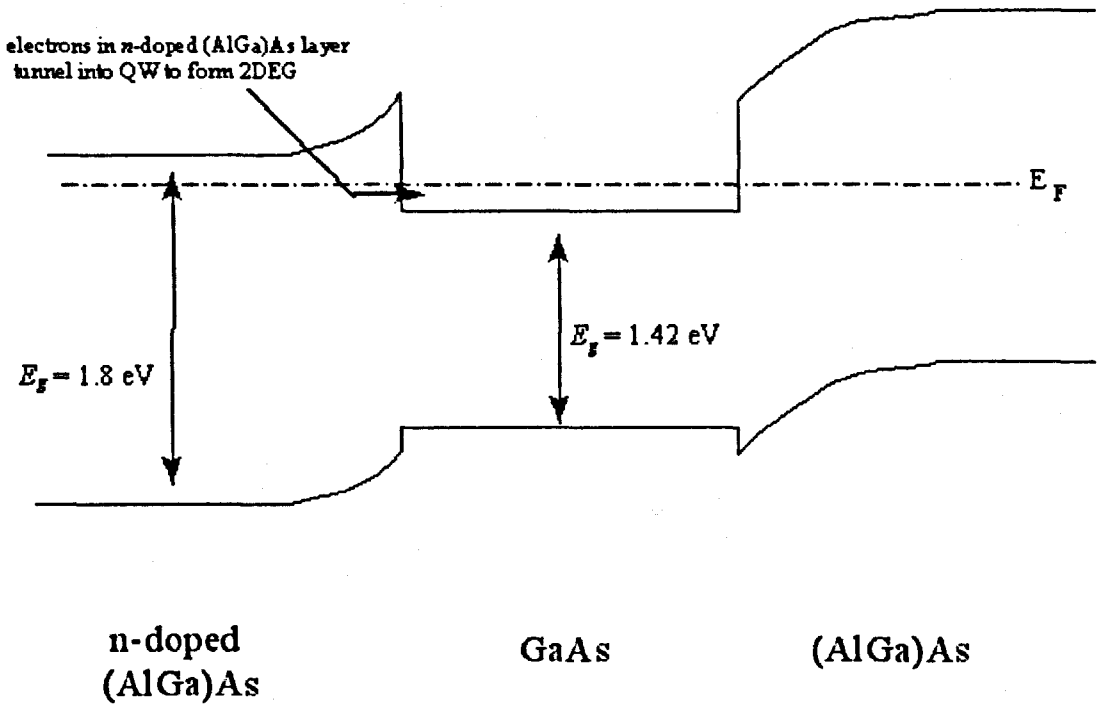

Figure 2.1: Formation of 2DEG in GaAs/(AlGaAs) quantum well

A quasi-two dimensional electron gas may be formed on a GaAs substrate by depositing single atomic layers (or "monolayers") using the technique of molecular beam epitaxy (MBE). Due to the similarity of the lattice constants of GaAs and (AlGa)As, it is possible to grow a layer of AlGaAs on top of a GaAs layer, forming an single-atom thick interface between the two layers. Owing to the different band gaps of GaAs (1.42eV) and AlGaAs (1.8eV), a potential step forms at the interface, as shown in *Figure 2.1*. By "sandwiching" a layer of GaAs between two AlGaAs layers, one of which is doped *n*-type with Silicon, a square potential well is formed, into which carriers from the doped layer tunnel to produce a two-dimensional electron gas, the effective "thickness" of which is given by the width of the GaAs layer.

Applying simple quantum theory, this two dimensional sheet may be approximated to a free particle in a box, with dimensions $L_x \times L_y \times w$, where w is the quantum well width, and so $L_{x,y} >> w$, as in *Figure 2.2*.

Applying the time-independent Schrödinger equation to this system:

$$\frac{\hbar^2}{2m^*}\nabla^2\Psi + E\Psi = 0 \qquad (2.1)$$

Rearranging the above equation to obtain an expression in terms of the electron wavevector k:

$$\nabla^2\Psi + k^2\Psi = 0 \qquad (2.2)$$

where $k^2 = 2m^*E/\hbar^2$.

The three-dimensional electron wavefunction ψ can be written as a product of three single-dimensional wavefunctions ψ_x, ψ_y and ψ_z, yielding

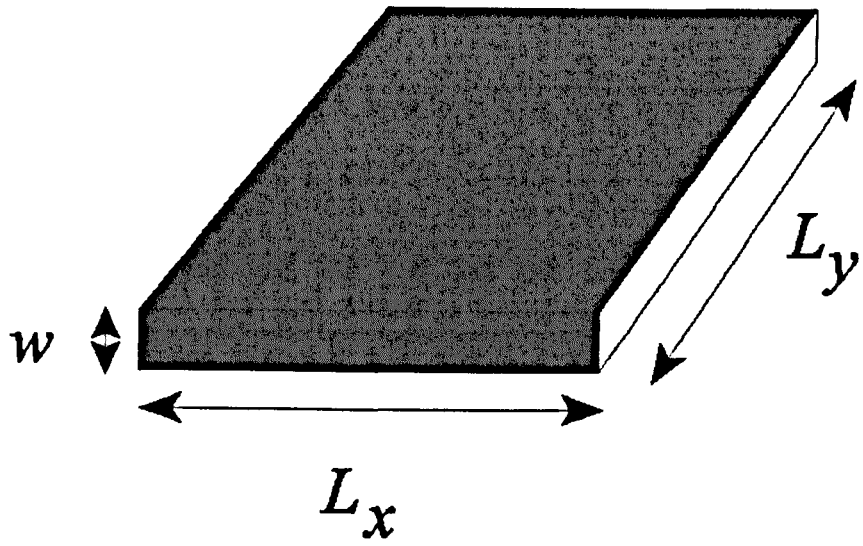

Figure 2.2: Representation of "2D" sheet as box with $w << L_{x,y}$

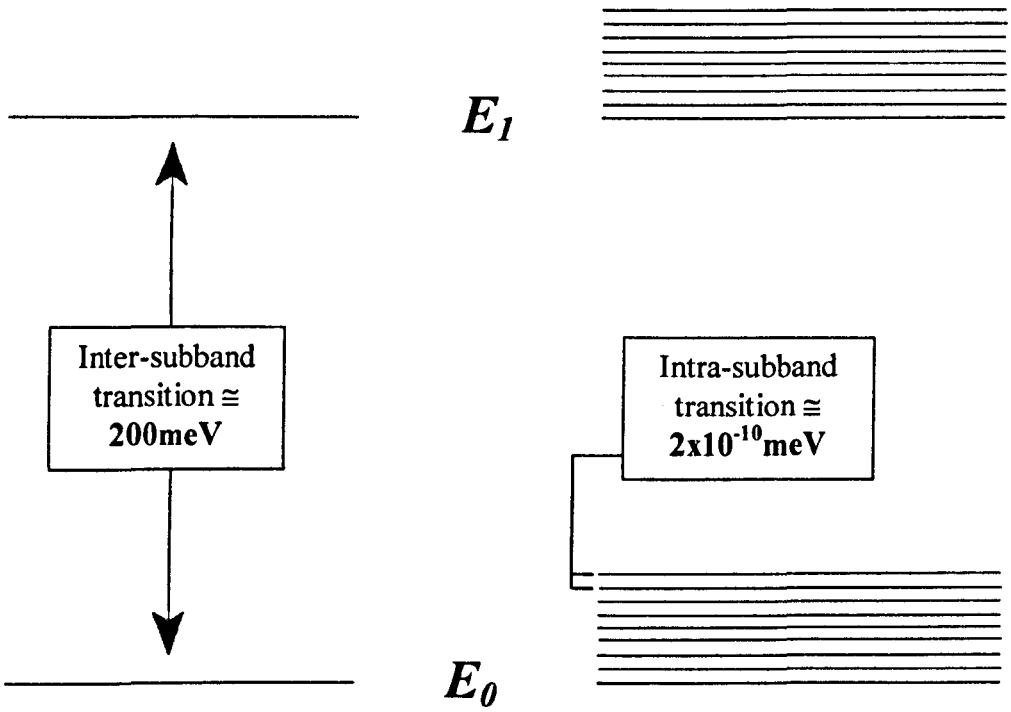

Figure 2.3: Inter- and intra-subband energy gaps for carriers confined within a two dimensional electron gas.

solutions for the wavevector components k_x, k_y, k_z, the single-dimensional wavefunctions taking the form:

$$\frac{d^2\Psi_x}{dx^2} + k_x{}^2\Psi_x = 0 \tag{2.3}$$

The generalised solutions for an infinite well are written as:

$$\Psi_x = A\sin(k_x x) + B\cos(k_x x) \tag{2.4}$$

To solve the above equations, the boundary conditions of the system are applied. Outside the walls of the box ($x < 0$, $x > L_x$) the wavefunction vanishes, i.e. $\Psi = 0$. At the edges of the box ($x = 0$ and $x = L_x$), the wavefunction ψ must be continuous.

Applying these conditions, the solutions $B = 0$ and $k_x L_x = l\pi$ (where l = 1,2,3..) are found. Similarly for the y- and z-directions, the expressions $k_y L_y = m\pi$ and $k_z w = n\pi$ are obtained.

The energy of the system may therefore be expressed as:

$$E = \frac{\hbar^2 k^2}{2m^*} = \frac{\hbar^2\pi^2}{2m^*}\left[\left(\frac{l}{L_x}\right)^2 + \left(\frac{m}{L_y}\right)^2 + \left(\frac{n}{w}\right)^2\right] \tag{2.5}$$

Considering, as an example, a quasi-2D GaAs sheet with dimensions L_x = L_y = 5mm, w = 5nm, and an electron effective mass, $m^* = 0.067m_0$, the separation between energy levels in the 2D plane is ~ $2\text{x}10^{-10}$meV, and perpendicular to the plane is ~ 200meV, as shown in *Figure 2.3*. By comparison, the thermal energy k_BT of a free electron at room temperature, 300K, is ~25meV, and at 50K, the thermal energy is ~4meV.

In the plane of the 2D sheet, therefore, the motion of the electrons is free, due to the narrow, continuum-like separation of energy levels ($k_B T >> \Delta E$), however, in the direction perpendicular to the GaAs/(AlGa)As interface, the motion is restricted by the "particle-in-a-box" bound states of the quantum well; carriers are confined to a single energy subband, as the separation between the energy levels is much greater, preventing thermal excitation of electrons between levels ($k_B T << \Delta E$). Such a system may, therefore, be considered as effectively two-dimensional with regard to electron transport.

Furthermore, at the low carrier temperatures and moderate carrier concentrations used in the experiments described in this work, it will be necessary only to consider electrons in the lowest (ground-state) subband, due to the negligible probability that a transition can occur between two discrete 2D subbands in such conditions.

For electrons confined in quantised subbands in the *z*-direction, but free to move in the *xy* plane, the normalised electron eigenfunctions are given by:

$$\Psi(r) = (L_x L_y)^{-1/2} \Psi_n(z) \exp(ik_x x) \exp(ik_y y) \qquad (2.6)$$

where $L_x L_y$ is the normalising area, $\Psi_n(z)$ are the set of electron wavefunctions describing motion in the *z*-direction for each occupied 2D subband, and a plane-wave solution has been assumed in the *x*- and *y*-directions.

The corresponding energy eigenvalues are then given by:

$$E = E_n + \frac{\hbar^2}{2m^*}\left(k_x^{\,2} + k_y^{\,2}\right) \qquad (2.7)$$

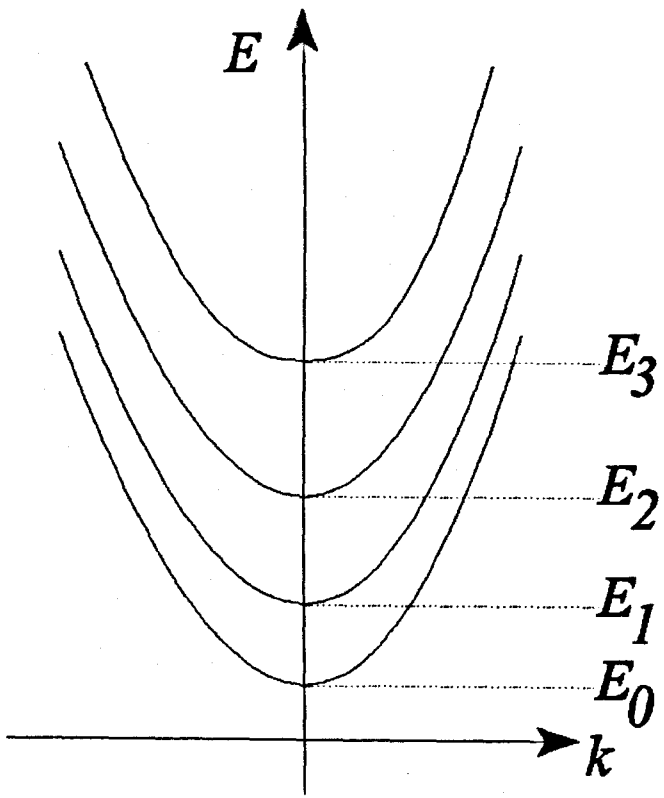

Figure 2.4: Energy levels for the first four energy subbands of a 2DEG.

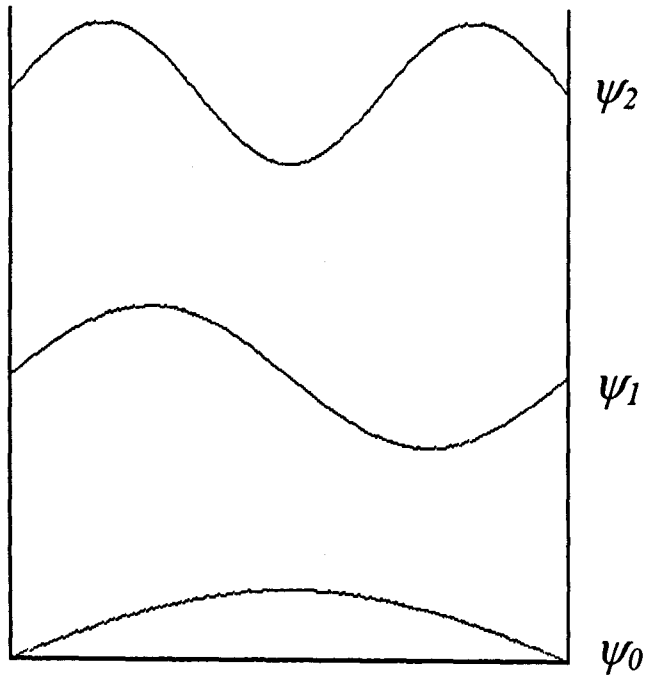

Figure 2.5: Electron wavefunctions in a infinite-height square potential well

where E_n is the base energy of the nth parabolic 2D sub-band, from *Equation 2.5*:

$$E_n = \frac{\hbar^2}{2m^*}\left(\frac{n\pi}{w}\right)^2 \qquad n = 1,2,3... \qquad (2.8)$$

Figure 2.4 shows these energy levels for a set of 2D subbands.

Substituting this solution for E_n into the Schrödinger equation, the resulting normalised electron wavefunctions for an infinitely deep square potential well, shown in *Figure 2.5,* are:

$$\Psi_n(z) = \sqrt{\frac{\pi}{w}}\sin\left(\frac{n\pi z}{w}\right) \qquad n = 1,2,3... \qquad (2.9)$$

In the finite-height potential well (FHPW) case, the electron wavefunctions may be expressed as: (Jasiukiewicz *et al.*, 1999)

$$\Psi_0(z) = A\exp\sqrt{\frac{2m_B^* V_B}{\hbar^2} - \frac{m_B^* k^2}{m^*}}\,z \qquad |z| > w/2 \qquad (2.10a)$$

$$\Psi_0(z) = B\cos kz \qquad |z| < w/2 \qquad (2.10b)$$

where k is the electron wavevector, m_B^* is the effective mass of the barrier material, V_B is the height of the potential step, and the normalised constants A and B are calculated by requiring that the electron wavefunction be continuous across the well barriers at $z = 0$ and $|z| = w/2$.

In *Equations 2.10a,b* above, it is acceptable, and for the purposes of numerical computation, particularly useful, to make the approximation $k \approx k_F$, where k_F is the Fermi wavevector of the electron distribution, as electrons at the Fermi energy dominate the conduction processes in 2DEGs, due to the proximity of filled and empty k-states.

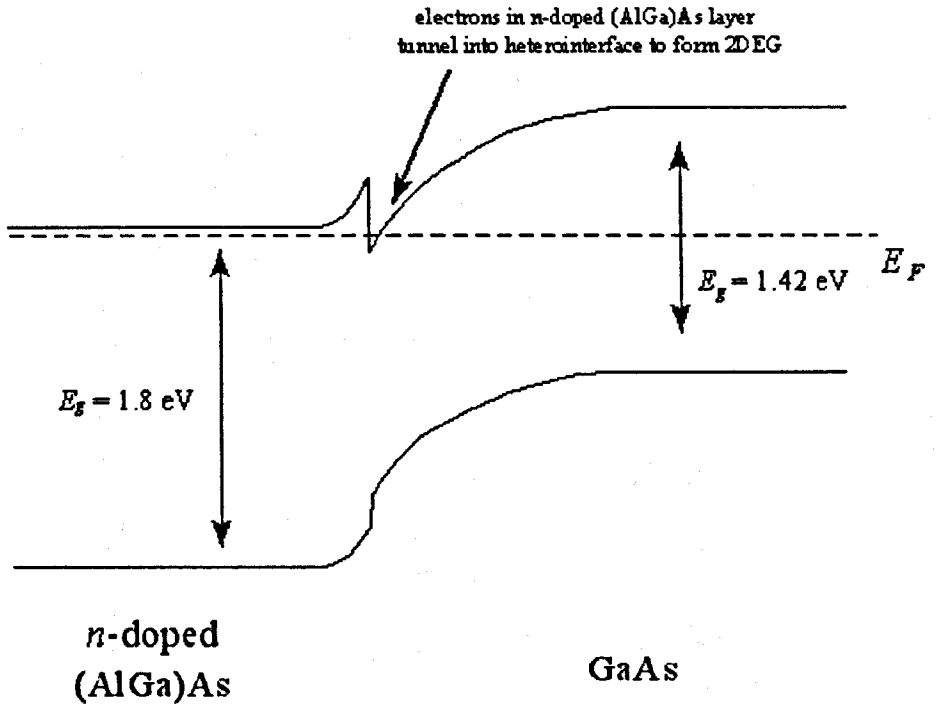

Figure 2.6: Formation of a 2DEG in a GaAs/(AlGa)As heterojunction

Comparison of the wavefunctions in the infinite-height (IHPW) and finite-height (FHPW) models shows that as the well width w is narrowed, the effect of the impingement of the electron wavefunction $\Psi_0(z)$ into the finite-height barrier material becomes increasingly significant, with a resultant reduction in the overall carrier confinement perpendicular to the 2D sheet.

2.2.2 Two Dimensional Electron Gases in GaAs Heterojunctions

Although experiments performed in the course of this work have used 2DEG quantum wells, the majority of earlier studies of the energy relaxation in 2DEGs has been performed using GaAs/(AlGa)As heterojunction-based devices, and so this system is briefly considered here, for the purpose of enabling comparisons to be made.

In a modulation-doped GaAs/(AlGa)As heterojunction, a triangular potential well forms at the interface of the GaAs and (AlGa)As layers, with the electron wavefunction not confined by a further potential step as in the quantum well case, instead extending out into the (AlGa)As layer, as shown in *Figure 2.6*. Consequently the carrier confinement is somewhat weaker than for a quantum well of similar MBE growth characteristics and layer structure, with the ground-state variational wavefunction given by:

$$\Psi_0(z) = \left(\frac{1}{2a_0^{\,3}}\right)^{1/2} z \exp\left(\frac{-z}{2a_0}\right) \tag{2.11}$$

a_0 is the Fang-Howard parameter, where $3a_0$ gives the average distance of electrons from the heterointerface.

2.2.3 2D Density of States

The 2D density of states in k-space, $D(E)$, is calculated by considering the number of k-states allowed between the energies E and $E + dE$:

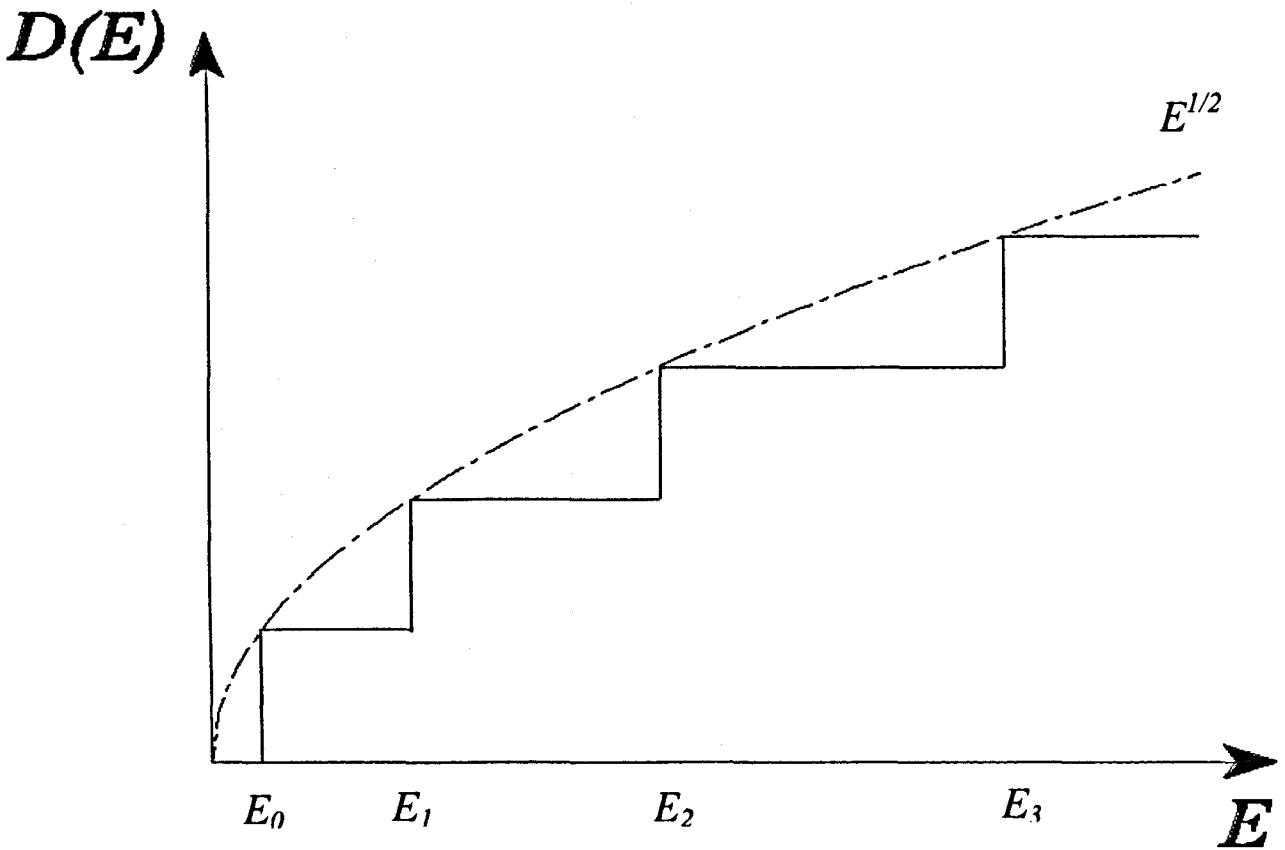

Figure 2.7: The two-dimensional density of states is independent of energy for a single occupied sub-band.

$$D(E)dE = D(k)dk = 2 \times \frac{1}{(2\pi)^2} \times 2\pi k dk \tag{2.12}$$

Making the acceptable assumption that the (100) GaAs 2DEG energy bands are parabolic :

$$E = \frac{\hbar^2 k^2}{2m^*} \tag{2.13}$$

the equation above yields:

$$D(E) = \frac{m^*}{\pi\hbar^2} \tag{2.14}$$

The density of states is therefore found to be independent of energy in the 2D regime, stepping up at subband edges only, as shown in *Figure 2.7*, rather than a continuous function of energy as in the 3D case.

The electron carrier density can therefore be expressed as:

$$N_s = D(E)E_F \tag{2.15}$$

since all k-states are filled up to the Fermi energy, to a good approximation at low temperatures. The Fermi surface, marking the boundary between filled and empty electron states in the 2DEG, is defined as a circle of radius k_F, given by:

$$k_F = (2\pi N_s)^{1/2} \tag{2.16}$$

2.3 Properties of phonons in semiconductors

2.3.1 Introduction

The conduction of heat in non-metallic solids takes place principally through the transport of thermal phonons. Acoustic phonons, which dominate these scattering processes at low temperatures, are lattice waves travelling at the speed of sound, with frequencies in the GHz/THz range. The maximum acoustic phonon frequency in GaAs is a few THz, at which the phonon wavelength equals twice the lattice constant. In the temperature regime of the experiments presented in this work, the Planckian peak in the phonon spectrum is well below this cutoff frequency.

Two types of acoustic phonon exist: a longitudinal (LA) mode causes particle displacement along the direction of propagation, whereas a transverse (TA) mode produces displacement perpendicular to the propagation direction, as shown in *Figure 2.8.*

In an anisotropic medium, two transverse modes exist, designated fast (FTA) and slow (STA) on account of their different averaged group velocities. These two modes are degenerate in an isotropic crystal, and in certain symmetry directions of anisotropic crystals, such as the (100) direction in GaAs, on which the devices used in the work presented here is based.

Optic phonon transport becomes dominant for higher temperatures (>50K). These phonons have very short lifetimes, decaying to large-wavevector acoustic modes.

2.3.2 Phonon Propagation at Liquid Helium Temperatures

At room temperature, ~ 300K, the mean free path of phonons in GaAs is very short, due to the high rate of inelastic scattering events. As the temperature of the system is lowered, thermal scattering becomes less

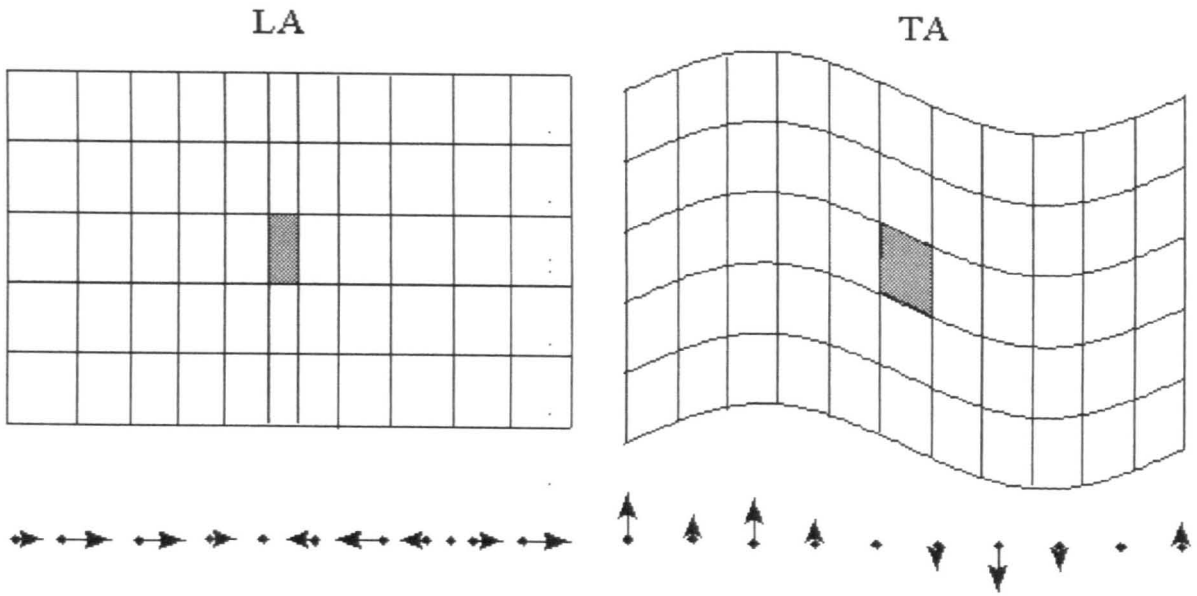

Figure 2.8: Phonon displacement directions due to compressional (LA) and shear (TA) stress

frequent, and a point is reached at which the mean free path becomes limited only by the crystal dimensions, owing to boundary scattering. In this regime, the phonon propagation is described as ballistic.

At liquid helium temperatures, ~4.2K and below, the contribution to scattering events from phonon-phonon interactions is negligible, and strong ballistic heat pulse signals corresponding to the phonon modes may be experimentally observed.

Phonons may, however, be elastically scattered from structural defects even at low temperatures.

2.3.3 Lattice Dynamics of Gallium Arsenide

2.3.3.1 Introduction

In considering the problem of an acoustic phonon travelling ballistically from a point source on one surface of a crystal to a detector on the opposite surface, the properties of the crystal lattice are of critical importance.

Firstly, the averaged sound velocities of longitudinal and transverse acoustic phonons in a crystal lattice are obtained directly from the elastic constants of the lattice. For cubic media, e.g. GaAs :

$$s_{LA} = \sqrt{\left[C_{11} + \frac{2}{5}(2C_{44} + C_{12} - C_{11})\right] / \rho} \qquad (2.18a)$$

$$s_{TA} = \sqrt{\left[C_{44} - \frac{1}{5}(2C_{44} + C_{12} - C_{11})\right] / \rho} \qquad (2.18b)$$

where $C_{11,12,44}$ are the three independent elastic constants in cubic media, and ρ is the crystal density.

With appropriate values for the elastic constants and density of GaAs, values of $s_{LA} = 5200\text{ms}^{-1}$ and $s_{TA} = 3300\text{ms}^{-1}$ are found.

The crystal lattice dynamics are also responsible for determining the nature of the angular and polarisation dependence of the phonon energy flux that is observed at the detector, given an initial uniform distribution of phonon wavevectors at the source.

In a perfectly isotropic medium, the acoustic phonon polarisation vectors are exactly parallel (LA mode) or perpendicular (TA modes) to the propagation direction. In a real crystal such as GaAs, however, particle displacement generally has components both along and perpendicular to the propagation direction, due to the elastic anisotropy of the medium. The resulting phonon polarisations therefore possess some of the character of both LA and TA modes, and so the resulting modes are described as being "quasi-longitudinal" and "quasi-transverse" respectively.

2.3.3.2 Phonon Focusing

A further significant consequence of the elastic anisotropy of real crystals is the preferential "channelling" of energy along certain symmetry directions of the crystal, known as phonon focusing.

In elastically anisotropic media, the phonon group velocity vector, v_g, associated with the direction of energy flow, and the phase velocity, v_p, which points in the direction of the phonon wavevector, are generally non-collinear. Consequently, when phonons are emitted from a source with a uniform angular distribution of wavevector directions, the energy flow will be enhanced in some directions, and decreased in others, with respect to the average value.

This effect was first observed, and the term "phonon focusing" used to describe it, by Taylor *et al.* (1969), who studied the time-of-flight phonon heat

pulse spectra obtained from the alkali halides LiF and KCl, for various crystallographic directions. The ratios of longitudinal to transverse acoustic phonon modes varied as the direction was changed. By altering the thickness of the samples, it was confirmed that this effect was not due to different attenuation coefficients for the modes as they propagated through the crystal. A phonon focusing enhancement factor, A, (Maris, 1971), was introduced, defining a ratio of the phonon intensity for various crystal directions to the intensity expected in an isotropic solid:

$$A \equiv \left| \frac{d\Omega_k}{d\Omega_v} \right| \tag{2.19}$$

where $d\Omega_k$ and $d\Omega_v$ are the respective solid angles in wavevector and group velocity space.

Figure 2.9 shows the phonon focusing pattern for longitudinal and transverse acoustic phonons emitted ballistically in an isotropic angular distribution, traversing a 380μm thick (100) GaAs wafer and being detected by a 800x800μm square detector plane situated on an opposite crystal face. The salient features observed in the images are the highly concentrated TA phonon flux close to the (100) direction, and the diffuse nature of the LA phonon flux, which peaks close to the (111) direction.

2.3.3.3 Calculation of the Angular and Polarisation Dependence of the Phonon Energy Flux

To determine the angular and polarisation dependence of the energy flux arriving at a spatial detector positioned on a crystal face opposite a source of phonons, continuum elasticity theory must be applied to the system.

Following the technique presented by Every (1979) for cubic crystals, to which the reader is directed for a detailed derivation of the equations that

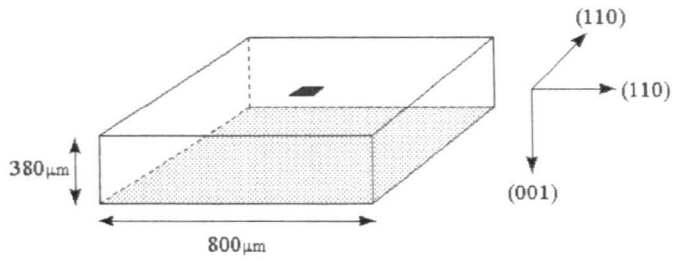

Figure 2.9: (100) focusing patterns for (a) isotropic LA and (b) isotropic TA phonon distributions

follow, the phonon polarisation and group velocity vectors are calculated in the framework of elastic waves.

In a non-piezoelectric crystal, the second-rank elastic stress, σ_{ij}, and strain, S_{lm}, tensors are related by a generalised form of Hooke's Law for small strains:

$$\sigma_{ij} = C_{ijlm} S_{lm} \tag{2.20}$$

where C_{ijlm} is the fourth-rank elastic modulus tensor. In a cubic crystal, there are only three independent components of the C_{ijlm} tensor:

$$C_{11} = C_{22} = C_{33}, \quad C_{12} = C_{13} = C_{23}, \quad C_{44} = C_{55} = C_{66} \tag{2.21}$$

In a piezoelectric medium, such as GaAs, a mechanical strain induces an electric polarisation, and similarly an applied electric field creates a strain in the crystal. This coupling of the elastic and electric variables requires that the generalised form of Hooke's Law above must be modified to account for the "stiffening" of the lattice due to the piezoelectric effect:

$$\sigma_{ij} = C_{ijlm} S_{lm} - e_{ijr} E_r = C'_{ijlm} S_{lm} \tag{2.22}$$

where C'_{ijlm} are the piezoelectrically stiffened elastic constants for the crystal.

In order to quantify the significance of this effect, Every and McCurdy (1987) defined a dimensionless electromechanical coupling constant K_{44} to determine the strength of the piezoelectric effect in cubic crystals:

$$K_{44} = \left(\frac{e_{14}^{\,2}}{\varepsilon_r \varepsilon_0 C_{44}^{\,E}} \right)^{1/2} \tag{2.23}$$

where e_{14} is the piezoelectric stress constant for the crystal, expressed in units of C/m^2, and C_{44}^{E} represents the elastic constant C_{44} as measured in zero electric field.

For GaAs, e_{14} = 0.166 C/m^2, giving K_{44} = 0.0609. Every and McCurdy show that piezoelectric stiffening only becomes a significant factor for K_{44} > 0.1, so it is reasonable to neglect such effects in the calculations presented in this work.

Two new parameters K_2, K_3 may be defined in terms of ratios of the elastic constants C_{11}, C_{12}, C_{44}:

$$K_2 = (C_{11} - C_{44}) / C_1 \tag{2.24}$$

$$K_3 = (C_{11} - C_{12} - 2C_{44}) / C_1) \tag{2.25}$$

$$\text{where } C_1 = C_{11} + 2C_{44} \tag{2.26}$$

In the K_2, K_3 representation, it is possible to construct a triangle of allowed values of K_2 and K_3, in which all crystals must lie, in order to ensure crystal stability. The case K_3 = 0 describes a system with perfectly isotropic behaviour.

By substituting plane-wave forms of the three phonon modes into the equation of motion for a crystal volume element, Christoffel's equation is obtained:

$$(D_{il} - v^2 \delta_{il}) \varepsilon = 0 \tag{2.27}$$

where

$$D_{il} = \frac{C_1}{\rho}\begin{pmatrix} K_2\hat{q}_1^{\,2} + \frac{1}{3}(1-K_2) & (K_2-K_3)\hat{q}_1\hat{q}_2 & (K_2-K_3)\hat{q}_1\hat{q}_3 \\ (K_2-K_3)\hat{q}_1\hat{q}_2 & K_2\hat{q}_2^{\,2} + \frac{1}{3}(1-K_2) & (K_2-K_3)\hat{q}_2\hat{q}_3 \\ (K_2-K_3)\hat{q}_1\hat{q}_3 & (K_2-K_3)\hat{q}_2\hat{q}_2 & K_2\hat{q}_3^{\,2} + \frac{1}{3}(1-K_2) \end{pmatrix} \tag{2.28}$$

is derived from the Christoffel tensor C_{ijlm}, obtained by the relation:

$$D_{il} = (1/\rho)C_{ijlm}n_j n_m \tag{2.29}$$

Equation 2.28 above shows that the system can be qualitatively described completely in terms of the K_2, K_3 parameters, with actual numerical values of the elastic constants (in the equation, represented by the C_1 term) required only for quantitative analysis.

Solving *Equation 2.27* by setting the determinant to zero, a cubic equation in $v_p^{\,2}$ is obtained, yielding three solutions, corresponding to the phonon phase velocity of each phonon mode (LA, STA, FTA).

The group velocity vectors for each mode are then obtained by:

$$v_g = \left(v_p - n.\frac{\delta v_p}{\delta n}\right)n + \frac{\delta v_p}{\delta n} \tag{2.30}$$

Every (1979) gives the solution for the ratios of the phonon polarisation vectors $\varepsilon_{i,\lambda}$ (i = crystallographic direction 1,2,3, λ = phonon mode: 0=LA, 1=STA, 2=FTA) :

$$\varepsilon_{i,\lambda} = \frac{\hat{q}_i}{T_\lambda - 3\hat{q}_i^{\,2}(K_3/K_2)} \tag{2.31}$$

where:

$$T_\lambda = 1 + 2(1 - aS)^{1/2} \cos(\psi + \frac{2}{3}\pi\lambda) \tag{2.32}$$

$$\psi = \cos^{-1}\left[\left(1 - \frac{3}{2}aS + bQ\right) / \left(1 - aS\right)^{3/2}\right] \tag{2.33}$$

$$a = 3\frac{K_3}{K_2}\left(2 - \frac{K_3}{K_2}\right) \tag{2.34}$$

$$b = \frac{27}{2}\frac{K_3^2}{K_2^2}\left(3 - 2\frac{K_3}{K_2}\right) \tag{2.35}$$

$$S = \hat{q}_1^{\,2}\hat{q}_2^{\,2} + \hat{q}_2^{\,2}\hat{q}_3^{\,2} + \hat{q}_3^{\,2}\hat{q}_1^{\,2} \tag{2.36}$$

$$Q = \hat{q}_1^{\,2}\hat{q}_2^{\,2}\hat{q}_3^{\,2} \tag{2.37}$$

2.3.3.4 Phonon Scattering

Any departure from ideal lattice periodicity will result in phonon scattering. Mechanisms for such events include scattering from structural defects and impurities, as well as from other phonons. In a well-grown MBE crystal, at low temperatures, the mean free path for phonon scattering from point defects and impurities becomes large with respect to typical crystal dimensions (~ 2mm x 2mm x 0.5mm) and so such scattering is reduced.

Variations in the isotopic mass of the crystal may also cause phonons to scatter: in an MBE-grown GaAs crystal, Gallium and Arsenic atoms exist in the form of several isotopes, randomly distributed through the crystal lattice. Such a deviation from ideal lattice periodicity causes localised changes in mass, elastic modulus and lattice constant, giving rise to an elastic scattering of phonons.

The rate of this isotope scattering is estimated in the Debye thermal conductivity approximation to vary as the fourth power of the phonon frequency, (Klemens, 1958) :

$$\tau^{-1} = A\upsilon^4 \tag{2.38}$$

where A is a material-dependent attenuation factor.

Using a value for A of $7.38\text{x}10^{-42}$ sec^3 for GaAs, (Tamura, 1984), a frequency q_c may be defined at which the contribution of isotope scattered attenuation becomes significant ($P_{scattered}(q_c) = P_0(q_c)/2$). For a 380μm thick wafer, $q_c \geq 1THz$, whereas for a 2mm thick wafer, $q_c \sim$ 700GHz. It is seen that these scattered phonons are predominantly found in the high energy tail of the acoustic phonon energy spectrum.

One other important mechanism to consider is that of scattering by Jahn-Teller ions (Cr^{3+}, Ni^{2+}) (Xin *et al.*, 1996). Although the density of such ions should be small in a well-grown GaAs crystal, the strongly frequency-resonant nature of the attenuation results in a quite significant effect. Broad frequency resonances are observed at $f \gtrsim 700\text{GHz}$, in the high-energy tail of the acoustic phonon emission spectrum.

A probability can be defined that ballistic phonons may be scattered before reaching the bolometer, undergoing down-conversion decay processes to lower energy phonons. Longitudinal (LA) phonons decay primarily by the route LA → TA + TA (where TA may be either a slow or fast transverse phonon). Fast transverse phonons most commonly decay by FTA → FTA + STA, while non-collinear decay of slow transverse phonons is rarely seen.

Down-conversion of modes may also occur as a result of optic phonon emission, which becomes the dominant energy relaxation process for electron temperatures of $T_e \cong 50K$ and above. Longitudinal optic phonons have a very short lifetime (Hawker *et al.* (1992) give a result of 3.3ps), converting rapidly to high-wavevector TA modes. These down-converted phonons appear as a broad, delayed, diffusive signal, arriving some time later than the ballistic transverse phonon pulse.

2.4 The Electron-Phonon Interaction

The theoretical study of the emission of acoustic phonons through the electron-phonon interaction has been considered in some depth by a number of authors (e.g. Vass, 1987; Vickers, 1992; Jasiukiewicz and Karpus, 1996; Kent, 1998), all of whom have employed an essentially similar technique, which will be used as the basis of the discussion below. Such theoretical analyses have, however, largely failed to explain certain features observed in experimental phonon emission studies, most notably the apparent absence of an LA phonon emission signal detectable using bolometers positioned directly opposite a (100) GaAs 2DEG heterojunction device.

Jasiukiewicz *et al.* (1999) argue that the inadequacies of the earlier theory can be attributed to the incorrect treatment of such factors as electrostatic screening of the interaction, coupling matrix element anisotropy, and the finite thickness of the 2D sheet, which were often simply neglected in earlier analyses. These terms are implicitly included in the treatment that follows, and the individual importance of each specific factor, as determined by numerical computations, will be discussed in depth in the following chapter.

2.4.1 Electron-Phonon Coupling Mechanisms

Two principal mechanisms account for electron-acoustic phonon scattering in GaAs crystals: the deformation potential, commonly abbreviated to DP, and the piezoelectric interaction (PZ). A "macroscopic deformation potential" (MDA) mechanism for the interaction, resulting from heterointerface vibrations, has been proposed by Vasko and Mitin (1995), but is predicted to be weak in comparison with ordinary DP coupling, and will not be considered here.

2.4.1.1 *Deformation Potential coupling*

In a 2DEG heterojunction or quantum well at moderate electron temperatures in the acoustic emission regime (5K < T_e < 50K), deformation potential coupling is the most efficient mechanism by which electrons interact with phonons.

If a crystal is disturbed by some applied strain, atomic motion is coupled to carriers through a periodic modulation of the lattice constant, causing a shift in the conduction and valence bands. This effective potential may induce electronic transitions.

For sufficiently small dilations, the energy shift has been shown to vary linearly with the magnitude of the dilation (Bardeen and Shockley, 1950):

$$V_{def} = E_d \Delta \tag{2.39}$$

In a (100) GaAs 2DEG heterojunction or quantum well, the conduction band can be approximated as parabolic, so that the three-dimensional dilation term is given by:

$$\Delta = \nabla . U \tag{2.40}$$

where U, the strain field due to a phonon q, λ is given by:

$$U(r) = \left(\frac{\hbar}{2\rho V \omega_{q,\lambda}} \right)^{1/2} \left(a_{q,\lambda} \exp(iq.r) + a^{+}_{q,\lambda} \exp(-iq.r) \right) \cdot \lambda \tag{2.41}$$

An expression for the deformation potential may therefore be written:

$$V_{def} = \left[\frac{\hbar E_d}{2\rho V \omega_q} \right] i(q.\varepsilon_q) \left[a_q \exp(iq.r) + a_q^{+} \exp(-iq.r) \right] \tag{2.42}$$

In an idealised, isotropic crystalline system, in which the longitudinal and transverse phonon polarisations are aligned directly parallel and perpendicular to the phonon wavevector, the scalar product term $q.\varepsilon_q$ evaluates to q in the case of the LA mode, and to zero for the TA mode. Transverse acoustic phonons are therefore forbidden from coupling to the deformation potential in the isotropic regime.

As discussed in 2.3.3.1 above, however, in a real, anisotropic crystal, the phonon polarisations are, in general, neither perfectly parallel nor perfectly perpendicular to the direction of propagation, and must instead be described as "quasi-LA" and "quasi-TA". As such, quasi-TA phonons, which have a small component of the polarisation directed along the phonon wavevector q, will couple weakly via the deformation potential.

Jasiukiewicz and Karpus (1996) modelled theoretically the anisotropy of the electron-phonon coupling matrix elements in 2DEGs, and their approach will be followed in the electron-phonon interaction calculation presented here.

2.4.1.2 Piezoelectric coupling

For crystals that possess a dipole moment, a second mechanism exists by which the electron-acoustic phonon interaction may occur.

In piezoelectric (PZ) coupling, the strain field of a phonon distorts the crystal lattice, which, in crystals lacking a centre of inversion symmetry axis (such as GaAs) produces an electric field that couples to the electrons.

The mechanical stress σ, mechanical strain e and electric field E are related by (Wixforth 1989, Hutson and White 1962)

$$\sigma_{ij} = C_{ijlm} e_{lm} - h_{ijk} E_k \tag{2.43}$$

where C_{ijlm} is the elasticity tensor, and h_{ijk} is the piezoelectric tensor, usually written in the reduced form h_{im} ($i,m = 1 \rightarrow 6$) due to symmetry.

For the zinc-blende GaAs cubic crystal structure, only shear strain components contribute to the piezoelectric tensor, and these components are all equal, $h_{14}=h_{25}=h_{36}$. Only one component of the piezoelectric tensor, h_{14}, is therefore required in writing an expression for the interaction potential.

The mechanical stress and strain are related to the lattice distortion by:

$$\nabla\sigma = \nabla^2 U \tag{2.44}$$

$$\nabla e = h\frac{\delta^2 U}{\delta t^2} \tag{2.45}$$

Finally an expression for the interaction potential may be written:

$$V_{piezo} = \left(\frac{h_{14}}{\varepsilon_0 \varepsilon(q)}\right)\frac{1}{q}\left(\frac{\hbar}{2\rho V \omega_{q,s}}\right)^{1/2}\left[a_{q,s}\exp(iq.r) + a_{q,s}^{+}\exp(-iq.r)\right]\varepsilon_{q,s} \tag{2.46}$$

In both isotropic and anisotropic media, both longitudinal and transverse phonons may couple to electrons through the piezoelectric interaction.

2.4.1.3 Screening of the Interaction Potentials

At low electron temperatures T_e, screening of the electron-phonon interaction by the free carriers of the two dimensional electron gas has the effect of reducing the energy relaxation rate, as the characteristic thermal phonon wavevector $q = \frac{k_B T_e}{\hbar}$ becomes smaller than the Thomas-Fermi screening radius, r_s.

Using the low-wavelength limit of the Lindhard formula for the dielectric function of free 2D electrons, the screening term $S_{q,\lambda}$ takes the form:

$$S_{q,\lambda} = \left(\frac{q_{//}}{q_s H + q_{//}} \right)^2 \tag{2.47}$$

where q_s is the inverse Debye screening length:

$$q_s = m^* e^2 / 2\pi\varepsilon\varepsilon_0\hbar^2 \approx 2 \times 10^8 m^{-1} \text{ for GaAs} \tag{2.48}$$

The H-factor is obtained by numerically integrating over the electron wavefunction:

$$H = \int dz' |\Psi_0(z')|^2 \int dz |\Psi_0(z)|^2 \exp(-q_{//}|z - z'|) \tag{2.49}$$

The effect of screening is clearly stronger at lower frequencies, acting to suppress low frequency phonon emission due to intra-level electronic transitions.

In systems with weak carrier confinement, such as bulk epilayers and, to a lesser extent, heterojunctions, the approximation $H = 1$ may be made, resulting in the quasi-static screening approximation given in the electron-phonon interaction treatment of Kent (1998). Such an approximation is useful in reducing the computation time required to numerically evaluate the full Lindhard screening of the interaction potentials. Its applicability to the experimental systems investigated in this work will be discussed further in Chapter 3.

For a more complete treatment of the screening of the electron-phonon interaction, incorporating many-body theory, the reader is referred to Jasiukiewicz *et al.* (1999). Such an approach has not been attempted in this

work, as a qualitative comparison of the results of the Jasiukiewicz group with those obtained using the dynamic Lindhard model in the present work (described in the following chapter) shows many similarities in the structures observed in the angular dependence of emission.

The Lindhard screening approximation is generally regarded as acceptable for the screening of the long-range piezoelectric interaction, however, in the case of the deformation potential, the inclusion of screening terms has been disputed. Walukiewicz (1988) argued that screening should not be included in the DP coupling calculation, owing to the short-range nature of the deformation potential.

Subsequent analysis, however, has suggested that screening must be taken into account for both DP and PZ-coupled emission. Gorczya and Krupski (1995) showed by measuring the temperature dependence of electron mobilities in GaAs/(AlGa)As heterostructures below 77K that the unscreened deformation potential model is insufficient to explain the shape of the mobility dependency curve obtained in their results; however, the use of the random phase approximation (RPA), of which the Thomas-Fermi model is a low-wavevector limit, gives good agreement, providing the deformation potential constant is increased from its bulk value of 7eV to an enhanced value of 12eV. The physical rationale behind such an increase in the deformation potential remains unexplained; Vickers (1992) shows that the total energy relaxation rate in 2DEG quantum wells can be modelled well with an unscreened deformation potential of 7eV. For consistency with other models that incorporate screening, however, the value of 12eV has been adopted in the present work.

The many-body deformation potential screening model employed by Jasiukiewicz *et al.* (1999) has shown good theoretical agreement with direct experimental phonon measurements made on 2DHGs by Strickland (1996) and on 2DEG QWs by Cross *et al.* (1999). Removing this screening term from the theoretical treatment, the angular distribution of emitted DP-coupled

phonons, as compared with experimental results is found to be incorrect. It is, therefore, the opinion of this author that the Lindhard model described above is equally applicable to the deformation potential, provided an enhanced interaction constant E_d= 12 eV is used.

2.4.2 Basic Equations of the Electron-Phonon Interaction

The two-dimensional electron gas under consideration is assumed to exhibit the behaviour of a perfect Fermi gas of non-interacting particles in thermal equilibrium.

The Fermi energy is given by the parabolic dispersion relationship:

$$E_F = \frac{\hbar^2 k_F^{\,2}}{2m^*} \tag{2.50}$$

where k_F, the Fermi wavevector is $k_F = (2\pi N_s)^{1/2}$

All electron states are filled up to the Fermi energy, and empty thereafter, with the boundary between filled and empty states "smeared" over a region of $\approx k_B T$, as depicted in *Figure 2.10.*

The theoretical dynamics of the electron-phonon interaction are governed primarily by considerations of momentum and energy conservation, both in the plane of the 2DEG, and in the normal direction.

The relaxation of an excited electron, emitting a phonon, may be represented as a conservation process in momentum space:

$$\boldsymbol{k} = \boldsymbol{k}' + \boldsymbol{q} \tag{2.51a}$$

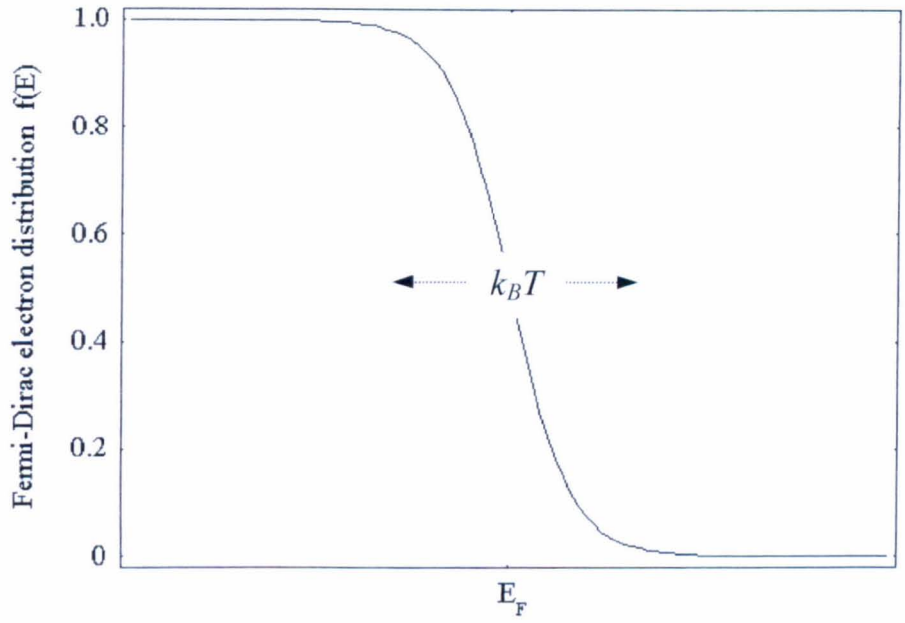

Figure 2.10: Occupied and empty electron states are separated by an energy $\sim k_BT$ at the Fermi energy E_F

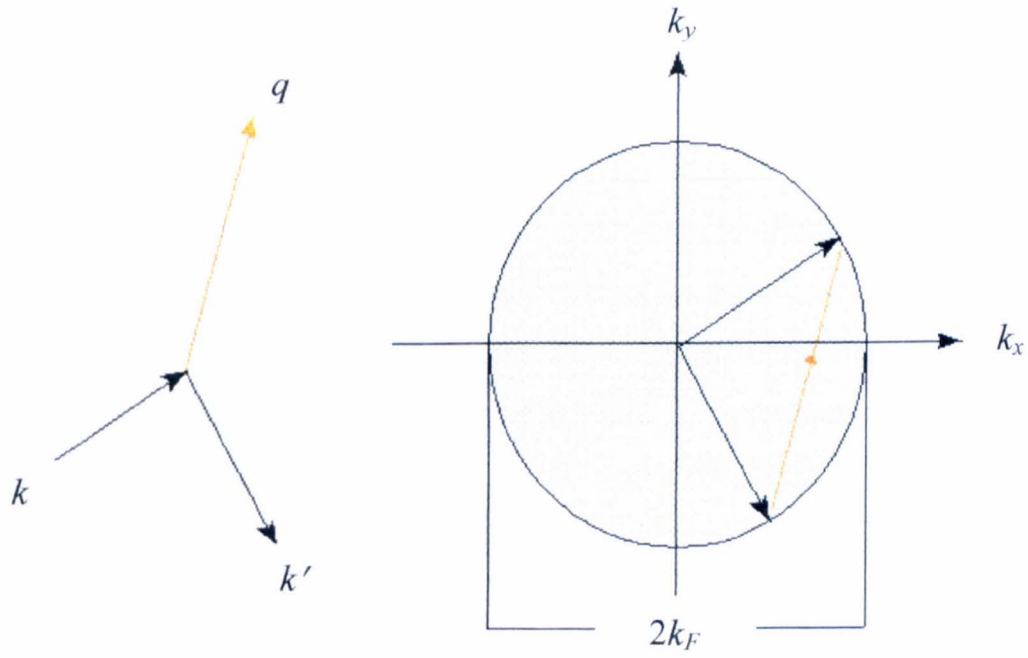

Figure 2.11: Electron-phonon interaction represented as transitions on the Fermi circle

where k and k' represent the initial and final electron states and a phonon of wavevector q, with energy $\hbar\omega_q$ is emitted in the process. The corresponding expression for the absorption of a phonon is similarly written:

$$\boldsymbol{k} = \boldsymbol{k}' - \boldsymbol{q} \tag{2.51b}$$

Energy is also conserved in the interaction, i.e. :

$$E_k = E_{k'} \pm \hbar\omega_q \tag{2.52}$$

where + indicates emission, and – represents absorption.

These transitions are represented diagramatically on the Fermi circle, shown in *Figure 2.11*. Due to the sharp boundary between filled and empty k-states at low temperatures, all electrons undergoing a transition have energies comparable to the Fermi energy, i.e. $|\boldsymbol{k}| \approx |\boldsymbol{k}'| \approx |\boldsymbol{k}_F|$.

The net energy transferred between electron and phonon, $\hbar\omega = \hbar^2 \Delta k^2 / 2m^*$ is therefore small with respect to the Fermi energy E_F. The maximum allowed transfer of momentum is limited by the case of an electron scattering from one point on the Fermi circle to the point diametrically opposite, a distance of $2k_F$ in wavevector-space. This imposes a limiting value for the phonon wavevector component in the 2D plane, known as the $2k_F$ cutoff :

$$q_{//} \leq 2k_F \tag{2.53}$$

Momentum conservation perpendicular to the plane is accounted for in the transition matrix element, formed by the overlap integral of the initial and final electron states:

$$M_k^{k',(q,\lambda)} = \langle k'|V_{e-p}|k\rangle = \int \Psi_{k'}^* V_{e-p} \Psi_k \, dr \qquad (2.54)$$

where $V_{e\text{-}p}$ represents the deformation or piezoelectric coupled interaction potential, k and k' are the initial and final electron states, and (q,λ) represents the wavevector and mode of the emitted phonon.

Applying *Equation 2.54* to the interaction potentials in turn, the electron-phonon coupling matrix element in each case is obtained.

The matrix element integral can be split into separate integrals for the directions parallel and perpendicular to the 2D electron gas respectively. From the parallel integral, a conservation of momentum expression is obtained, yielding the $2k_F$ momentum cutoff. The integral over z gives rise to a bound-state form factor $|F(q_z)|^2$ (Stern and Howard, 1967), where:

$$F(q_z) = \int \Psi_0^*(z) \exp(iq_z z) \Psi_0(z) dz \qquad (2.55)$$

where Ψ_0 is the ground-state wavefunction for the 2D layer.

For a heterojunction, assuming a triangular confinement potential described by the Stern-Howard variational wavefunction, a well-known result is obtained:

$$\left|F(q_z)^2\right| = \frac{1}{\left(1 + q_z^{\,2} a_o^{\,3}\right)^3} \qquad (2.56)$$

For an infinitely deep square quantum well, with ground-state wavefunction given by *Equation 2.9*, after a slightly lengthy integral (see Appendix A for derivation), the following form factor is obtained:

$$\left|F(q_z)^2\right| = K^2(\sin^2 q_z w + (1 - \cos q_z w)^2) \qquad (2.57)$$

where $K = \left(\frac{1}{q_z w}\right) - \left(\frac{1}{2(q_z w + 2\pi)}\right) - \left(\frac{1}{2(q_z w - 2\pi)}\right)$

For a quantum well with a finite potential step, the form-factor may be evaluated numerically, by re-expressing *Equation 2.57* in non-complex notation:

$$|F(q_z)|^2 = \left(\int |\Psi_0(z)|^2 \cos(q_z z) dz \right)^2 + \left(\int |\Psi_0(z)|^2 \sin(q_z z) dz \right)^2 \qquad (2.58)$$

In computing the finite potential well wavefunction $\Psi_0(z)$ (*Equations 2.10a,b*), the approximation $k \sim k_F$ is made, as described above.

The coupling matrix elements may be more conveniently expressed as the product of terms that are respectively independent, $\left|M_k^{'k',(q,\lambda)}\right|$, and dependent, $A_{q,\lambda}$, upon the directions of the phonon wavevector q and polarisation vector ε, i.e.

$$\left|M_k^{k',(q,\lambda)}\right|^2 = \left|M_k^{'k',(q,\lambda)}\right|^2 \times A_{q,\lambda} \times S_{q,\lambda} \times |F(q_z)|^2 \times \delta(k, k' + q_{//}) \qquad (2.59)$$

The term $S_{q,\lambda}$ represents the screening of the interaction potential as discussed above, and the final two terms account for the momentum conservation requirements respectively perpendicular to, and parallel with the 2DEG plane.

For the deformation potential and piezoelectric interactions in turn, the components of $\left|M_k^{'k',(q,\lambda)}\right|^2$ and $A_{q,\lambda}$ are given by:

$$\frac{2\pi}{\hbar}\left|M'_{DP}\right|^2 = \frac{\pi E_d{}^2 q}{L^3 \rho s_{LA}} \qquad A_{q,DP} = \frac{s_{LA}}{\upsilon_{q,\lambda}}\left(\hat{q}_x \varepsilon_x{}^{\lambda} + \hat{q}_y \varepsilon_y{}^{\lambda} + \hat{q}_z \varepsilon_z{}^{\lambda}\right)^2$$

(2.60a) (2.60b)

$$\frac{2\pi}{\hbar}\left|M'_{PZ}\right|^2 = \frac{\pi (e h_{14})^2}{L^3 \rho s_{TA} q} \qquad A_{q,PZ} = \frac{s_{TA}}{\upsilon_{q,\lambda}}\left(\hat{q}_x \hat{q}_y \varepsilon_z{}^{\lambda} + \hat{q}_z \hat{q}_x \varepsilon_y{}^{\lambda} + \hat{q}_y \hat{q}_z \varepsilon_x{}^{\lambda}\right)^2$$

(2.61a) (2.61b)

2.4.3 Acoustic Phonon Emission

The relaxation of an excited electron through the emission of an acoustic phonon is characterised by the crystal momentum conservation equation $\boldsymbol{k} = \boldsymbol{k'} + \boldsymbol{q}$, where $\boldsymbol{k}$ is the initial electronic state, $\boldsymbol{k'}$ is the state into which the electron is scattered, and $\boldsymbol{q}$ is the wavevector of the phonon emitted in the process.

In the treatment given here, the emission of acoustic phonons by a hot gas of free two-dimensional electrons is considered, with the following assumptions:

- The carriers are in thermal equilibrium and any drift velocity effects can be ignored; i.e. a Fermi carrier distribution.
- The electron temperature T_e is in the regime $k_B T_l < k_B T_e < \hbar\omega_{LO}$, where $\hbar\omega_{LO}$ is the energy at which optic phonon emission becomes significant.
- The screening of the interaction potentials and anisotropy of the electron-phonon interaction are incorporated using the form of the coupling matrix elements given above in 2.4.2.

The probability of a transition between two discrete electron states k and k' is given by the Fermi Golden Rule:

$$W_k^{k',q} = \frac{2\pi}{\hbar}\left|M_k^{k',(q,\lambda)}\right|^2 \delta\left(E_k - E_{k'} - \hbar\omega_q\right) \tag{2.62}$$

where $\left|M_k^{k',(q,\lambda)}\right|^2$ is the squared electron-phonon coupling matrix element.

The energy relaxation rate into a phonon mode of wavevector q, and polarisation λ is given by the product of the phonon energy and emission rate:

$$P_{q,\lambda} = \hbar\omega_{q,\lambda}\frac{dn_q}{dt} \tag{2.63}$$

where n_q is the Bose-Einstein occupation number of the phonon mode q.

The total emission rate into the phonon mode q,λ, summed over all possible electron states, for a given temperature, is given by:

$$\Lambda_k^{k',q,\lambda} = \frac{dn_q}{dt} = g_s g_v \sum_{k,k'}\left(f_k\left(1-f_{k'}\right)\left(n_{q,\lambda}+1\right)W_k^{k',q,\lambda}\right) \tag{2.64}$$

where g_s, g_v are the spin and valley degeneracies of the electronic k-states, $f_k, f_{k'}$ are the Fermi-Dirac electron distribution functions of the initial and final states, and $n_{q,\lambda}$ is the Bose-Einstein phonon occupation number of the mode q,λ.

In considering the net emission at a carrier temperature T_e in a semiconductor having a bulk, or lattice temperature T_l, where $T_e >> T_l$, the overall power emitted into the phonon mode q,λ is given by:

$$P_{q,\lambda} = \hbar\omega_{q,\lambda}\left(\Lambda(T_e) - \Delta(T_l)\right) \tag{2.65}$$

The approximation is made that $T_e >> T_l$ and so the energy flowing from phonons to electrons in absorption processes is negligible compared to the energy transferred to emitted phonons.

Expanding the previous equation:

$$P_{q,\lambda} = \hbar\omega_{q,\lambda} g_s g_v \frac{2\pi}{\hbar} \left| M_k^{k',(q,\lambda)} \right|^2 \left[n_{q,\lambda}(T_e) - n_{q,\lambda}(T_l) \right] \sum_{k,k'} (f_k^{T_e} - f_{k'}^{T_e}) \delta(E_k - E_{k'} - \hbar\omega_{q,\lambda}) \tag{2.66}$$

Replacing the matrix element term by the consituent parts in Eq. 2.60 :

$$P_{q,\lambda} = \hbar\omega_{q,\lambda} g_s g_v \frac{2\pi}{\hbar} \left| M_k^{k',(q,\lambda)} \right|^2 A_{q,\lambda} S_{q,\lambda} |F(q_z)|^2 \left[n_{q,\lambda}(T_e) - n_{q,\lambda}(T_l) \right] \sum_{k,k'} (f_k^{T_e} - f_{k'}^{T_e}) \delta(E_k - E_{k'} - \hbar\omega_{q,\lambda}) \delta(k, k' + q_{//}) \tag{2.67}$$

Following the technique of Toombs *et al.* (1987) and Hawker (1990), the summation over *k*-states is transformed to an integral that may be expressed in energy terms:

$$P_{q,\lambda} = \hbar\omega_{q,\lambda} g_s g_v \frac{2\pi}{\hbar} \left| M'^{k',q,\lambda}_{k} \right|^2 A_{q,\lambda} S_{q,\lambda} |F(q_z)|^2 \left[n_{q,\lambda}(T_e) - n_{q,\lambda}(T_l) \right] \sum_{k,k'} (f_k^{T_e} - f_{k'}^{T_e}) \delta(E_k - E_{k'} - \hbar\omega_{q,\lambda}) \delta(k, k' + q_{//}) \tag{2.68}$$

To obtain the total energy loss rate of the two dimensional electron gas, the above expression must be summed over all permitted phonon wavevectors and polarisations:

$$P_{total} = \sum_{\lambda} \int d\Omega \int dq P_{q,\lambda} \frac{q^2 V}{(2\pi)^3} \tag{2.69}$$

where $Vq^2 d\Omega dq/(2\pi)^3$ is the number of normal modes in a volume of phase space $q^2 d\Omega dq$, and $d\Omega = \sin\theta d\theta d\varphi$ is the element of solid angle into which the phonons are emitted.

Chapter 3

Theory Results

3 Theory Results and Discussion

3.1 Introduction

This chapter presents a complete model for the emission and propagation of acoustic phonons from a hot two-dimensional electron (or hole) gas in a cubic semiconductor crystal, in the form of a computer simulation devised and written by the author.

A brief description of the concepts and approach used in the development of the program software is given, followed by a detailed treatment of the 2D phonon system being experimentally investigated in later chapters of this work.

Finally, the importance of such aspects as interaction screening and matrix element anisotropy in the representation of the electron-phonon system is discussed with reference to numerical calculations performed using the model.

3.2 Computer Simulation of 2D Phonon System

The computer program "2D Phonon Theory Simulator" was written by the author in order to graphically illustrate the equations presented in Chapter 2.

The principal objective of the program is to facilitate the calculation of the acoustic phonon emission rate with respect to a number of variable parameters of the 2D system, e.g. electron temperature, sheet density, quantum well width, emission angle, phonon frequency, mode(s) and coupling process(es). Furthermore, by making it possible to selectively include or exclude such factors as interaction screening and matrix element anisotropy, and comparing the program output to experimentally obtained results,

conclusions may be drawn regarding the importance of the inclusion of these factors in the model.

To fulfil these requirements, a user interface for the program was developed using the Microsoft Visual Basic 4.0 environment (*Figure 3.1*), to facilitate the setting of these parameters, which are automatically saved and restored between sessions.

The user interface also includes custom-written routines to handle the display of graphs and images (*Figure 3.2*), incorporating such functionality as zooming, rescaling and linescans through images. The interface is supplemented by a library of routines to handle the numerical calculations, written in C using Microsoft's Developer Studio 4.0 in order to optimise the speed of program execution. This library is compiled into a 32-bit Windows DLL (dynamic link library) that is distributed with the main interface program.

In order to accurately "map" the theoretical distribution of emitted phonon energy emerging from a source positioned at one surface of a cubic crystal, and arriving at a detector on the opposite face, it is necessary to consider two dominant factors in determining the distribution of wavevectors and modes in the detected phonon flux: the electron-phonon interaction and the phonon propagation through the crystal.

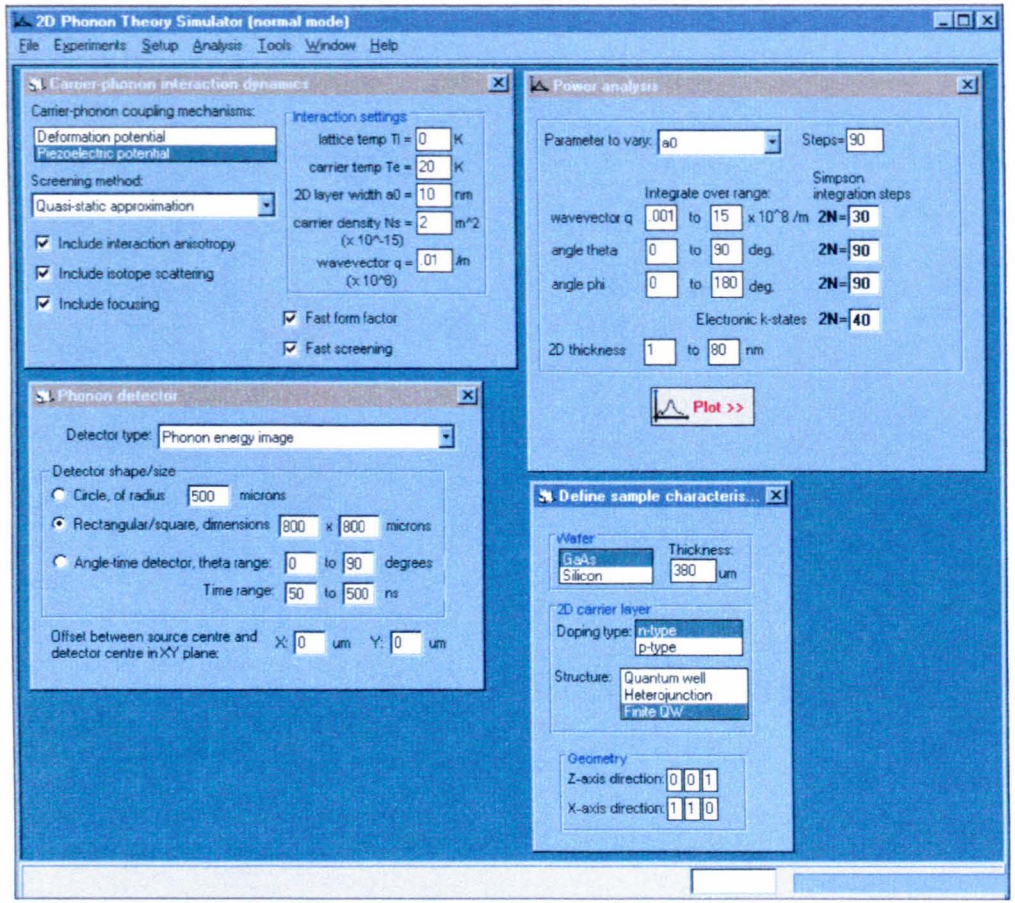

Figure 3.1: Properties of the electron-phonon interaction and experimental arrangement can be configured before starting a virtual phonon experiment.

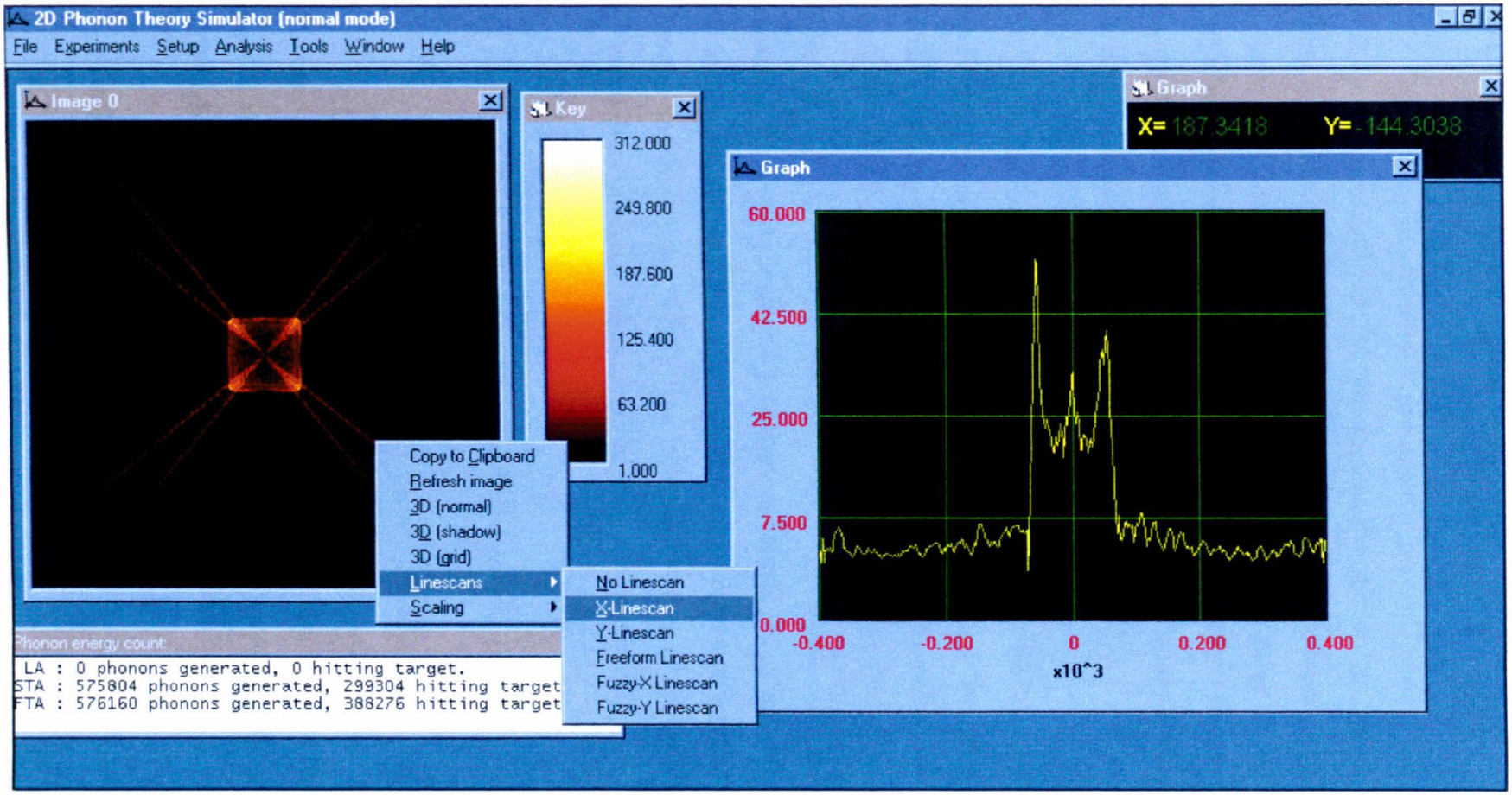

Figure 3.2: Image and line-graph functionality of the Theory simulation

3.3 Computer Simulation of Phonon Focusing

Considering first the phonon propagation: phonon focusing, as discussed in 2.3.3.2, significantly affects the angular distribution of phonon energy, owing to the non-colinearity of wavevector and energy transport in anisotropic cubic media. Northrop (1982) developed a FORTRAN program to obtain an analytic expression for the phonon flux enhancement factor A for an arbitrarily chosen phonon wavevector direction in k-space, based on the solution of the Christoffel elastic matrix as given in Every (1980).

With the improvement in computing power since this first program, it has become possible to apply Monte-Carlo techniques to the generation of phonon focusing patterns. With such a method, a large number of "virtual" phonons (hereafter referred to simply as "phonons"), having wavevector directions θ_q, φ_q chosen randomly from an isotropic distribution, are generated. Their associated group velocity directions θ_v, φ_v are calculated in the framework of elastic waves, and the result is mapped onto a detector plane. (Gancza and Paskiewicz, 1995) The isotropic LA and TA phonon focusing patterns shown in *Figure 2.9* are obtained using such a method.

3.3.1 Computer Simulation of Electron-Phonon Interaction

To complete the task of modelling of emitted phonon energy flux reaching a detector region positioned on one face of an anisotropic crystal, it is also necessary to compute the angular distribution of such wavevectors at the point of emission from the source that arises from the energy and momentum conservation requirements of the electron-phonon interaction.

Considering first the focusing: in 3.2.1 above, a "Monte-Carlo" technique for mapping out the focusing pattern is described, based on explicit calculation of the group velocities associated with randomly chosen wavevector directions from an isotropic angular distribution.

In order to account for the non-uniformity of the anisotropic distribution of wavevectors obtained from the electron-phonon interaction, two main approaches may be taken.

In the first approach, phonon wavevectors are chosen randomly over the full range of angular directions as before. The energy relaxation rate into a unit solid angle $d\Omega$ is calculated for the chosen direction, integrating over all possible wavevector magnitudes q. The resulting energy loss rate is used to scale the mapped result onto the detector plane. This is in contast to the isotropic Monte-Carlo approach, in which each created phonon contributes an equal weight to the phonon image.

An alternative, novel approach has been developed by the author, in which the energy weighting of each phonon is equal, as in the simple isotropic Monte-Carlo model. This is achieved through the use of a "selective wavevector" Monte-Carlo technique. In this method, the electron-energy relaxation rate calculation is performed first, for all phonon modes and wavevectors. The results of this calculation are stored in a large data array of N points, as a function of θ, φ and the phonon mode.

This array is then transformed into a new array, P_{int}, storing "integrated power", where:

$$P_{int}(n) = \sum_{m=1}^{n} P_{non-int}(m) \qquad (3.1)$$

i.e. the nth element of the modified array contains the summed total of the 1st, 2nd, 3rd... (n-1)th and nth elements of the original array, so that the final element, $P_{total} = P_{int}(N)$ of the transformed array contains the total emitted power into all phonon wavevectors and modes by the 2DEG.

A random power between 0 and P_{total} is then generated, and by "indexing" into the integrated power array using a binary search technique, the wavevector directions θ, φ are found.

By interpolation of the random power, P_{ran}, falling between the powers corresponding to two successive integrated power array elements $P_{int}(\vartheta_n, \varphi)$, $P_{int}(\vartheta_{n+1}, \varphi)$, the θ-angle is obtained. The range of possible θ-angles is continuous, as in the isotropic Monte-Carlo technique. The φ-angles, however, are discrete, stepped at intervals determined by the array size N (which in turn is determined by the time allowed by the user for calculation of the electron-phonon coupling). Therefore, to transform φ into a continuous function, a re-randomisation algorithm is applied, represented in pseudo-code as:

$$\varphi_{randomised} = \varphi_m + \Delta\varphi\left(RAND(1) - \frac{1}{2}\right) \tag{3.2}$$

where the function RAND(1) returns a pseudo-random floating-point number between 0 and 1, and $\Delta\varphi$ is the interval between the two elements in the data array.

The principal advantage of this "selective wavevector" procedure is that the efficiency with which the final image is defined is increased, as the contribution to the image that will be made up by each generated Monte-Carlo phonon is already known. By contrast, there may be several orders of magnitude of difference between the minimum and maximum emission power contribution of randomly chosen wavevector directions in the first model described above. The integrated power array may also be saved to disk, allowing it to be reloaded into memory to generate further focusing patterns based on the same electron-phonon system, without the requirement to recalculate the effects of the interaction.

Consequently, after the initial computing cost of calculating the electron energy relaxation rate has been paid, anisotropic phonon focusing patterns may be generated almost as quickly as for isotropic patterns (approximately 30,000 phonons/second on an 375MHz AMD K6-2 processor), enabling high-resolution images to be generated very quickly (less than one minute is usual) on a modern PC computer.

Comparison of the images obtained with this technique show good qualitative agreement in the focusing structures observed by Jasiukiewicz *et al.* (1999), using long acquisition times on UNIX mainframe computers.

3.4 Calculations of Electron Energy Relaxation from a Heated 2DEG Quantum Well

The discussion that follows describes the emission of acoustic phonons by hot electrons confined in a 2DEG quantum well, in terms of the results of calculations performed using the computer program described above. In all cases, unless otherwise stated, the full model of the electron-phonon interaction is used, including dynamic Lindhard screening and electron-phonon coupling matrix element anisotropy.

Table 3.1 shows the numerical values used for parameters found in the equations of Chapter 2.

Parameter		**Value**
DP coupling constant E_d		12.0 eV
PZ coupling constant h_{14}		1.45×10^{9} eV m^{-1}
Density ρ		5316 kg m^{-3}
Elastic constants	C_{11}	121.1×10^{10} dyn cm^{-2}
	C_{12}	54.8×10^{10} dyn cm^{-2}
	C_{44}	60.4×10^{10} dyn cm^{-2}
Al concentration x in $(Al_xGa_{1-x})As$		0.33

Electron effective mass in well m^*	$0.0667m_0$
Electron effective mass in barrier m_B^*	$0.0940m_0$
Height of QW potential barrier V_0	332mV
Spin degeneracy g_s	2
Valley degeneracy g_v	1
Dielectric constant ε_r	13.2
Isotope scattering constant A	7.38×10^{-42} s^3

Table 3.1: Numerical parameters used in theoretical model.

An important consideration in studying the phonon emission from a 2DEG is the relative strengths of the DP and PZ interaction potentials. *Figure 3.3* shows the angle-averaged matrix elements $|M_{e-p}|^2$ for the deformation potential and piezoelectric interaction, from *Equations 2.55* and *2.56*.

The deformation potential varies linearly with the magnitude of the phonon wavevector q, whereas the piezoelectric interaction varies as q^{-1}. Deformation potential coupling favours higher wavevectors, therefore it is the dominant process by which the electron-phonon interaction occurs at high temperatures and for high-energy transitions. PZ coupling is the preferred mechanism for small wavevector transitions, and dominates only for very low temperatures. ($T_e < 1$K in narrow quantum wells, $T_e < 3$K in heterojunctions)

Using the values for the DP and PZ coupling constants given above, the crossover between the piezoelectric interaction and deformation potential occurs at $q_z = 1.83x10^8 m^{-1}$, above which the deformation potential is dominant. The extent to which the dominance occurs, however, is dependent upon the $2k_F$ and $1/a_0$ interaction cutoffs. The bound-state form factors $|F(q_z)|^2$ are shown in *Figure 3.4*. Assigning a cutoff wavevector q_c, defined as the value at which the form factor falls to $1/e$, *Table 3.2* shows how the interaction cutoff varies depending on the thickness of the 2D sheet (in all cases, the sheet density, N_s, has been taken to be $2 \times 10^{15} m^{-1}$)

2DEG parameters	Cutoff wavevector q_c
Heterojunction / a_0 = 3nm	2.1 x 10^8 m^{-1}
Infinite-height QW / a_0 = 6.8nm	7.9 x 10^8 m^{-1}
Finite-height QW / a_0 = 3.6nm	7.3 x 10^8 m^{-1}
Finite-height QW / a_0 = 6.8nm	5.3 x 10^8 m^{-1}
Finite-height QW / a_0 = 10.0nm	4.1 x 10^8 m^{-1}

Table 3.2: Variation of $1/a_0$ cutoff with 2D sheet thickness

For a typical heterojunction, the $1/a_0$ cutoff is expected to suppress the emission of all phonon wavevectors of magnitude $q > 2.1 \times 10^8$ m^{-1}, a wavevector closely comparable to the DP-PZ matrix element crossover. In this case, therefore, DP coupling will never clearly dominate over the PZ coupling. This suppression of DP-coupled modes has been presented at the primary reason for the absence of the "classically-predicted" dominant LA mode in heterojunctions (see e.g. Strickland, 1996).

Conversely, in narrower QWs, the $1/a_0$ cutoff is much weaker, with supression of phonon emission being pushed to a much larger wavevector, so that the dominant DP coupled modes predicted by the matrix elements are expected to be observed. It is also of note that the finite height quantum well approximation makes a significant difference to the form factor: using the infinite-height quantum well approximation results in a considerable weakening of influence of the $1/a_0$ cutoff, and consequently the DP coupling strength is overestimated.

Figure 3.5 shows the numerically calculated overall electron energy relaxation rate due to deformation potential coupled acoustic phonon emission in a 6.8nm GaAs/(AlGa)As quantum well, as a function of the electron temperature T_e. The carrier density N_s has been taken to be 2.0 x 10^{15} m^{-2}, and

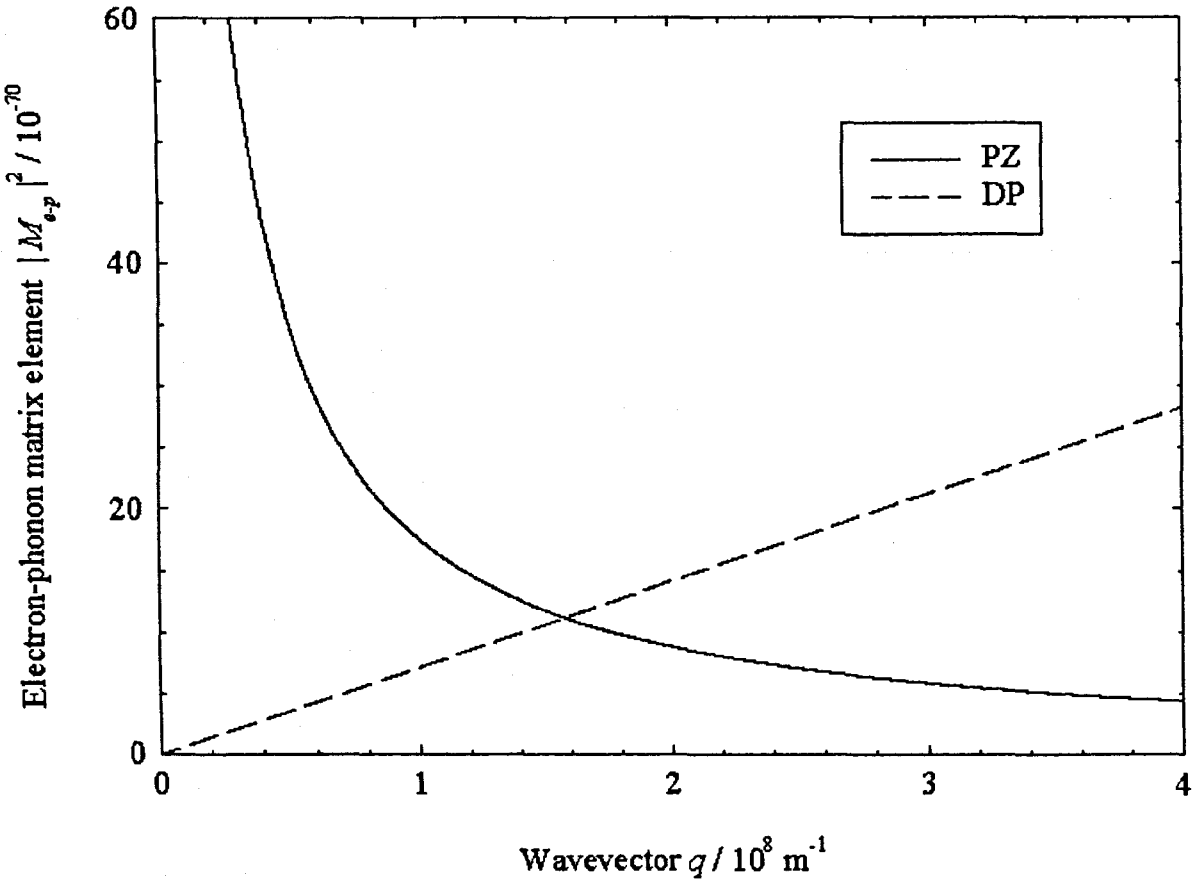

Figure 3.3: Angle-averaged electron-phonon matrix elements for DP and PZ coupling

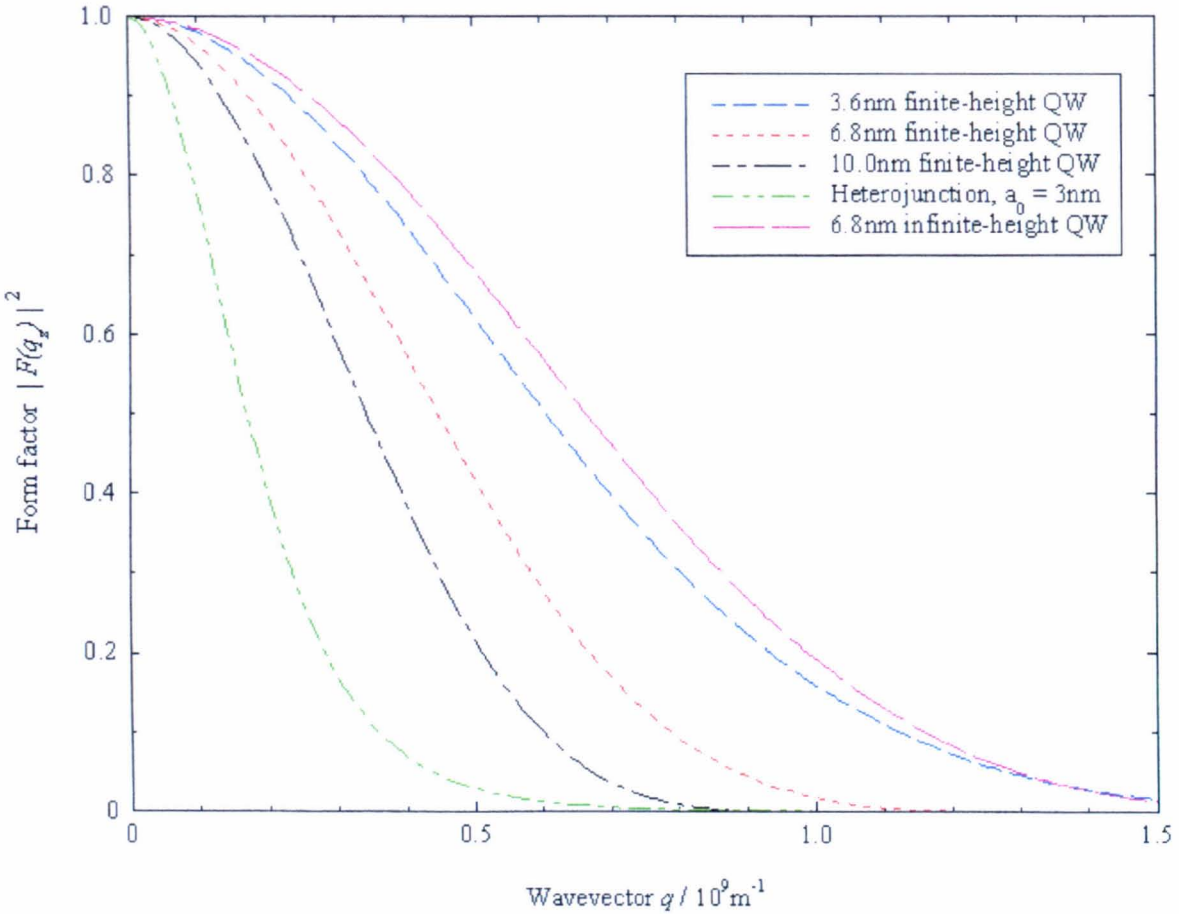

Figure 3.4: Bound-state form factors of 2DEGs of varying widths

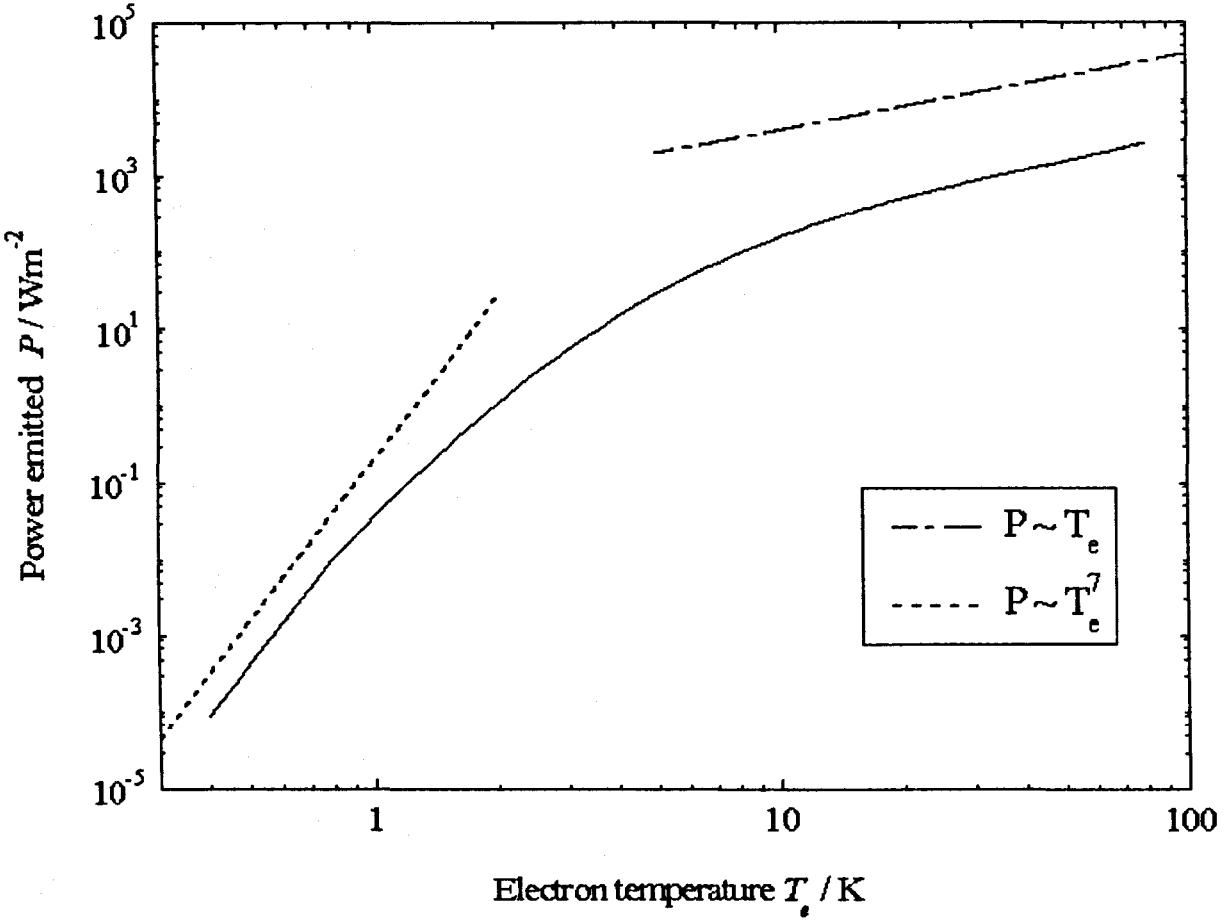

Figure 3.5: Temperature dependence of deformation potential coupled phonon emission from 6.8nm QW

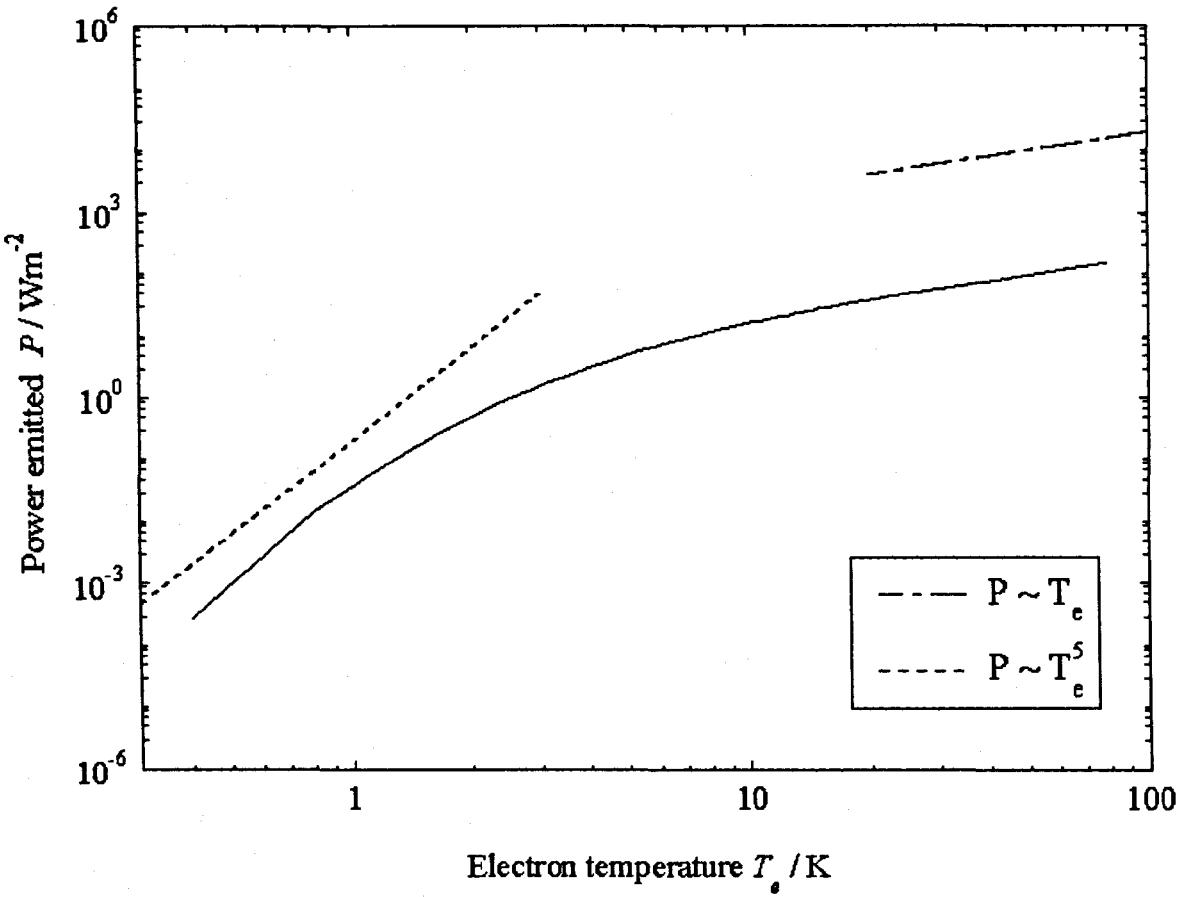

Figure 3.6: Temperature dependence of piezoelectric coupled phonon emission from 6.8nm QW

the assumption is made that the lattice temperature $T_l \sim 0K$. Two distinct regions are seen in the results: at very low temperatures, $T_e \leq 1.5K$, the relaxation rate varies as $P \sim T_e^7$, characteristic of screened DP coupling in the absence of the momentum cutoffs. At higher temperatures, the $2k_F$ and $1/a_0$ cutoffs strongly influence the spectrum of emitted phonons, weakening the dependence on T_e, which tends towards $P \sim T_e$ at high temperatures.

For piezoelectric coupling (*Figure 3.6*), the power varies as $P \sim T^5$ at very low temperatures, again weakening towards a linear dependence as the temperature is increased. The crossover between DP and PZ coupling occurs at $T_e = 1.1K$, in notable contrast to calculations for heterojunctions (e.g. Kent, 1998), where PZ-coupled TA modes are predicted to account for one third of the energy relaxation rate at 50K. This discrepancy can be attributed to the much weaker $1/a_0$ cutoff in a 6.8nm quantum well and to differences between the screening methods applied in each case.

Figure 3.7 shows the dependence of the total emission power from a hot 2DEG QW on the 2D carrier density as a function of (a) emission angle, (b) temperature, and (c) well width. The carrier density N_s determines the Fermi energy of the 2D electron system and, therefore, the energy at which phonon emission is suppressed due to the $2k_F$ cutoff. The correlation of the carrier density to the $1/a_0$ cutoff is much weaker: from *Figure 3.7a* it is seen that at small angles, where $q_z \equiv q\cos\theta$ is at its greatest value, the variation of power with carrier density converges to a single curve. *Figure 3.8* shows the ratio of the total LA and TA phonon energies emitted as a function of the carrier density: this ratio varies by only ~ 10% over the range of N_s values of interest experimentally. These observations justify the use of quantum well samples with carrier densities in the range $N_s = 1.7 \times 10^{15} m^{-2}$ to $3.7 \times 10^{15} m^{-2}$ in the experimental studies presented in this work.

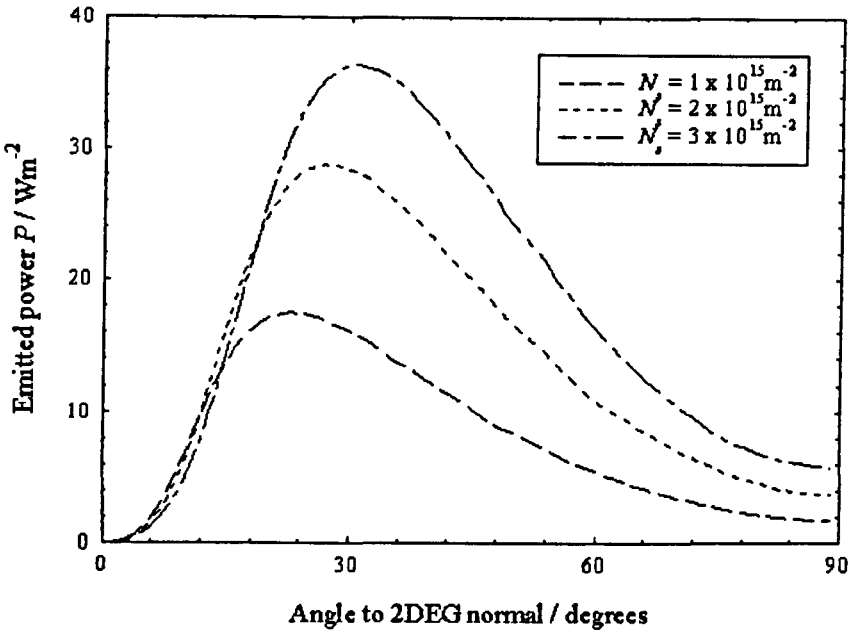

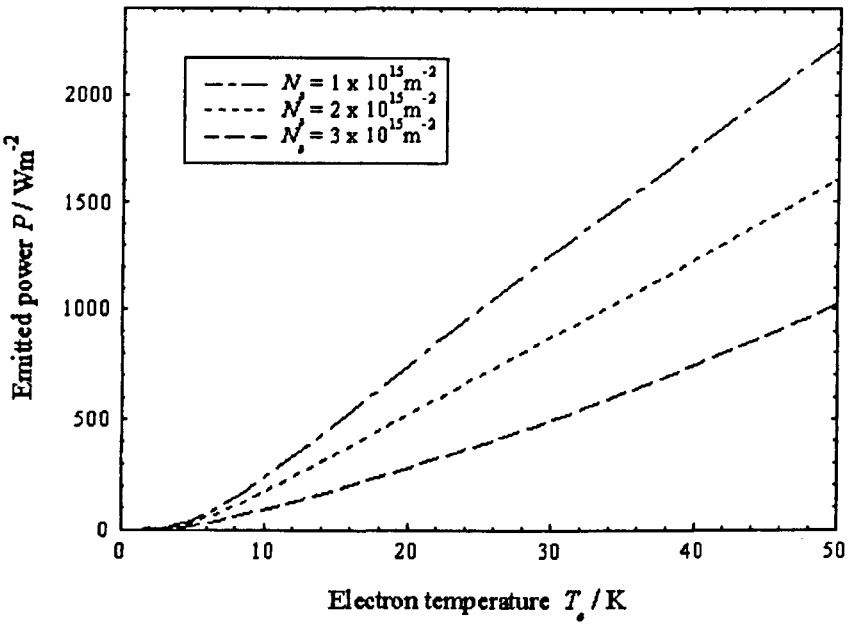

Figure 3.7: Variation of total emitted phonon power with 2D electron density N_s, as function of (a) emission angle θ to 2DEG normal, (b) electron temperature T_e.

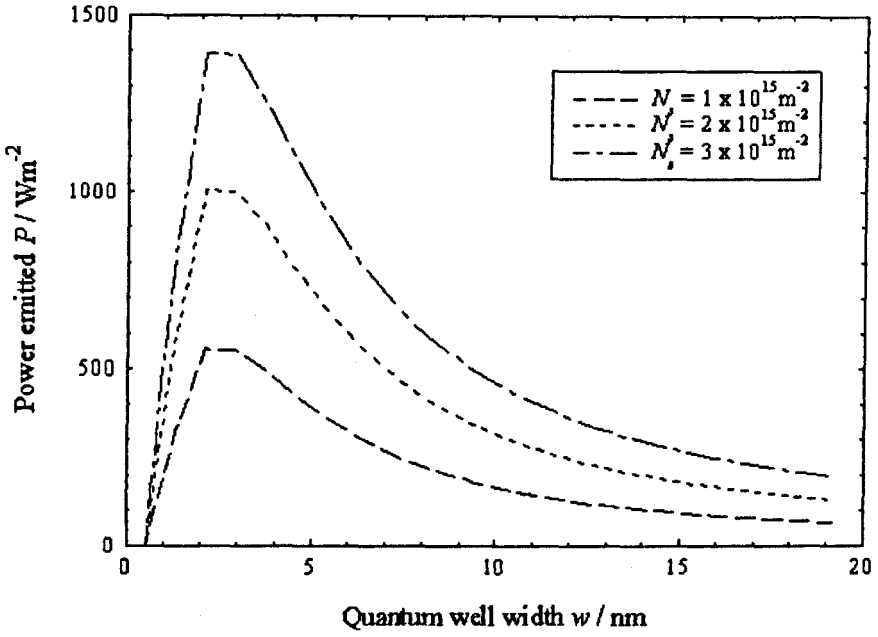

Figure 3.7(c) : Variation of total emitted phonon power with 2D electron density N_s, as function quantum well width w.

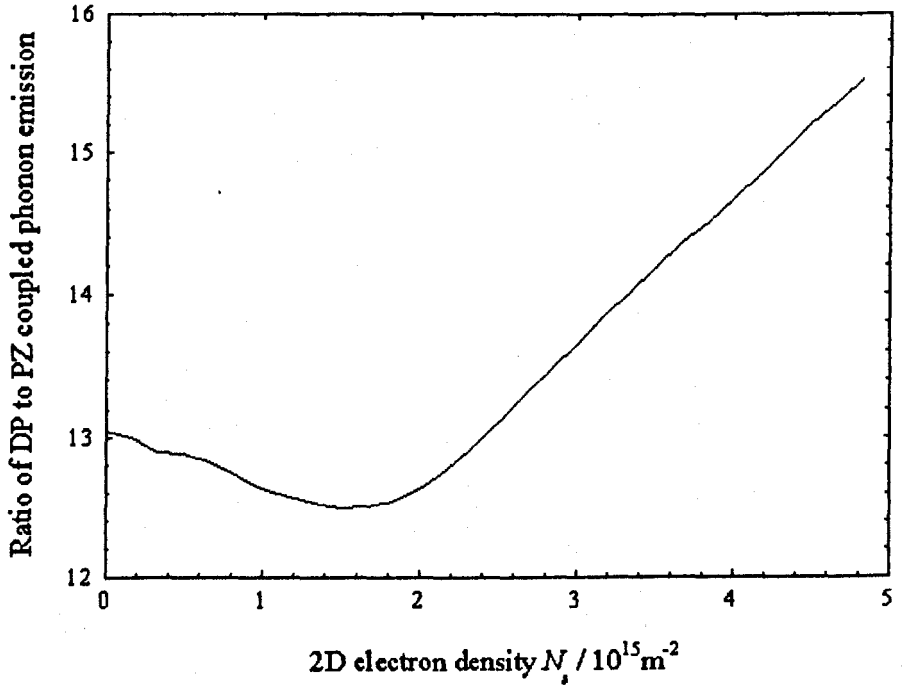

Figure 3.8: Ratio of DP to PZ-coupled emission power as function of 2D electron density N_s.

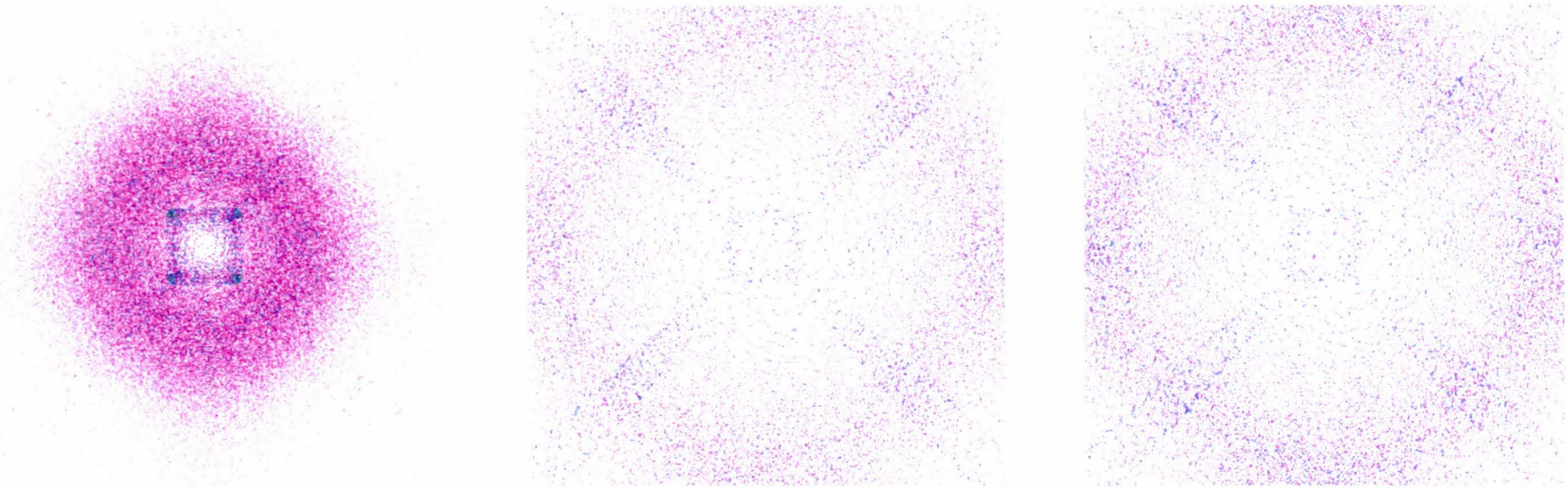

a) w = 3nm b) w = 6.8nm c) w = 15nm

Figure 3.9: Total phonon power from (a) w = 3nm (N_s=1.7 x $10^{15}m^{-2}$), (b) w = 6.8nm (N_s= 2.0 x $10^{15}m^{-2}$) and (c) w = 15nm (N_s=3.6 x $10^{15}m^{-2}$) 2DEG quantum wells at T_e = 50K. Emission is from a point source, propagated through a 380μm thickness of GaAs substrate and detected on an 800x800μm surface directly opposite the source.

3.4.1 Angular dependence of emitted power

The strong angular dependence of the emission is illustrated by *Figure 3.9*. These images show the calculated phonon energy flux arriving on the surface of the 380μm thick (100) wafer directly opposite the 2DEG for quantum wells of width w = 3nm, 6.8nm and 15nm respectively, ($N_s = 2\text{x}10^{15}\text{m}^{-1}$) at a temperature $T_e = 50K$. The images represents a surface area of 800x800μm, i.e. a total subtended angle of approximately 90° (+/- 45° around the 2DEG normal). The strong anisotropy of the emission and its dependence on the well width are clearly seen. This is due to the $1/a_0$ cutoff, limiting the allowed phonon wavevectors that may be emitted from the source, and focusing of the phonons along directions of crystallographic symmetry during their propagation to the detector.

Considering first the anisotropy arising from the $1/a_0$ cutoff, *Figures 3.10 to 3.13* show the angular distribution of the emitted phonon power from a point source, for each of the coupling-mode combinations DP-LA, DP-TA, PZ-LA and PZ-TA, as a function of a) electron temperature T_e and b) quantum well width w. The images depict the angular dependence in two dimensions, as mapped onto a surface of area 800x800μm, separated from the source by a orthogonal distance of 380μm. Each image is normalised to the peak power in its corresponding graph. Phonon focusing is not taken into account in these figures.

In general, it is seen that the peak angle in the emission spectrum shifts to narrower angles for higher temperatures and, more notably, for narrower well widths, demonstrating the effect of the $1/a_0$ cutoff:

$$q_z \equiv q\cos\theta \leq \frac{1}{a_0} \qquad (3.3)$$

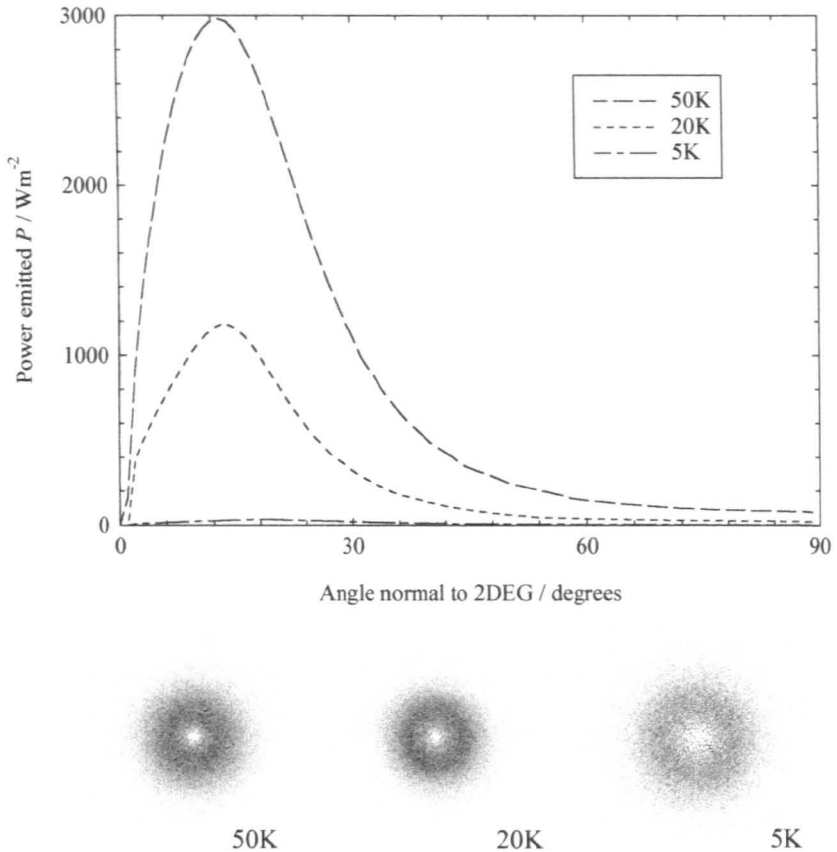

Figure 3.10 (a) : Angular distribution of emitted DP-coupled LA phonon emission as a function of T_e at 50K, 20K and 5K. (w = 6.8nm)

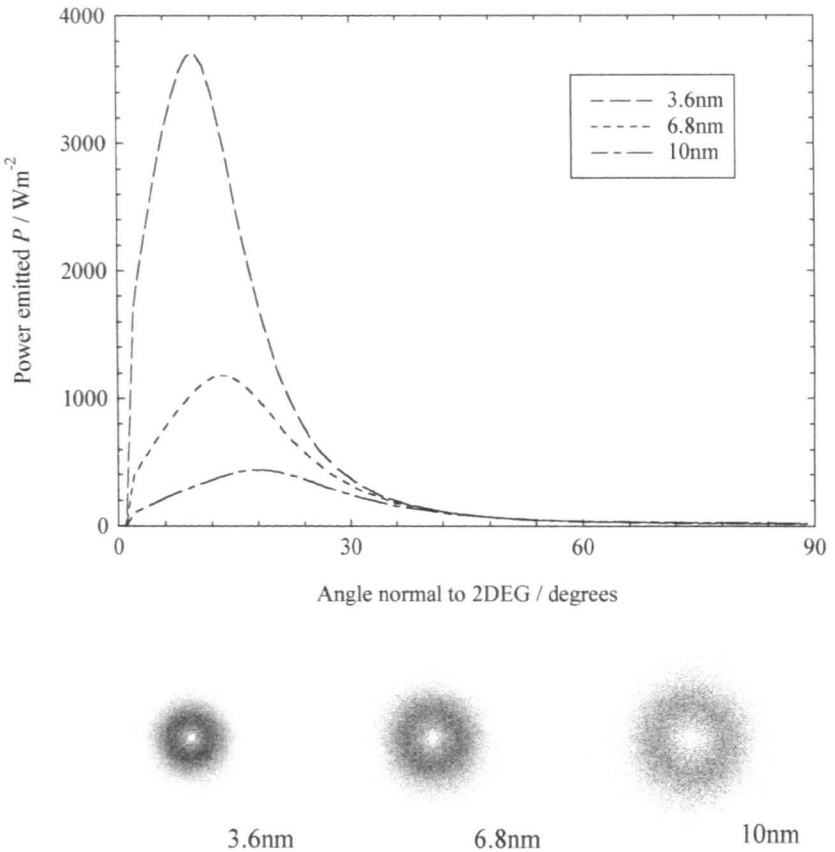

Figure 3.10 (b) : Angular distribution of emitted DP-coupled LA phonon emission as a function of w at 3.6nm, 6.8nm, 10nm (T_e = 20K)

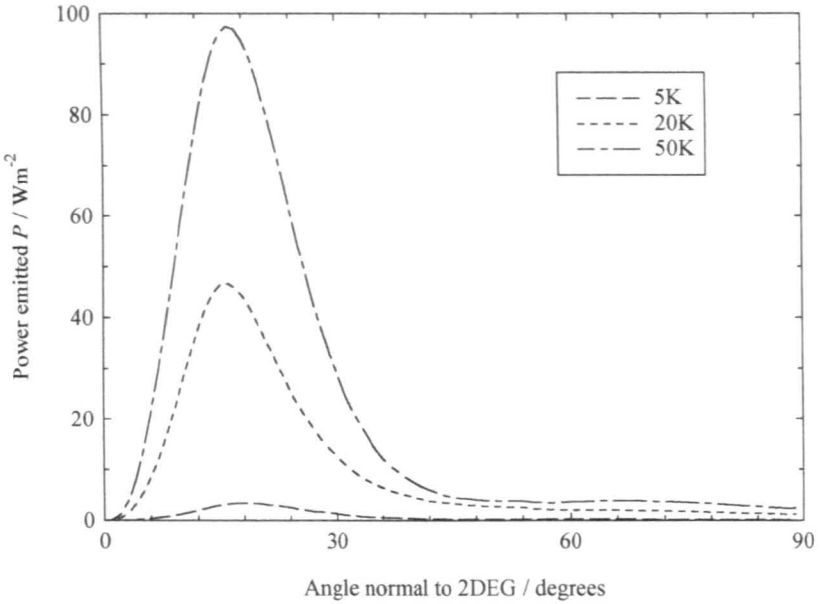

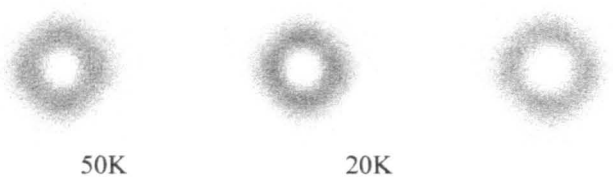

Figure 3.11 (a) : Angular distribution of emitted DP-coupled TA phonon emission as a function of T_e at 50K, 20K and 5K. (w = 6.8nm)

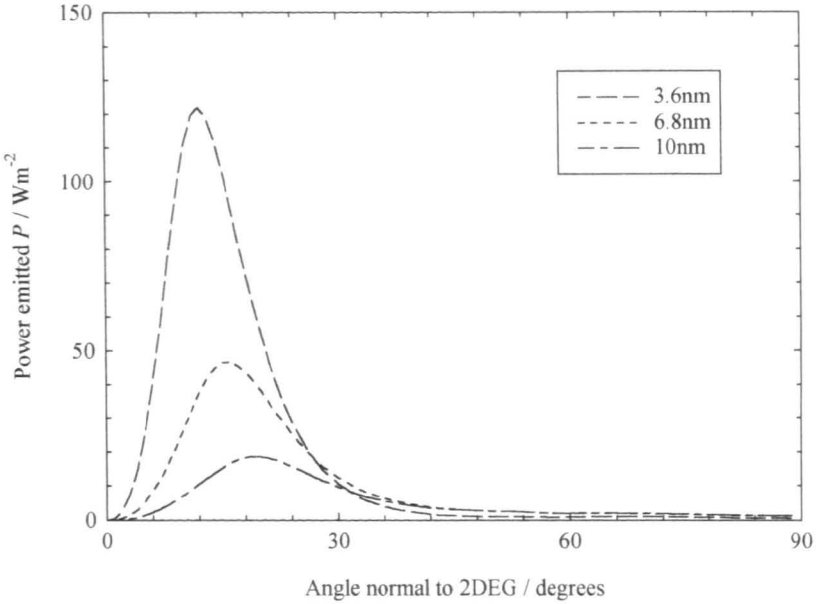

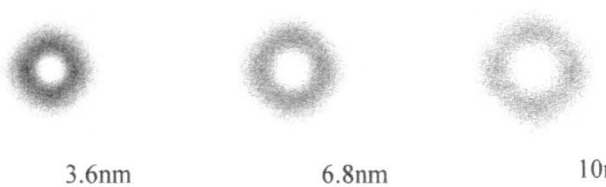

Figure 3.11 (b) : Angular distribution of emitted DP-coupled TA phonon emission as a function of w at 3.6nm, 6.8nm, 10nm (T_e = 20K)

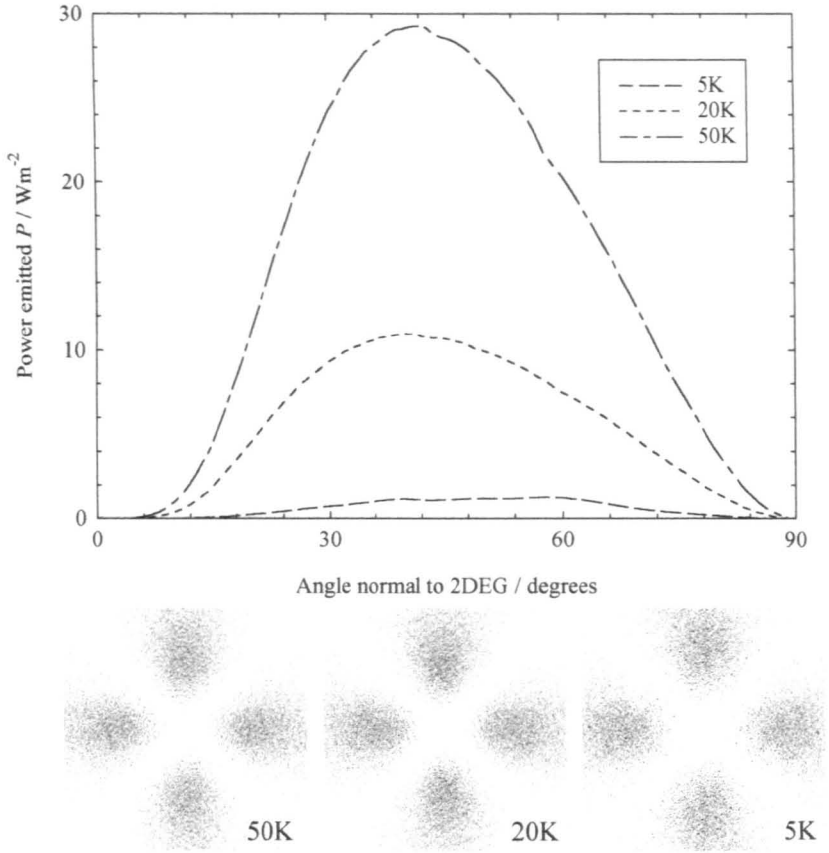

Figure 3.12 (a) : Angular distribution of emitted PZ-coupled LA phonon emission as a function of T_e at 50K, 20K and 5K. (w = 6.8nm)

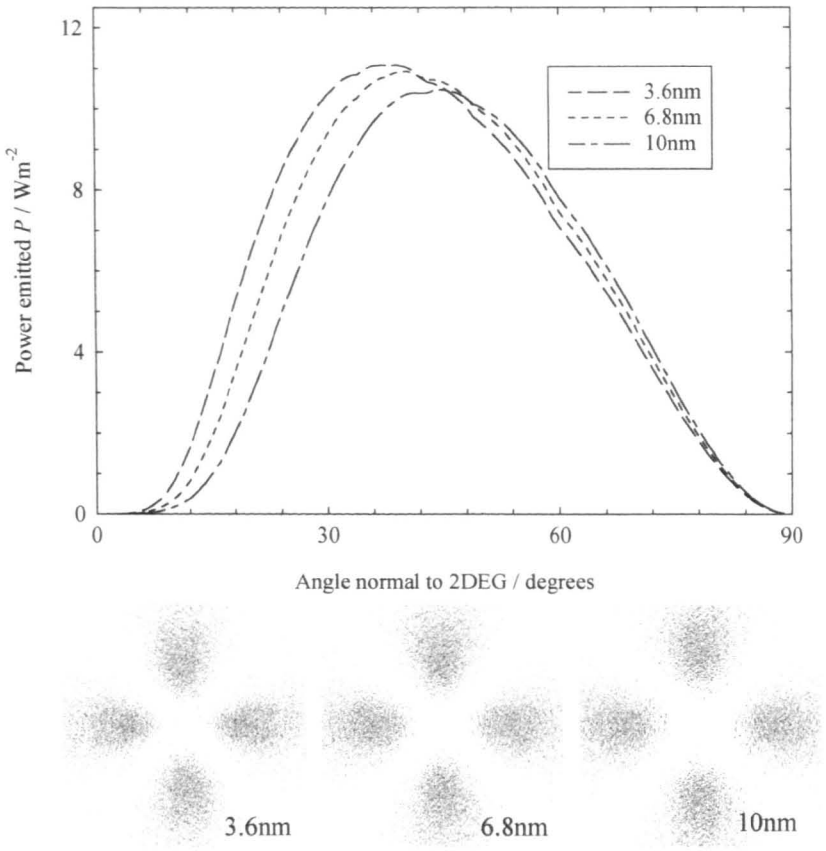

Figure 3.12 (b) : Angular distribution of emitted PZ-coupled LA phonon emission as a function of w at 3.6nm, 6.8nm, 10nm (T_e = 20K)

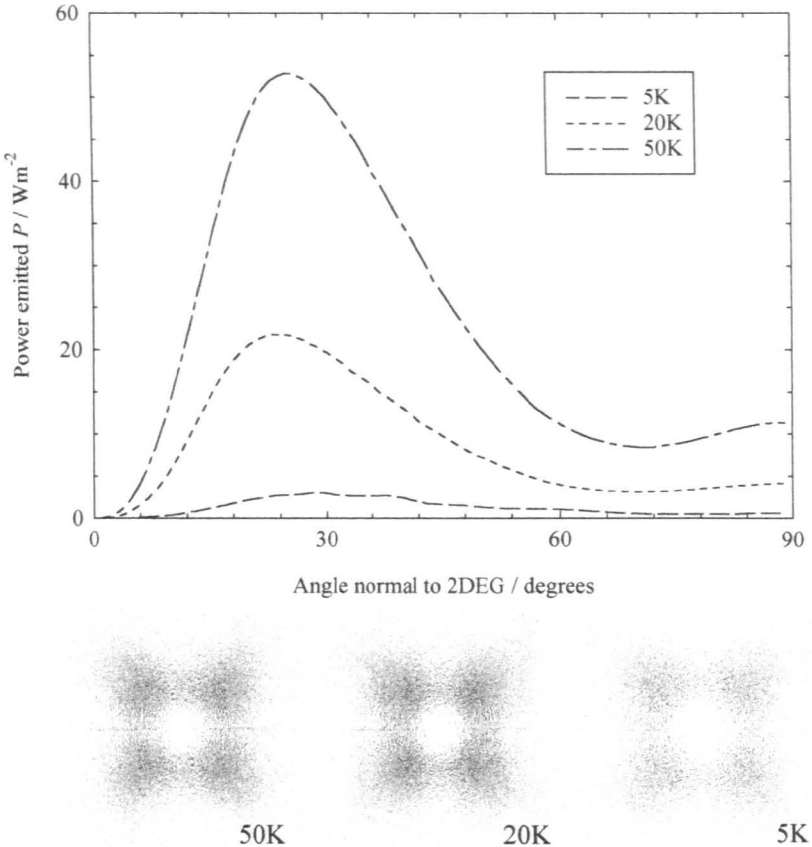

Figure 3.13 (a) : Angular distribution of emitted PZ-coupled TA phonon emission as a function of T_e at 50K, 20K and 5K. (w = 6.8nm)

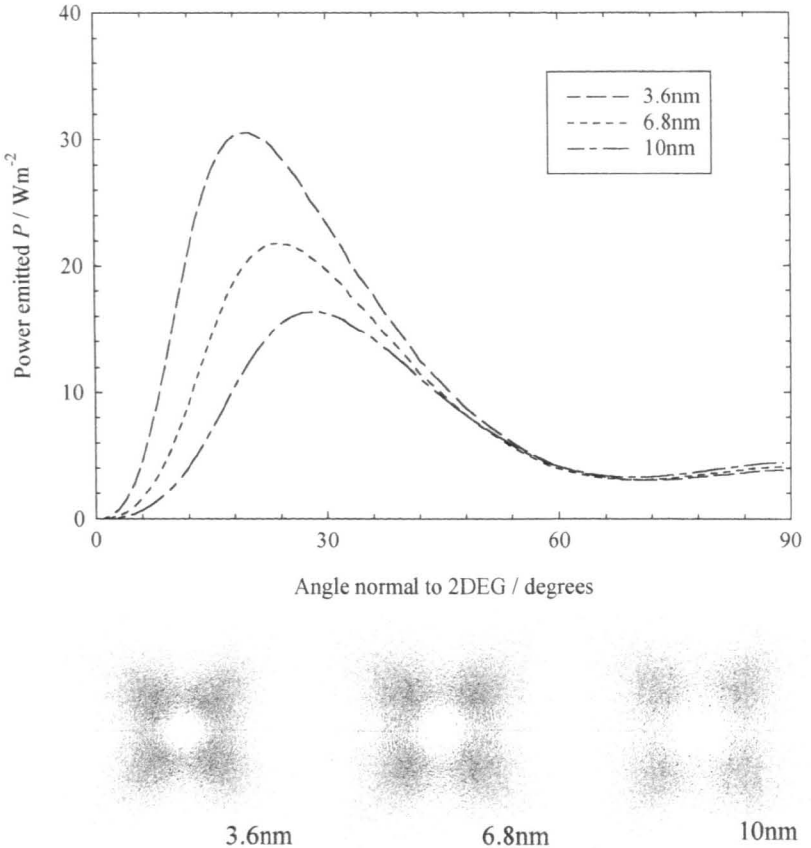

Figure 3.13 (b) : Angular distribution of emitted PZ-coupled TA phonon emission as a function of w at 3.6nm, 6.8nm, 10nm (T_e = 20K)

As the temperature T_e and characteristic phonon wavevector q are increased, so the average emission angle θ must decrease to satisfy the equation. Similarly, if the well width w (and hence a_0) is reduced, so the angle θ must become smaller to compensate.

The deformation potential modes show a large change in emission power between 5K and 20K, corresponding to the region on the power-temperature graph (*Figure 3.5*) in which the dependence has not yet become linear: in quantum well devices, the $1/a_0$ cutoff is sufficiently weak that the deformation potential continues to strengthen non-linearly until the temperature is very close to the acoustic-optic crossover ($T_e \approx 50K$). By contrast, the increase in the piezoelectric power shows only a thermal behaviour, increasing approximately linearly thoughout the 5K – 50K range.

As expected, the graphs show strongly dominant DP-coupled LA emission, peaking at $P \sim 3000 Wm^{-2}$ (1.5pW/electron) at 50K. These modes are emitted in a tight cone around the 2DEG normal, peaking at an angle of ~12°. A "hole" appears at the centre of the emission pattern, owing to the matrix element term, which couples together orthogonal states, disappearing at very small angles ($\theta < \frac{v_\lambda}{v_F}$).

The DP-coupled TA phonon response is of particular interest. Coupling of transverse phonons to the deformation potential is forbidden if the assumption of isotropic electron-phonon coupling matrix elements is taken. However, if the anisotropic matrix elements are used, the DP TA emission power is found to be somewhat stronger than the PZ TA power in the range of temperatures and well widths under consideration. Therefore, doubt must, be cast on the validity of earlier theoretical models that assumed that the electron-phonon system could be described using the assumption of emission exclusively into DP-coupled LA and PZ-coupled TA phonon modes.

As with the DP-coupled LA mode, the TA mode is emitted into a tight cone around the 2DEG normal, though the "hole" at small angles is observed to be somewhat larger, due to the lower relative velocity of the TA mode compared to the LA mode.

The PZ-coupled TA mode is emitted at a wider angle, due to the q^{-1} dependence of piezoelectric coupling, and lacks the toroidal shape of the DP emission spectra, owing to the anisotropic φ- dependence of the PZ matrix element (*Equation 2.56b*). The emission is seen to be strongest in the same directions that are associated with fast transverse mode focusing.

The PZ LA mode is the weakest of all, having a peak power some 100 times less than the DP LA mode. Once normalised for total power, the angular emission spectra is seen to have almost no dependence on either temperature or well width.

Considering now the total energy flux detected at a point on a surface opposite the 2DEG source, separated by some thickness of an anisotropic crystalline material, e.g. GaAs, the effects of phonon focusing must be applied, transforming the angular distribution of phonon wavevectors (which run parallel to the phonon phase velocity) into a distribution of phonon group velocities.

Figures 3.14 to *3.17* show the angular distributions of the total emitted phonon power from a hot 2DEG QW (w = 6.8nm, $N_s = 2 \times 10^{15} m^{-2}$), where the θ- axis has been mapped onto a θ_V- axis, representing the direction of the phonon group velocity, for each of the coupling-mode combinations DP-LA, DP-TA , PZ-LA and PZ-TA, as before, as functions of (a) electron temperature T_e and (b) well width w.

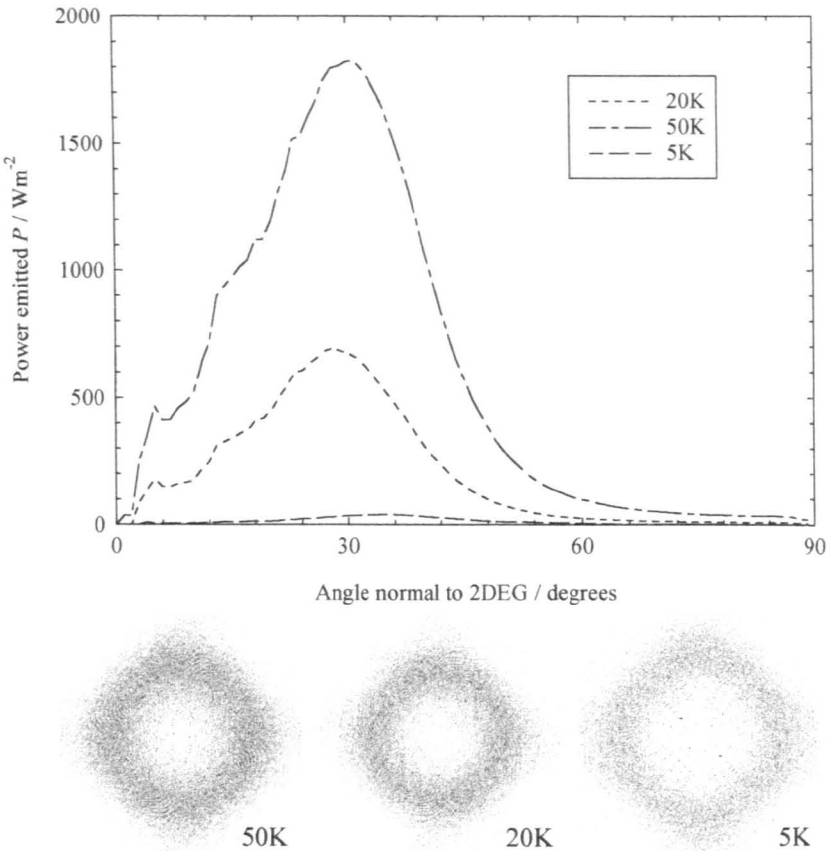

Figure 3.14 (a) : Angular distribution of detected DP-coupled LA phonon emission as a function of T_e at 50K, 20K and 5K. (w = 6.8nm)

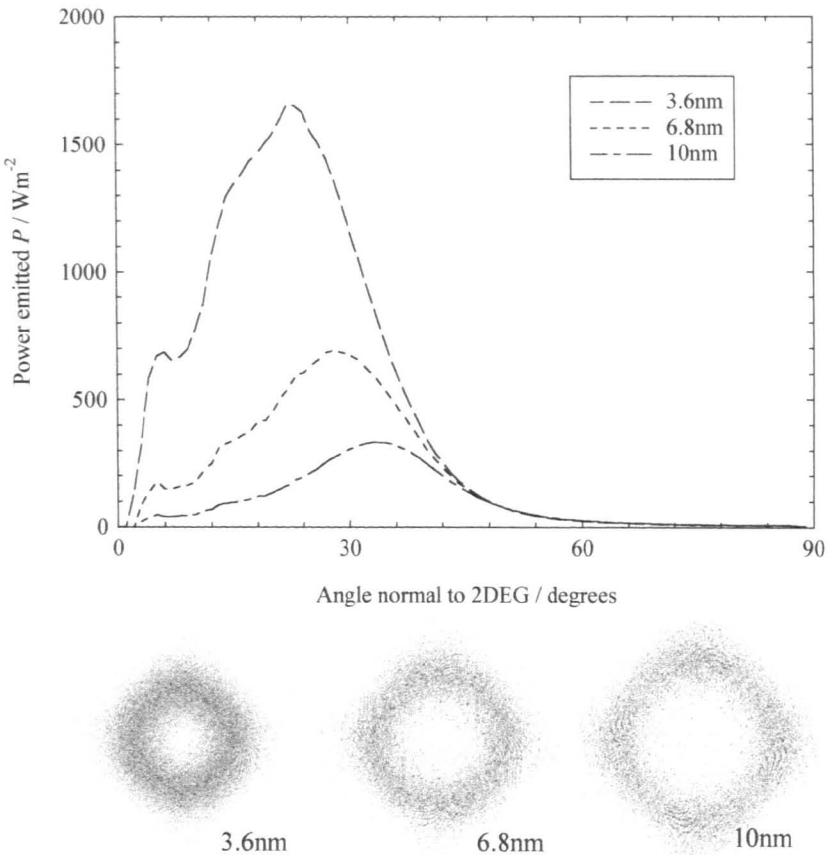

Figure 3.14 (b) : Angular distribution of detected DP-coupled LA phonon emission as a function of w at 3.6nm, 6.8nm, 10nm (T_e = 20K)

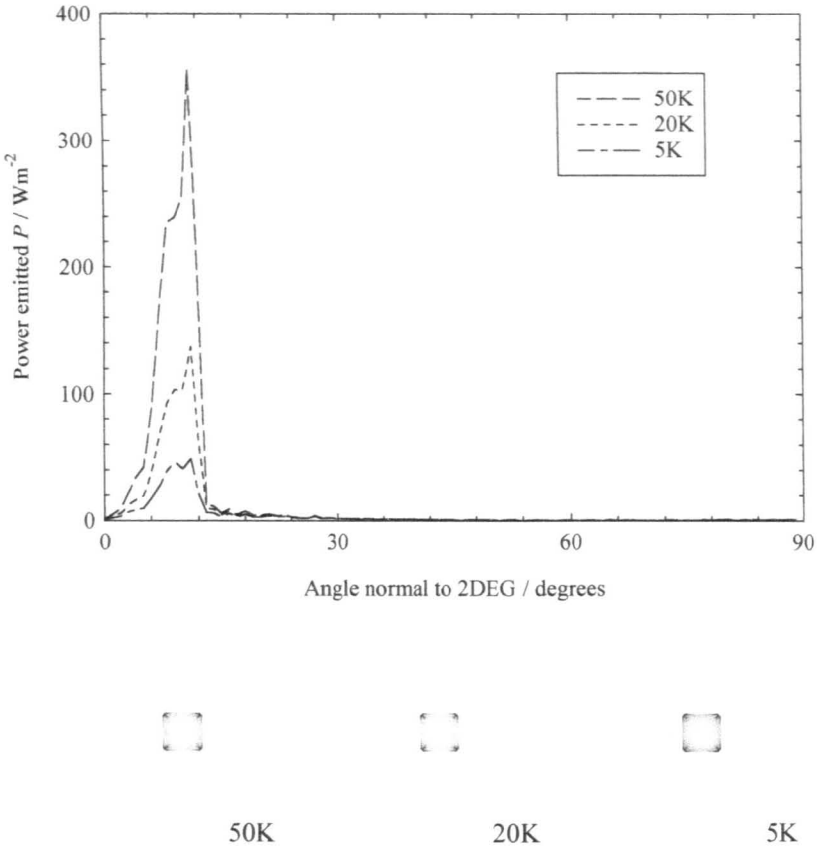

Figure 3.15 (a) : Angular distribution of detected DP-coupled TA phonon emission as a function of T_e at 50K, 20K and 5K. (w = 6.8nm)

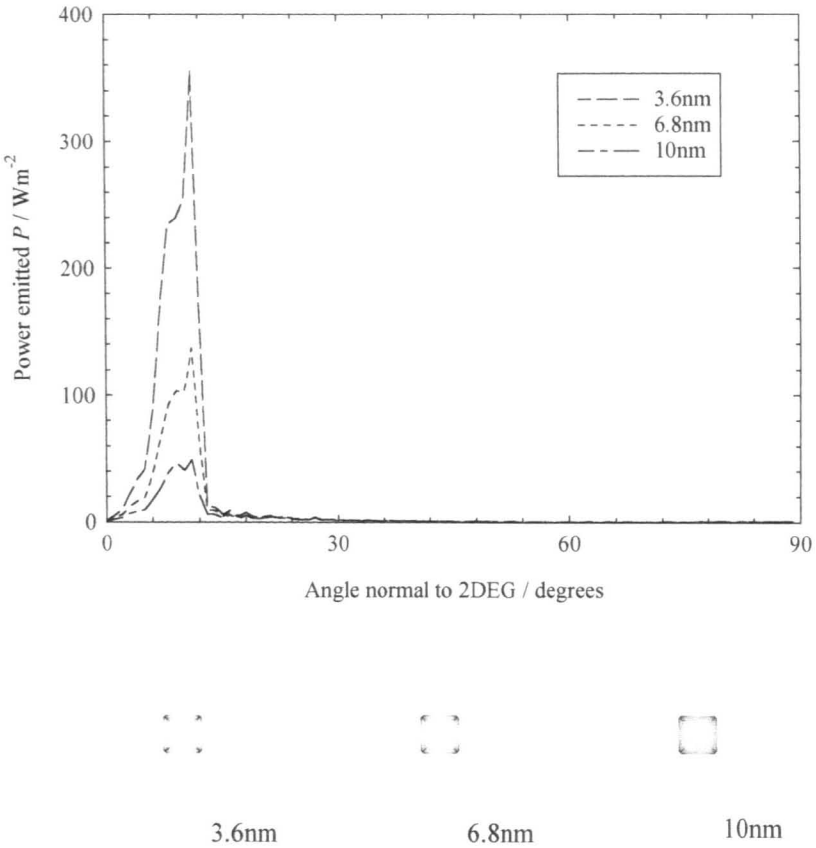

Figure 3.15 (b) : Angular distribution of detected DP-coupled TA phonon emission as a function of w at 3.6nm, 6.8nm, 10nm (T_e = 20K)

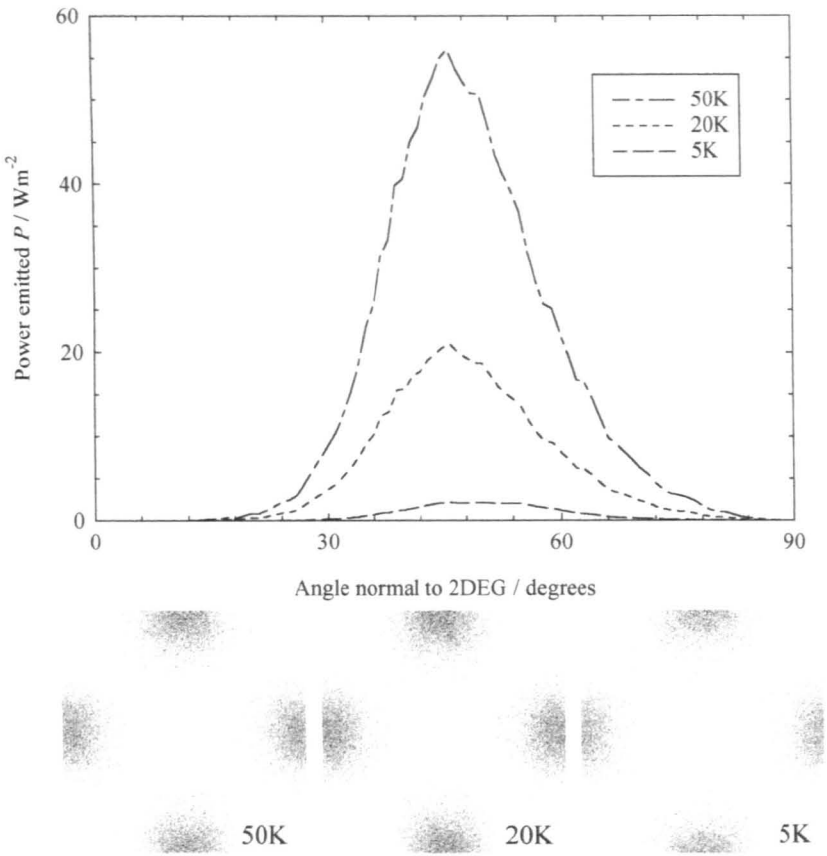

Figure 3.16 (a) : Angular distribution of detected PZ-coupled LA phonon emission as a function of T_e at 50K, 20K and 5K. (w = 6.8nm)

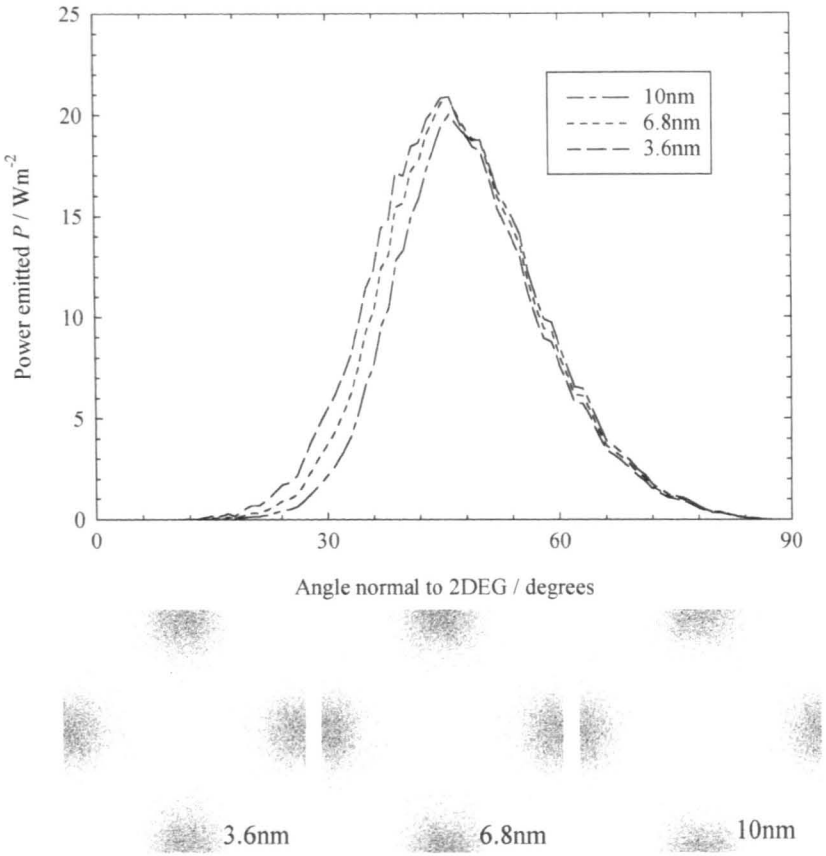

Figure 3.16 (b) : Angular distribution of detected PZ-coupled LA phonon emission as a function of w at 3.6nm, 6.8nm, 10nm (T_e = 20K)

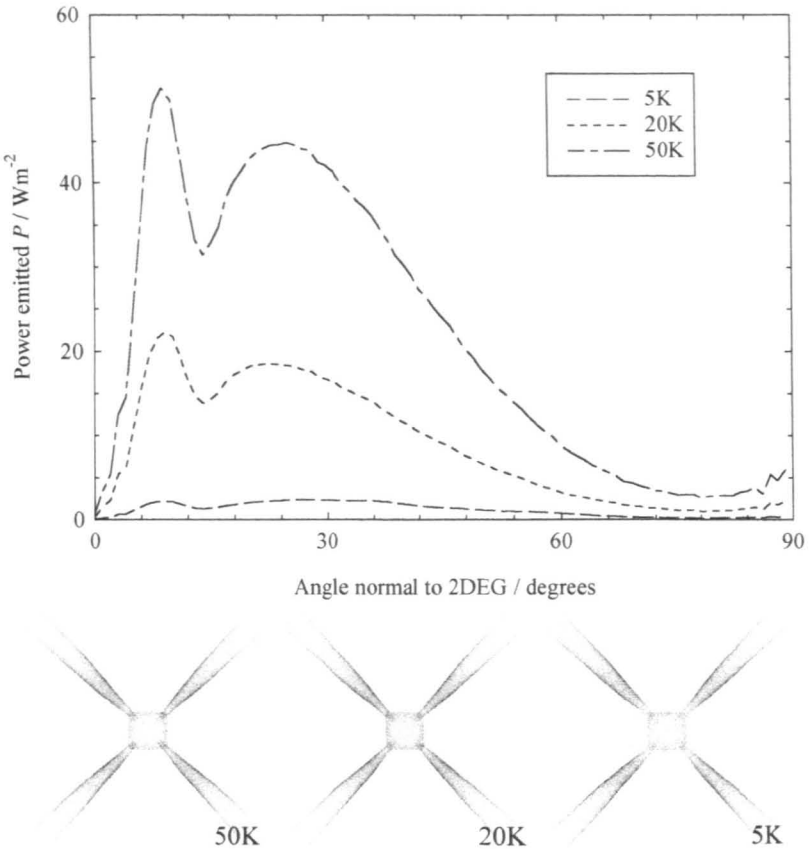

Figure 3.17 (a) : Angular distribution of detected PZ-coupled TA phonon emission as a function of T_e at 50K, 20K and 5K. (w = 6.8nm)

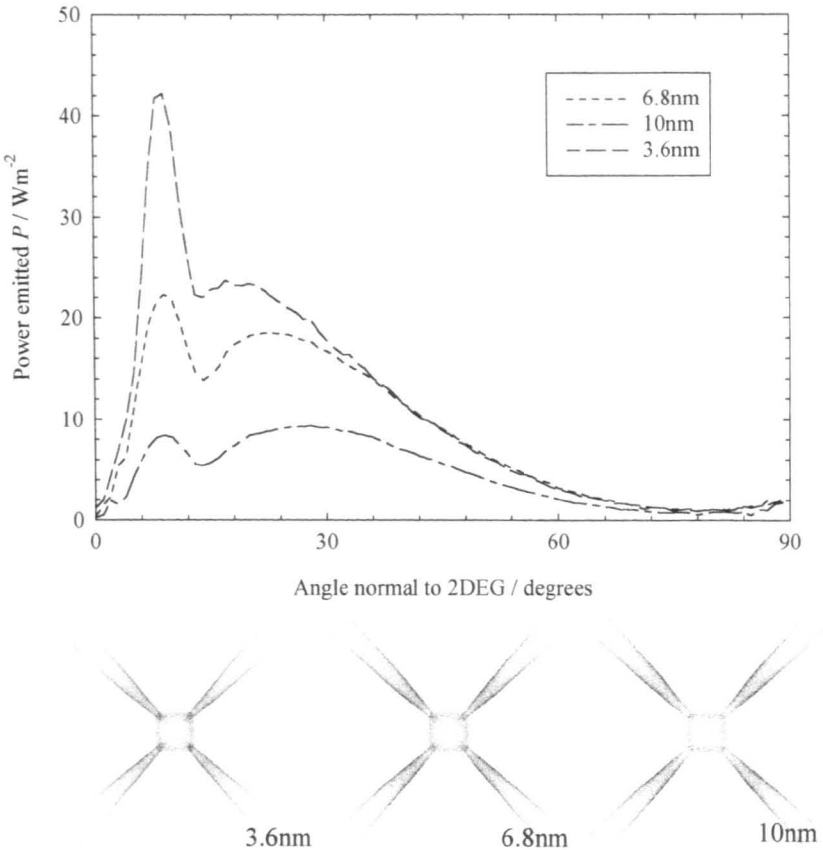

Figure 3.17 (b) : Angular distribution of detected PZ-coupled TA phonon emission as a function of w at 3.6nm, 6.8nm, 10nm (T_e = 20K)

An interesting feature of these graphs is that the shift in the peak of angular distribution as the well width, temperature and carrier density are changed is lessened. The focusing factor is sufficiently strong that these minor shifts are "washed out".

The DP LA "detected" (i.e. group velocity) angular distribution is similar to the "emitted" (phonon wavevector) distribution, but pushed out to a wider angle, due to the (111) focusing direction (~ 50 degrees to the normal) of LA modes. The "character" of the emission however is still evident in the images; the nature of the DP LA angular dependence of emission may be described as being "governed" by the electron-phonon interaction.

A sharp contrast is observed with the DP TA mode: the detected phonon pattern is qualitatively very similar for all temperatures and well widths, varying only in magnitude; the variation in peak angle observed in *Figure 3.11* above has been almost entirely neutralised by the very strong TA focusing towards the (100) direction. The angular dependence of emission for DP TA phonon modes is therefore governed by focusing, i.e. by the anisotropy of the crystal medium. The magnitude of the DP TA response, however, is determined by the details of the electron-phonon coupling.

One interesting point, however, is the absence of both the diagonal fast transverse and the "Maltese Cross" slow transverse caustic "arms" in the focusing pattern, due to the tight cone emission of the DP TA mode. This is due to the additive effect of the electron-phonon coupling and TA focusing, both pulling the emission in to very small angles normal to the 2DEG.

Similar uniformity is evident in the angular emission spectra for the PZ TA mode: the strong focusing of the TA phonons again cancels out much of the variation in angular dependence seen in the distribution of phonon wavevectors. Unlike the DP TA mode, the fast-TA diagonal arms are present, and indeed, enhanced relative to the remainder of the image, owing to the electron-phonon interaction emitting strongly in these directions. The

"Maltese Cross" slow-TA structure however is almost entirely missing, being only weakly visible in the 5K image. The fast-TA caustics run to larger angles at wider well widths, fading at smaller angles for narrower well widths. However, at lower well widths and higher temperatures, the fast TA diagonal arms are seen to extend inwards to smaller angles, impinging on the central slow-TA structure, as indicated by a small "shoulder" in the distribution graphs at an angle $\theta \sim 3°$.

As with the DP LA mode, the PZ LA detected emission pattern shows little difference from the phonon wavevector angular distribution, shifting slightly outward to angles close to the LA focusing direction. Consequently, the PZ LA emission will be of little further interest in this work: the results that will be presented are based on phonon time of flight experiments, in which the overall LA and TA emission strengths are considered; the PZ LA represents such a small fraction of the overall LA emission as to be essentially negligible, furthermore the experimental detectors are placed at angles less than 30°, where the emitted PZ LA power is virtually zero. Subsequent discussion will therefore largely omit detailed consideration of this mode.

3.4.2 Emission Power at Experimental Detectors

The integrated power at three small spatial windows corresponding to detectors used in an experimental study is considered briefly here, as a precursor to a detailed discussion in Chapter 5.

In the experiment, 100x10μm bolometers were positioned on the opposite face of a 380μm thick GaAs substrate, (a) directly opposite a 120x50μm area of active 2DEG, (b) 100μm distant along the (110) direction, corresponding to an angle of 14° normal to the 2DEG centre, and (c) 200μm distant along the (110) direction, an angle of 27°.

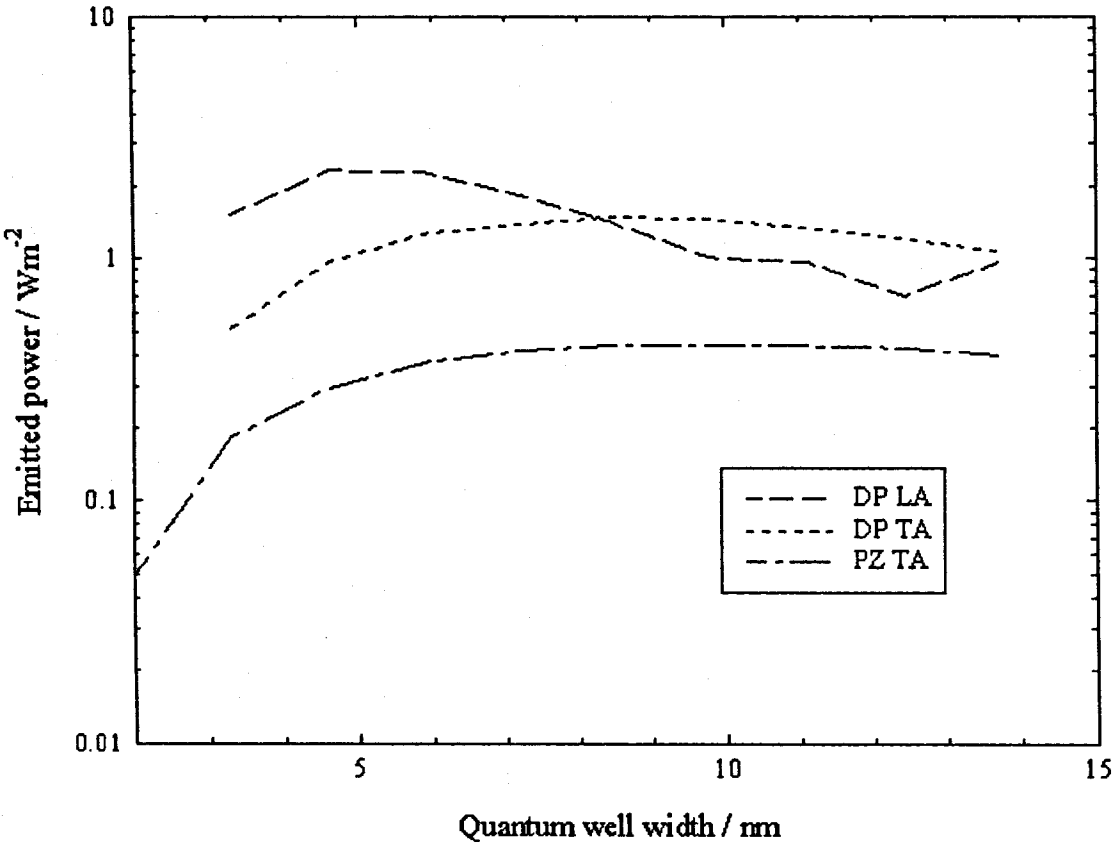

Figure 3.18: Emitted power detected at 100x10 μm bolometer opposite 120x50 μm source

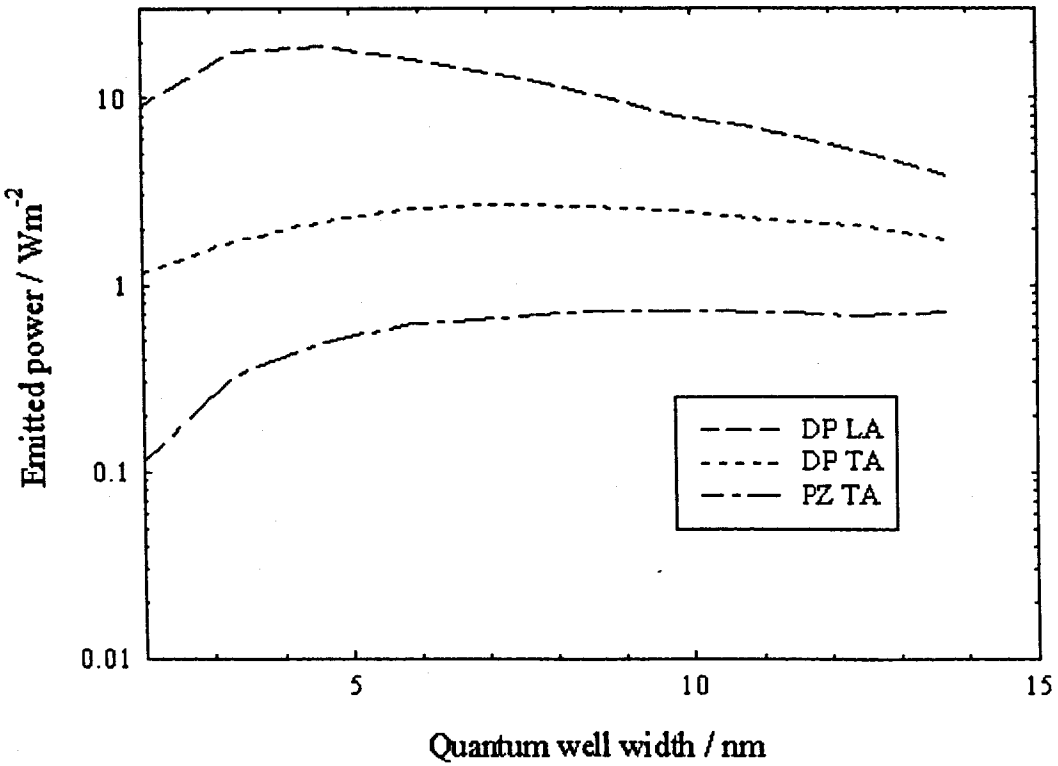

Figure 3.19: Emitted power detected at 100x10 μm bolometer at 14 degrees to 2DEG normal

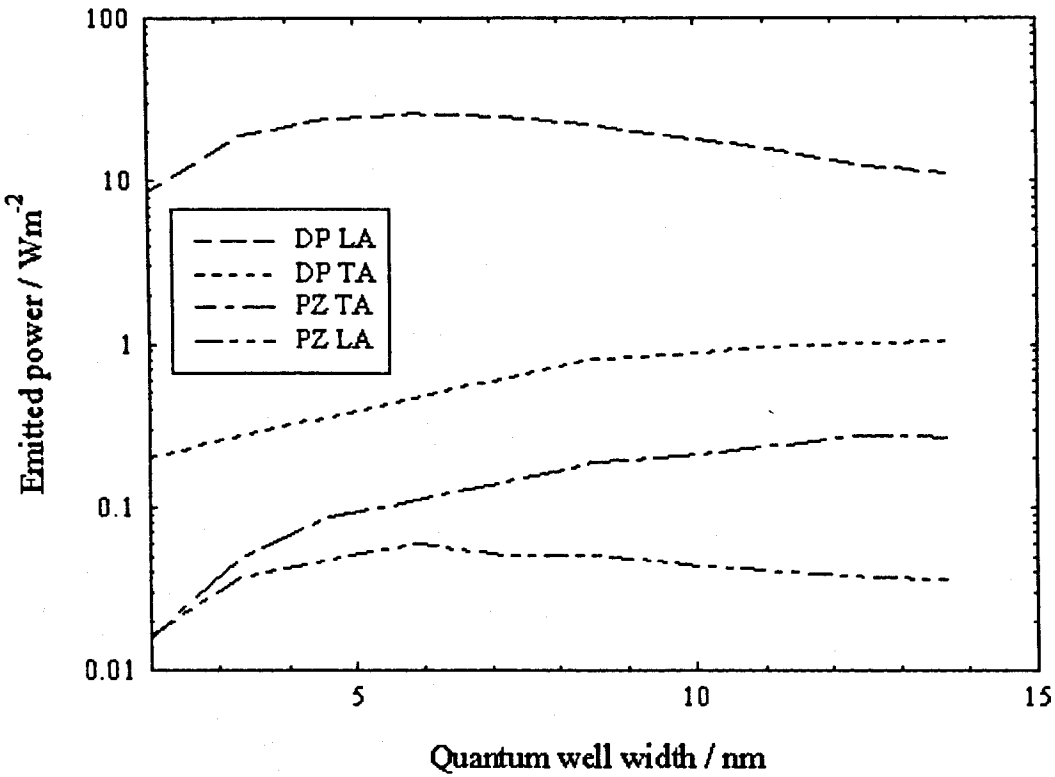

Figure 3.20: Emitted power detected at 100x10 μm detector at 28 degrees to 2DEG normal

Figure 3.18 shows the dependence of the phonon signal at detector (a) for the different modes and coupling mechanisms as a function of the QW width.

Here the electron temperature has been taken as T_e = 50K, and the carrier density $N_s = 2 \times 10^{15}$ m^{-2}. Of particular interest are the PZ-coupled LA modes, which are of negligible contribution to the overall detected emission, and the DP-coupled TA response, which in the isotropic theory approximation would be zero, and here is even stronger than the PZ-coupled TA emission.

These graphs confirm that in quantum well 2DEG devices, DP coupled LA phonons is expected to be the predominant mode detected using bolometers positioned opposite the 2DEG device, however the ratio of LA to TA modes, and of DP to PZ coupling, is strongly dependent on the well width, and therefore the carrier confinement potential. As the well narrows, so the $1/a_0$ cutoff becomes less strong. The overall emission rate increases and especially the emission into DP-coupled LA modes. At very narrow well widths, however, the effects of the penetration of the electron wavefunction into the GaAs/AlGaAs barriers cause an effective lessening of the confinement potential, resulting in a net reduction in the total energy relaxation rate.

As the detector is moved to a wider angle relative to the 2DEG normal (*Figures 3.19* and *3.20*), the emission becomes even more dominated by DP coupled LA modes. The PZ-coupled LA, while still some two orders of magnitude weaker, also strengthens. This shift towards stronger LA mode emission is consistent with the expectations of phonon focusing, as the detector is moved away from the TA-enhancing (100) direction and towards the (111) LA focusing direction.

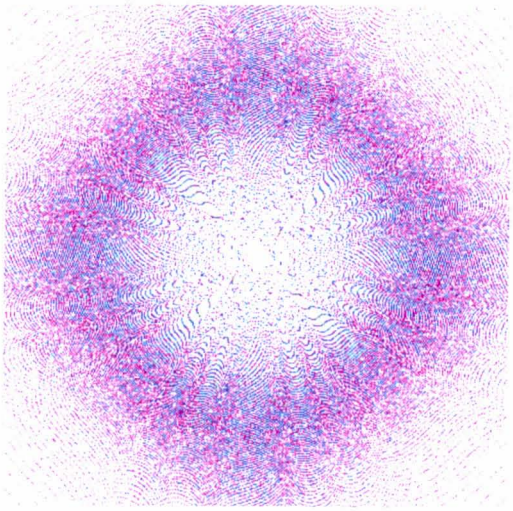

a) DP-coupled LA (0.793)

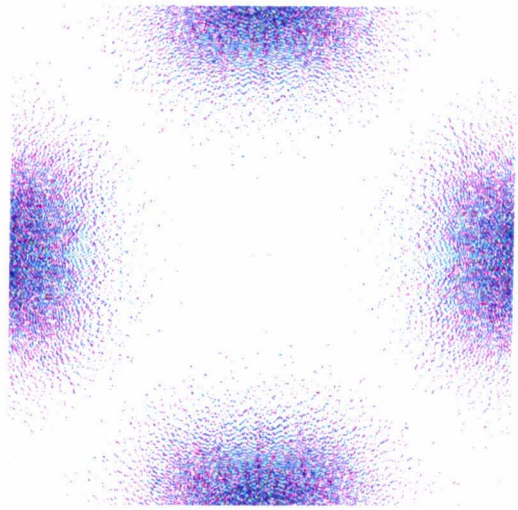

c) PZ-coupled LA (0.029)

b) DP-coupled TA (0.146)

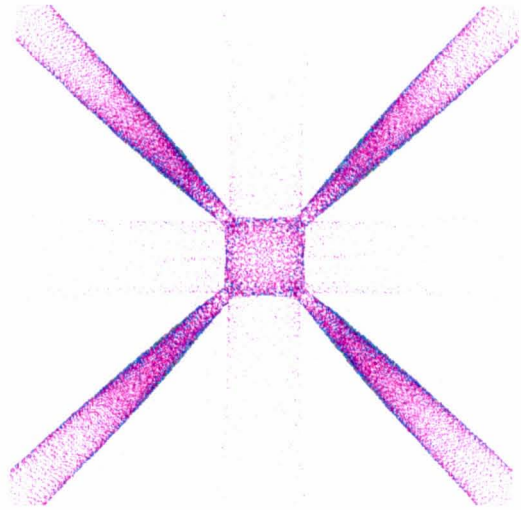

d) PZ-coupled TA (0.033)

Figure 3.21: Angular phonon emission distribution from 6.8nm QW, fully including the effects of matrix element anisotropy and dynamic Lindhard screening.

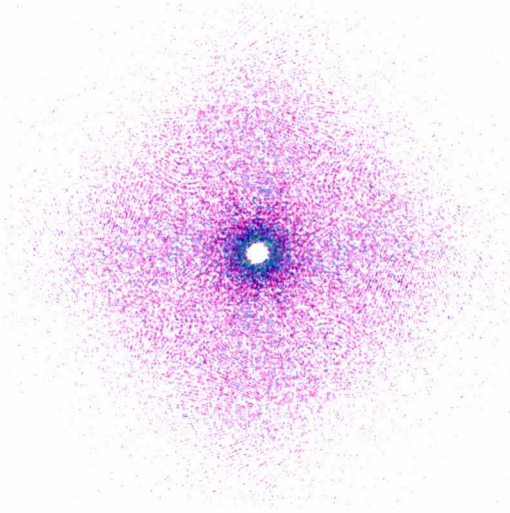

a) DP-coupled LA (0.828)

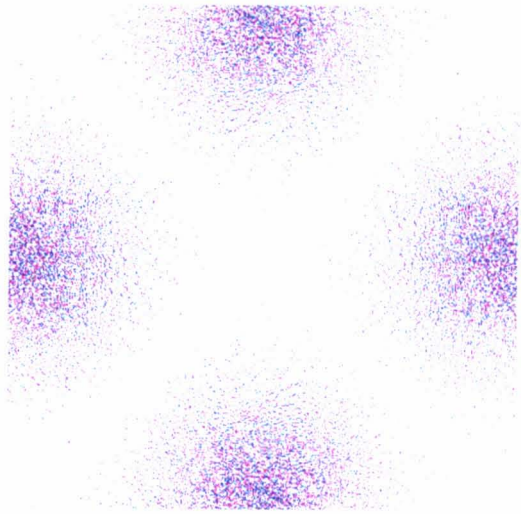

c) PZ-coupled LA (0.026)

b) DP-coupled TA (0.114)

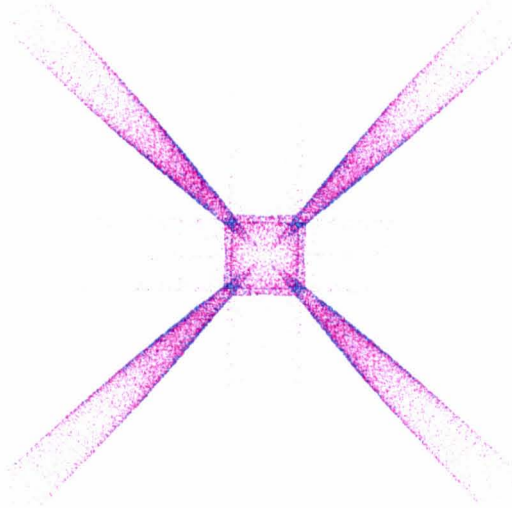

d) PZ-coupled TA (0.032)

Figure 3.22: Angular phonon emission distribution from 6.8nm QW, neglecting the effects of screening.

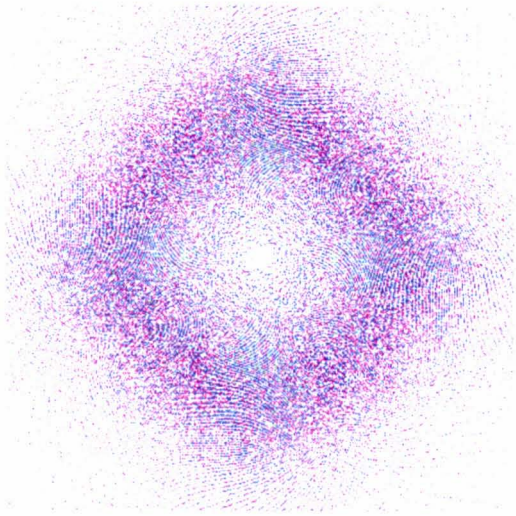

a) DP-coupled LA (0.917)

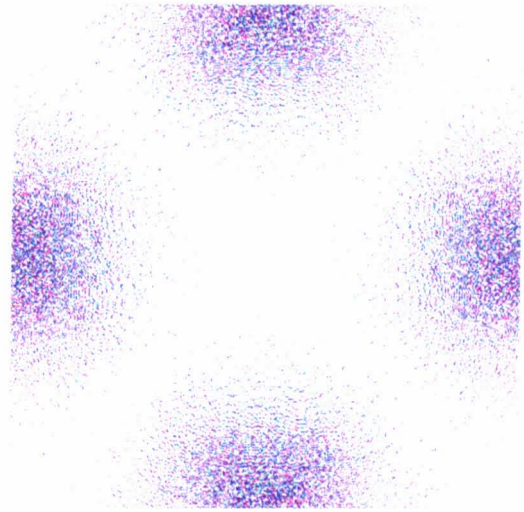

c) PZ-coupled LA (0.018)

b) DP-coupled TA (0.034)

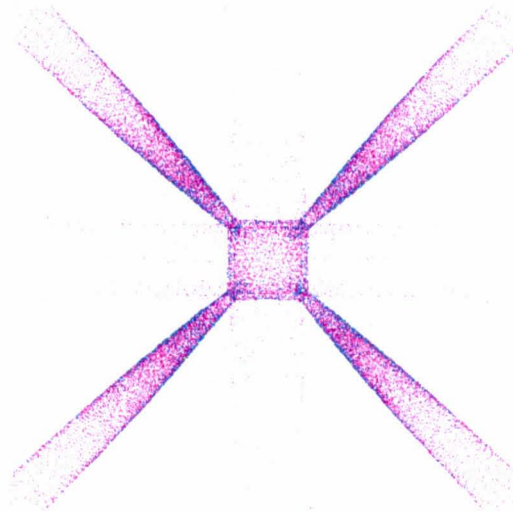

d) PZ-coupled TA (0.030)

Figure 3.23: Angular phonon emission distribution from 6.8nm QW, using the quasi-static screening approximation.

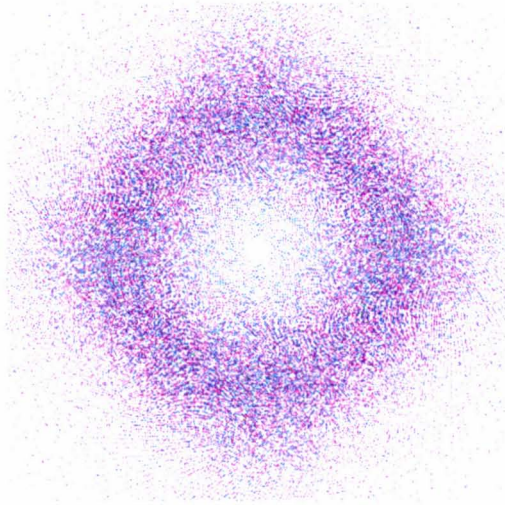

a) DP-coupled LA (0.917)

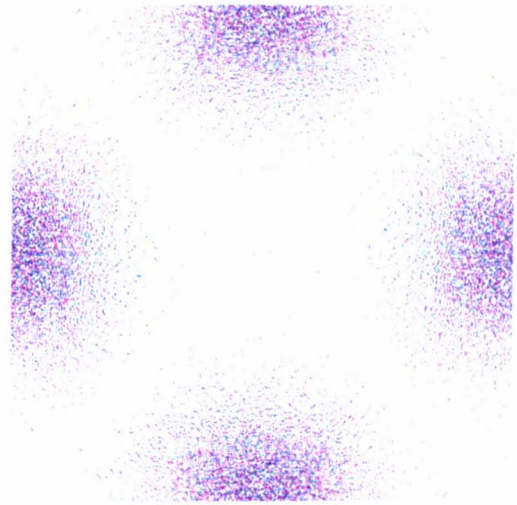

c) PZ-coupled LA (0.029)

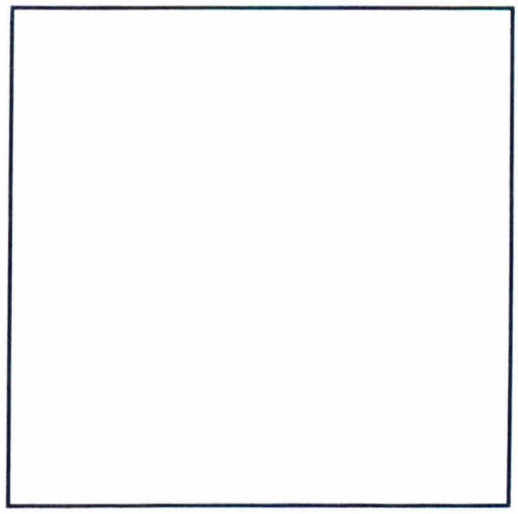

b) DP-coupled TA (0.000)

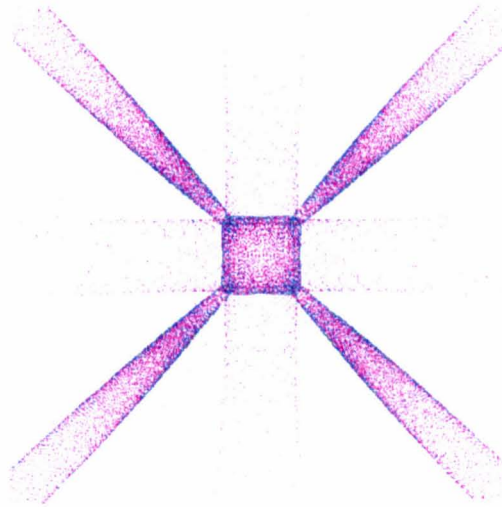

d) PZ-coupled TA (0.054)

Figure 3.24: Angular phonon emission distribution from 6.8nm QW, using isotropic electron-phonon coupling matrix elements.

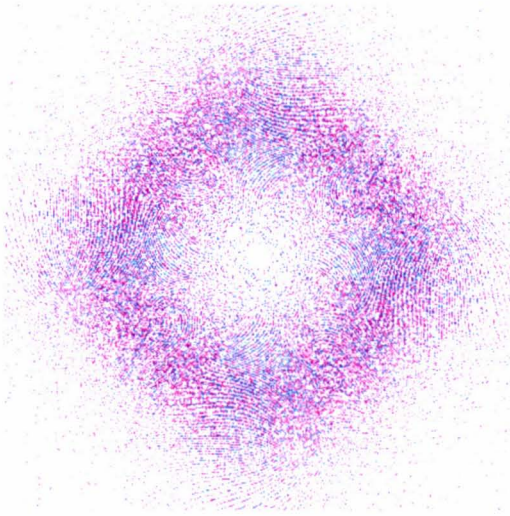

a) DP-coupled LA (0.794)

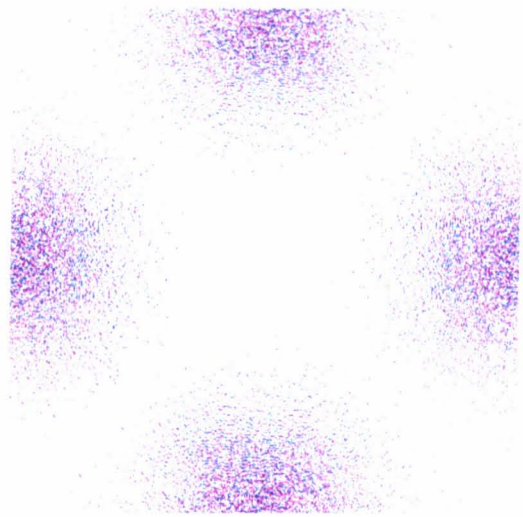

c) PZ-coupled LA (0.029)

b) DP-coupled TA (0.144)

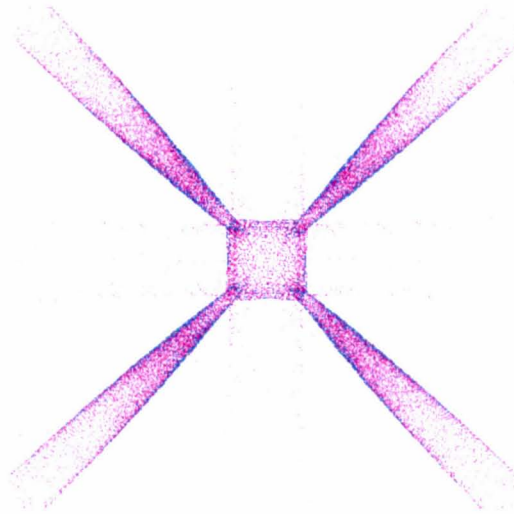

d) PZ-coupled TA (0.033)

Figure 3.25: Angular phonon emission distribution from 6.8nm QW, using an infinite-square well approximation for the calculation of the electron wavefunction.

3.5 Comparison of the Full Model with the "Classical" Model

Figures 3.21 to *3.25* show the phonon emission image for (a) DP-LA (b) DP-TA (c) PZ-LA and (d) PZ-TA modes, where *Figure 3.21* represents the full model of the electron-phonon interaction, *Figure 3.22* omits the interaction screening term, *Figure 3.23* uses a quasi-static screening term, *Figure 3.24*
makes the assumption of isotropic electron-phonon coupling matrix elements, and *Figure 3.25* assumes an infinite-height quantum well.

3.5.1 Importance of Screening the Interaction Potentials

The images show that screening of the electron-phonon interaction is especially significant in the case of the DP LA mode, reducing its overall intensity by a factor of ~7 at 20K, and also moving the distribution out to a far wider angle to the 2DEG normal. Many classical treatments of the electron-phonon interaction did not apply a screening treatment to the deformation potential, resulting in theoretical predictions of very strong DP LA emission close to the 2DEG normal, that conflicted with experimental observations. the so-called "missing LA mode". The screening term, therefore, provides much of the explanation of why the LA mode is not observed experimentally.

The screened images shown agree well with those obtained by Jasiukiewicz (1999) using a many-body screening approach, indicating that the Lindhard screening model gives an acceptable approximation. Furthermore, comparison of the images obtained with the Lindhard and quasi-static screening methods shows much similarity in the angular dependence, indicating that qualitatively, the quasi-static screening term is entirely reasonable for the screening of the interaction.

3.5.2 Importance of Matrix Element Anisotropy

As discussed above, in the isotropic matrix element approximation, the deformation potential may only couple to LA phonons. The images clearly

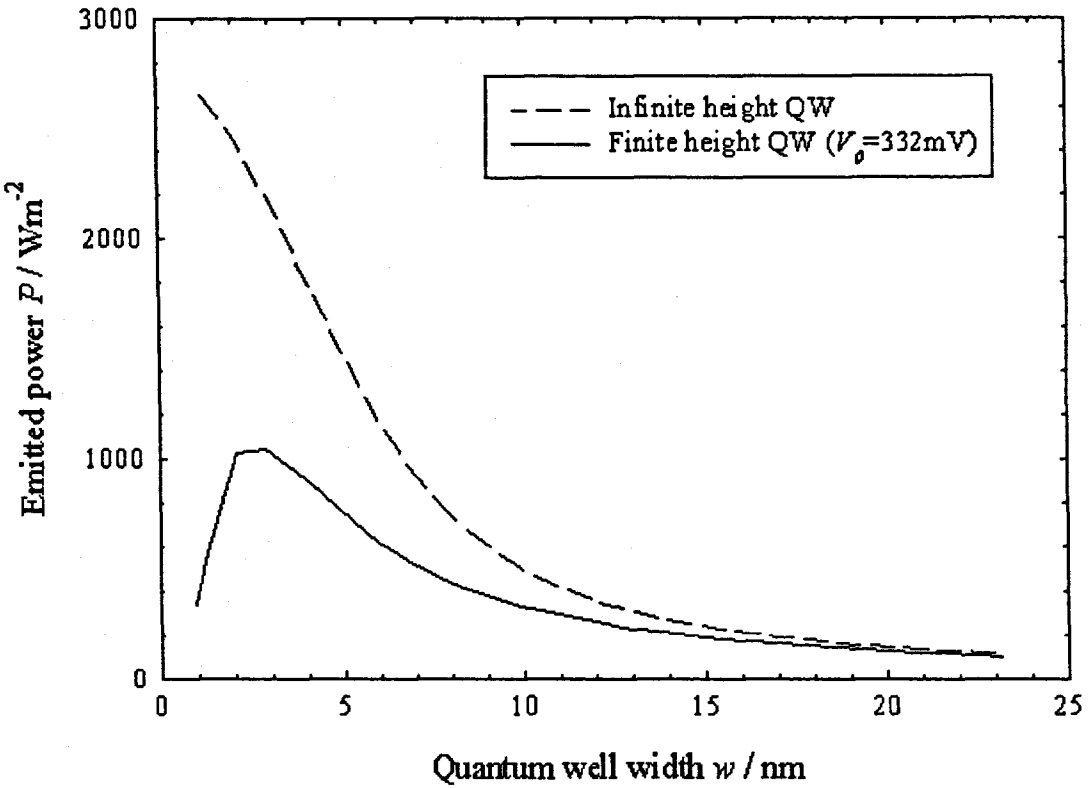

Figure 3.26 : Variation of total emitted power with well width for finite and infinite-height quantum wells (T_e = 20K)

indicate that in fact, DP-coupled TA phonon emission is highly significant, stronger than PZ-coupled TA emission for all but very low (T_e <1K) temperatures. Therefore the inclusion of matrix element anisotropy must be considered essential in a theoretical treatment of the electron-phonon interaction in which the ratio of LA to TA modes emitted is a subject of interest, particularly at small angles where the DP-coupled TA mode is strongly focused. *(Figure 3.15)*

3.5.3 Importance of Non-Infinite Quantum Well Potential Barrier

The infinite height approximation has been shown to have the effect of weakening the influence of the $1/a_0$ cutoff in the numerical calculations; from the form factors in *Figure 3.4* it is seen that the 6.8nm infinite height QW has a weaker $1/a_0$ cutoff than the 3.6nm finite well. As a result, the calculated relaxation rate due to DP-coupled LA phonon emission is considerably greater than for the finite-well approximation, and the emission is pushed to narrower angles. The infinite-well approximation therefore must be avoided if the ratio of LA to TA modes at small angles is of interest.

Additionally, as shown in *Figure 3.26*, the finite-height well approximation has the effect of reducing the total energy emitted from the 2DEG into all acoustic phonon modes and angles for very narrow well widths, w < 4nm. For such widths, the probability of electrons being found in the GaAs/(AlGa) interface is dramatically increased. The phonon scattering rate therefore tends towards the three-dimensional bulk value. This weaker electron confinement leads to a weakening of the electron-phonon coupling and thus the overall energy relaxation rate is reduced.

3.6 Conclusions

In quantum well devices, deformation potential coupled longitudinal acoustic phonons dominate the emission for most temperatures and well widths of interest in this study, as predicted by "classical" theory. However,

the magnitude of the LA signal is reduced considerably when screening and a non-infinite potential well approximation are used, suggesting that these factors should be included in the "classical" model in which the "missing" LA mode was predicted theoretically but not observed experimentally in heterojunctions.

The DP-coupled TA mode, zero in isotropic matrix element approach, is in fact a significant contributor to the total emission.

The DP-coupled LA mode shows strong variation in peak angle with well width and temperature, both at the emission source and after focusing, at the detector, due to the weakness of the LA focusing term. This mode may therefore be considered to be "mobile".

Transverse acoustic modes, however, show little variation in the angular emission distribution observed at the detector, due to the strength of the focusing factor. These modes may therefore be considered as "static". However, the nature of the electron-phonon interaction does remove certain structures from the isotropic TA focusing pattern.

The PZ LA mode is so weak as to be safely considered negligible in consideration of the relaxation processes that are relevant to the experimental study presented in the following chapters.

Chapter 4

Device Fabrication and Experimental Technique

4 Device Fabrication and Experimental Technique

4.1 Introduction

In this chapter the techniques used to perform heat-pulse measurements of the acoustic phonon emission from GaAs/(AlGa)As quantum wells are outlined.

The low-temperature experimental arrangement is discussed, along with a review of the methods used to acquire and process the phonon data. Finally, the steps involved in fabricating a 2DEG device from a MBE-grown GaAs quantum well 2DEG wafer are described.

4.2 Experimental Arrangement

4.2.1 Introduction

Figure 4.1 shows a schematic diagram of the system used to investigate the acoustic phonon emission from a 2DEG GaAs/(AlGa)As quantum well. The entire experimental apparatus, with the exception of the controlling computer and the data acquisition cards contained within it, is contained within a "screened room" – a metal cage that filters out external radio-frequency signals.

The 2DEG sample was held in a ^{4}He cryostat at a temperature of ~ 1.8 Kelvin, and excited by short duration, low power electrical pulses. These pulses were generated by a Philips PM5786B signal generator and fed through a programmable attenuator in order to reduce the signal by 0-63dB before feeding it into the device contacts.

Once excited by the pulse, the heated electrons in the 2DEG relax their energy through the emission of acoustic phonons, which propagate ballistically across the 380μm GaAs substrate, being detected at the opposite surface by an array of superconducting aluminium bolometers. The cryostat temperature is

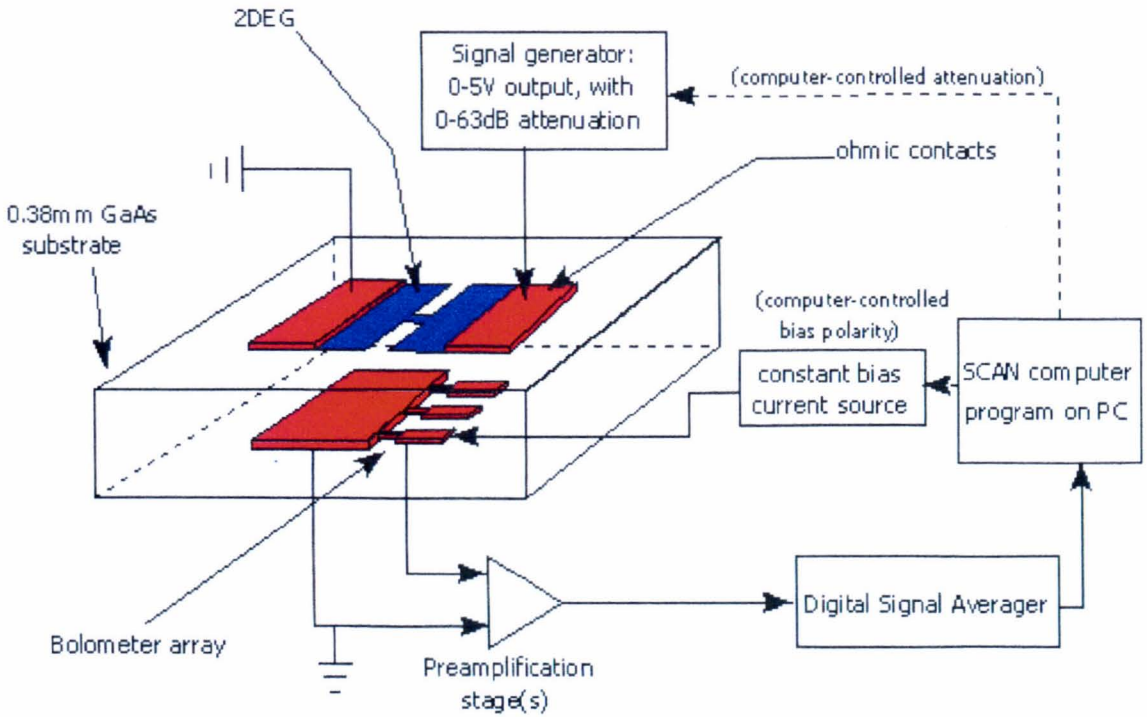

Figure 4.1: Schematic diagram of phonon emission experimental arrangement

regulated at the superconducting transition point of the bolometers, so that a slight warming caused by the arrival of phonons results in a measurable change in bolometer resistance. By applying a small (10-100μA) bias current through the bolometer, this resistance change results in a voltage pulse, which is amplified and fed into a digital signal averager.

By averaging a large number of such voltage pulses, the signal to noise ratio of the phonon time-of-flight signal is increased. Further improvement is made by subtracting traces obtained with positive and negative bolometer bias currents; with reverse bias applied, the phonon trace will be reversed, and thus be enhanced in the resultant trace. Signals arising from amplifier ringing or other electrostatic breakthrough, which can have a duration far in excess of the acoustic phonon rise time, will not be reversed, and so are cancelled out in the result trace, leaving only the desired phonon response.

The experiment was controlled by a PC computer and software package, SCAN, developed by the author during the first year of this PhD work. Most of the measurement and control instrumentation was linked on a IEEE-4888 network, enabling experiments to be automated. This network was controlled by a Brain Boxes PC-Elite IEEE interface bus, mounted on a standard ISA interface card inside the PC. Control of each device was performed by instructing it to become the active talker or listener on the network, and then either polling or writing to its data port. Each device supports two input/output streams: "Control", a command buffer for each device, and "Data". Communication between the PC and each device is achieved by sending a command to the control stream of a device, instructing it to become either a "listener" (ready to receive data), or a "talker" (ready to transmit data). The data stream of the device may then be addressed to send or receive the data itself.

4.2.2 Pulse Generation

Electrical pulses, typically of 10-20ns duration and 1μs period, were produced by a Philips PM5786B signal generator. In the experiments presented in this work, it is necessary to measure the phonon response as a function of input power, so a method of controlling the output signal amplitude accurately is required. As this feature is not supported by the PM5786B, a Pascall programmable attenuator was used for this purpose. This device precisely regulates the pulse power, by attenuating an input signal of up to 5V by a specified degree, from 0 to 63dB. The attenuation level is set through the digital output of a Stanford Research Systems SR245 computer module, which itself is controlled by the IEEE bus of the experimental control computer.

To calculate the power absorbed by the 2DEG sample for a particular attenuation level, the theory of acoustic mismatch is used; the heat pulse signal sent into the device is displayed on an oscilloscope, along with the signal reflected from the sample. The two signals are temporally resolved due to the longer distance travelled by the reflected pulse, and the absorbed power is calculated by the equation:

$$P_{abs} = \frac{V_{in}^{\,2} - V_{out}^{\,2}}{Z_o} \qquad (4.1)$$

To account for power loss within the length of the transmission cables (typically ~ 2 metres, including forward and reflected travel), the above equation was also used to measure the incident and reflected powers when the co-axial cable connected to the 2DEG device is instead replaced by a "null" connection, i.e. the signal passes down the co-axial cable and is reflected directly back, without any power absorption from a resistive device. The small

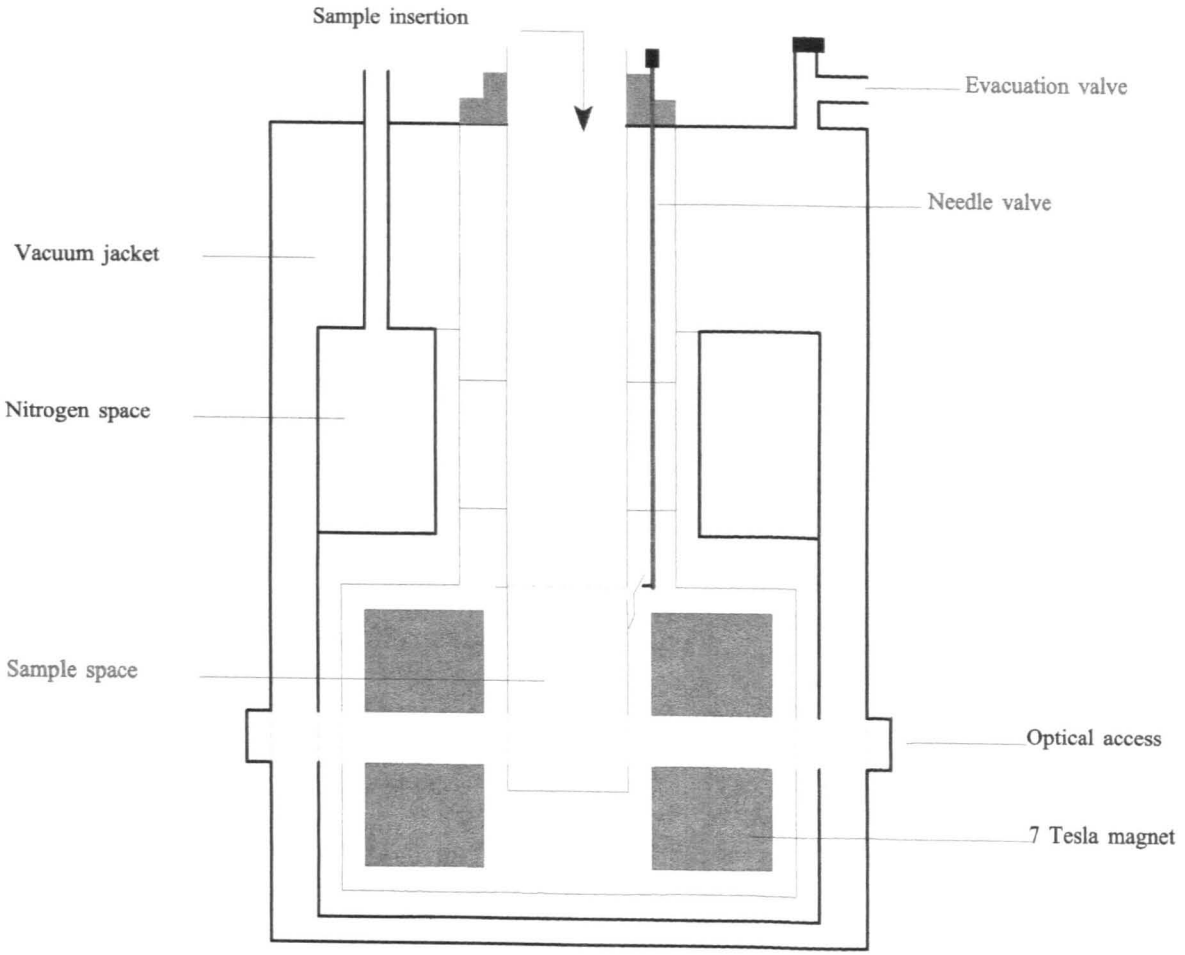

Figure 4.2: Oxford Spectromag cryostat arrangement

cable loss measured was offset from the power absorption values above, when calculating the power input into the 2DEG.

4.2.3 Cryogenic System

The phonon emission experiments were carried out at low temperatures of ~1.5K. At this temperature, the phonon mean free path is large compared to the sample dimensions, and so propagation is ballistic. For the purpose of maintaining such temperatures, an Oxford Instruments Spectromag 3 ^{4}He cryostat, adapted for optical access, was used. The cryostat schematic arrangement is shown in *Figure 4.2.*

The cryostat has a tail set, accommodating a 7 Tesla superconducting split-pair magnet, and a sample space, which can be varied in temperature by using a rotary pump to alter the vapour pressure of the liquid helium contained within.

Liquid helium is drawn slowly into the sample space from the main reservoir through a externally regulated needle valve: by carefully controlling the flow of helium, temperatures between 1.2K and 4.2K may be obtained, and operation in helium vapour as well as helium liquid is possible.

Pumping of the helium vapour pressure was performed under manostat control, allowing the temperature to be stablised to a high degree of precision, providing that the level of helium in the sample space remains approximately constant. For this reason, the tail of the sample space is enlarged, to give an increased volume of helium, which allows an extended operating time at the base temperature.

Optical access to the cryostat takes the form of a pair of quartz windows to the sample space, which in turn are aligned with similar windows in the outer shield. The outer windows can be covered, to prevent the exposure of light to samples where it is not desired.

To prevent the liquid helium in the cryostat from rapidly boiling off, a series of insulating measures are used. A radiation shield surrounds the main helium space, which in turn is cooled by a jacket of liquid nitrogen. To further reduce heat leaks, an outer vacuum jacket is pumped to a pressure of 10^{-6} Torr, to lower the effect of gaseous conduction.

Insertion of samples into the cryostat is performed by means of a "dipstick", a long, thin, stainless steel rod that sits in the main sample space of the cryostat, which is lowered into position from above. *Figure 4.3* shows a schematic diagram of a sample mounted in the dipstick.

The top of the dipstick is sealed firmly into position with a brass flange and O-ring. A miniature co-axial cable, wrapped around the dipstick in a coiled fashion, is used to input a heat pulse to the 2DEG device. Additional co-axial cables connect to the bolometers to measure the phonon time-of-flight response, and to to an Allen-Bradley resistor, which is used to monitor the temperature inside the cryostat. In addition to the insulating measures built into the cryostat design, to further minimise the loss of helium vapour into the column where the dipstick resides, a sequence of insulating baffle plates are positioned along the length of the stick. Samples are mounted onto a 16-pin chip carrier, then plugged into a standard integrated chip socket positioned at the bottom of the dipstick, aligned with the cryostat window, allowing optical access to the sample, should it be required.

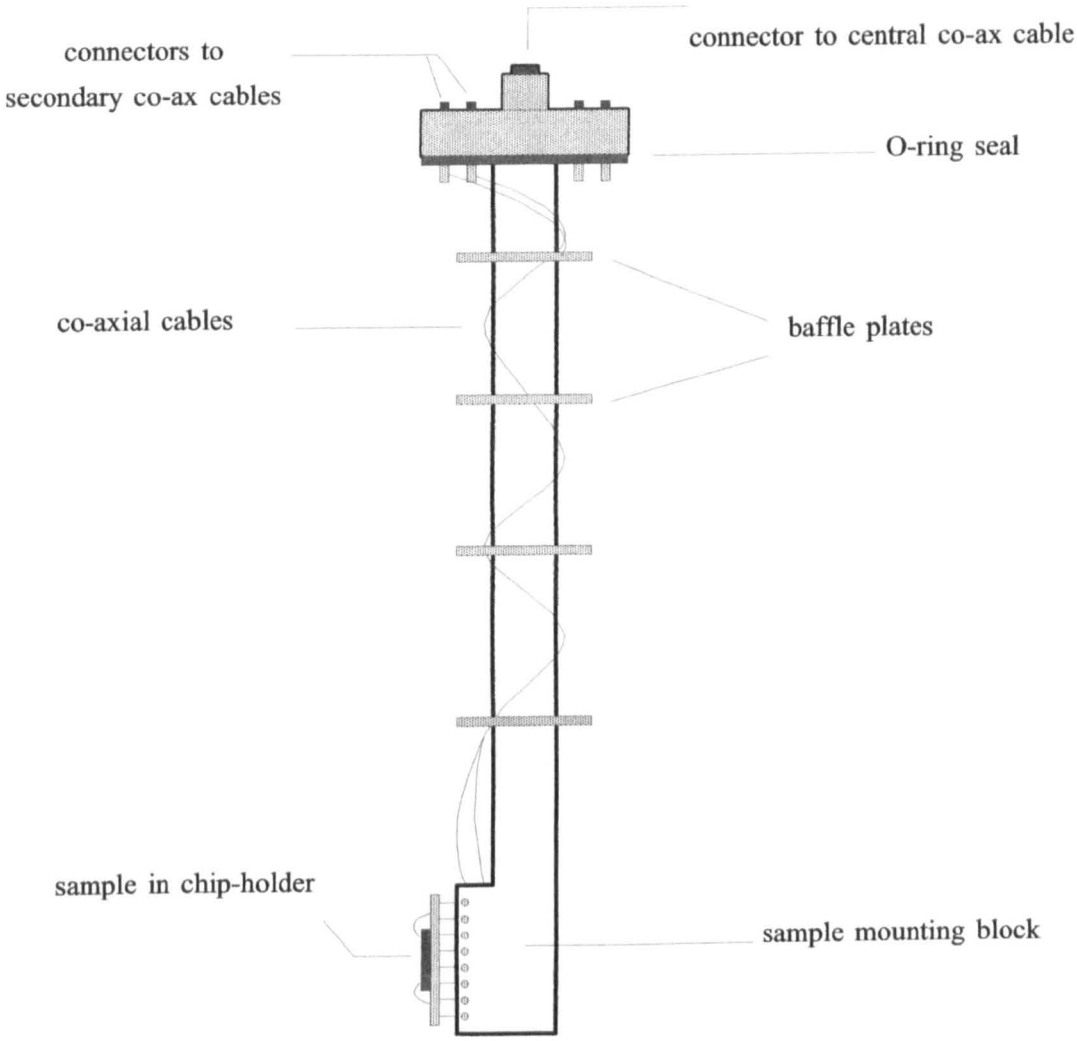

Figure 4.3: Schematic diagram of dipstick

4.2.4 Amplification and Transmission of Signals

The main preamplifier used in the phonon emission experiment had an input impedance of 50Ω, closely matched to the 4.2K impedance of the aluminium film bolometers used for phonon detection. The amplifier had a x20 gain, with a bandwidth of 4kHz - 5MHz.

Further amplification was provided by a series of x5 broadband (DC to 300MHz) amplifiers in a Stanford Research Systems SR240 fast preamplifier. These amplification stages could be added or removed depending on the magnitude of the detected phonon response.

The amplified signal is then fed out of the radio-frequency screened room through a fast opto-coupler network designed and constructed by Dr. P. Hawker, into the inputs of a fast digital signal averager, for storage and display on the experimental control PC. The opto-coupler network is also used to transmit IEEE network and serial-port signals in and out of the screened room.

4.3 Acquisition and Processing of Experimental Data

4.3.1 Data Acquisition with the EG&G Averager and SCAN Program

The phonon emission traces received from the experimental arrangement were processed by an EG&G Instruments 9826 Digital Signal Averager board, mounted on two ISA cards inside a Pentium PC computer. The averaging board (hereafter referred to as the "digitiser") is able to acquire 16,384 discrete signals in its onboard memory and return an averaged trace of 16-bit precision to a user-written control software program.

By adding a "software averaging" routine to this "hardware averaging" of the digitiser, many signals may be obtained and averaged to give a final trace with a high signal-to-noise ratio. With a very short "dead-time", i.e. a high-frequency input pulse, averaging speeds of 30-40,000 traces per second were achieved on this system, with a temporal resolution of 2ns.

4.3.2 Experimental Control Software: the SCAN program

The software package SCAN (*Figure 4.4*) was written and developed by the author during the first two years of his PhD, as a flexible and robust program suite for the control of, and data acquisition from, the experimental apparatus described above. Other than the emission experiments presented in this thesis, the software was also used to control time-of-flight spectroscopy and laser-imaged experiments in other areas of phonon imaging; for instance in the study of one- and zero-dimensional carrier systems (quantum wires and dots). Some extra functionality was incorporated into the software to adapt it for these purposes: for example, the ability to set a Schottky-gate depletion voltage for pinching off a 2D channel into a quasi-1D wire, as in Naylor (1998).

The SCAN program was written primarily using Microsoft Visual Basic 3.0 for Windows 3.1/95, using a modular "form-based" approach. The user interface of the program is therefore highly intuitive, with separate form modules for each of the main data acquisition options (two variable (XY) scatter graph, image acquisition, digitiser trace acquisition), and for setting up the parameters of each computer-controlled hardware instrument. New form modules, for example to accommodate a new piece of instrumentation, can be incorporated easily. A menu control enables all these forms to be navigated without difficulty.

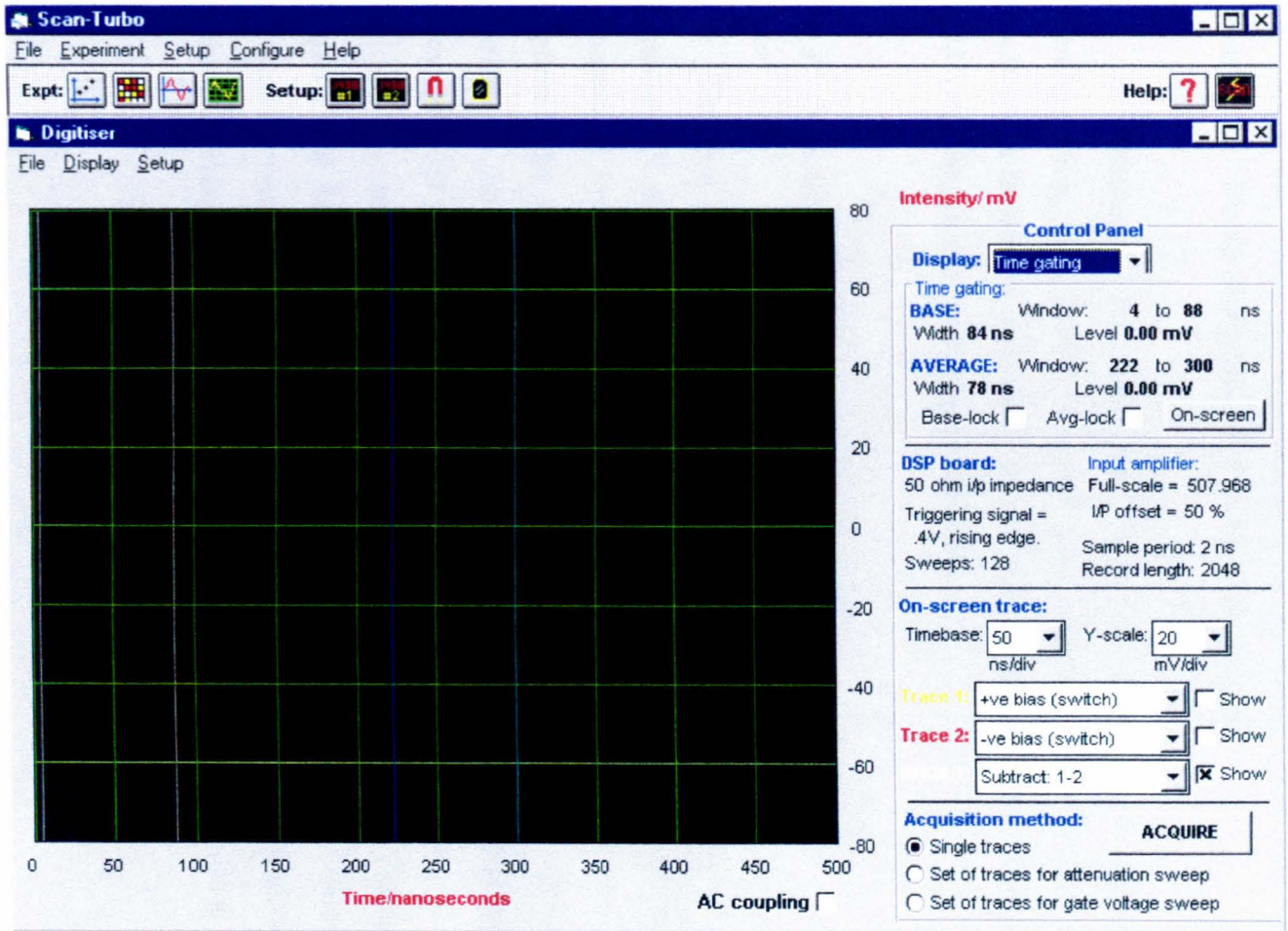

Figure 4.4: Digitiser trace acquisition with SCAN program

For direct input/output (I/O) port functions, such as writing and reading parameters and data to and from the IEEE bus and digitiser *(Figure 4.6)*, as well as some speed-critical subroutines, e.g. additional software-averaging of digitiser traces, the main Visual Basic SCAN application was supplemented by a set of routines written in the C language, and compiled into a dynamic link library (DLL) file that could be called by the main program.

In addition to the IEEE and direct I/O methods of controlling instrumentation, the SCAN program also supports RS232 serial port input/output, in order to control two precise galvanometer mirrors that position a Nd/Yag laser, used for imaging experiments.

4.3.3 Data Acquisition Options

The data obtained by the SCAN program is typically in one of three forms: an XY plot of two variables, e.g. a resistance-temperature graph; a two-dimensional image acquired by a laser scan, and a time-response trace acquired from the digitiser. These three methods are treated as individual modules in the program, though there is considerable interleaving of the methods: a 2D phonon image, for instance, may be generated using a gated digitiser trace as the source of the intensity values at each point. Similarly a linescan may be taken through the completed image, requiring interaction between the Image and XY plot modules. Such functionality is obtained using global variables and routines to pass data between the modules concerned.

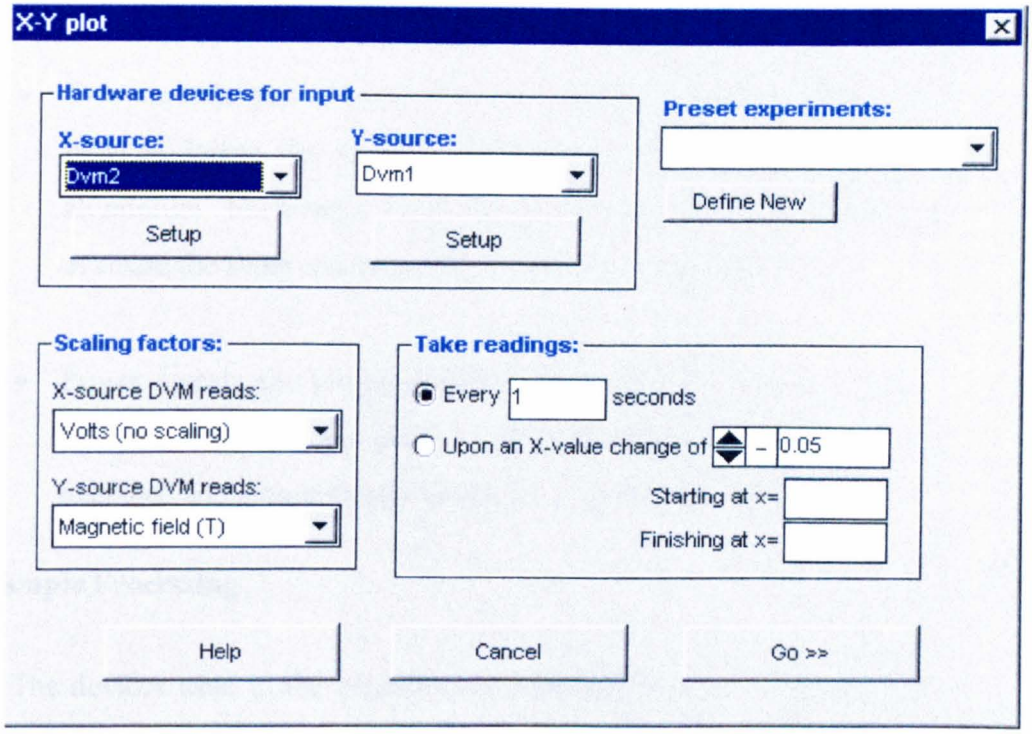

Figure 4.5: Setting up a 2-variable plot with the SCAN program

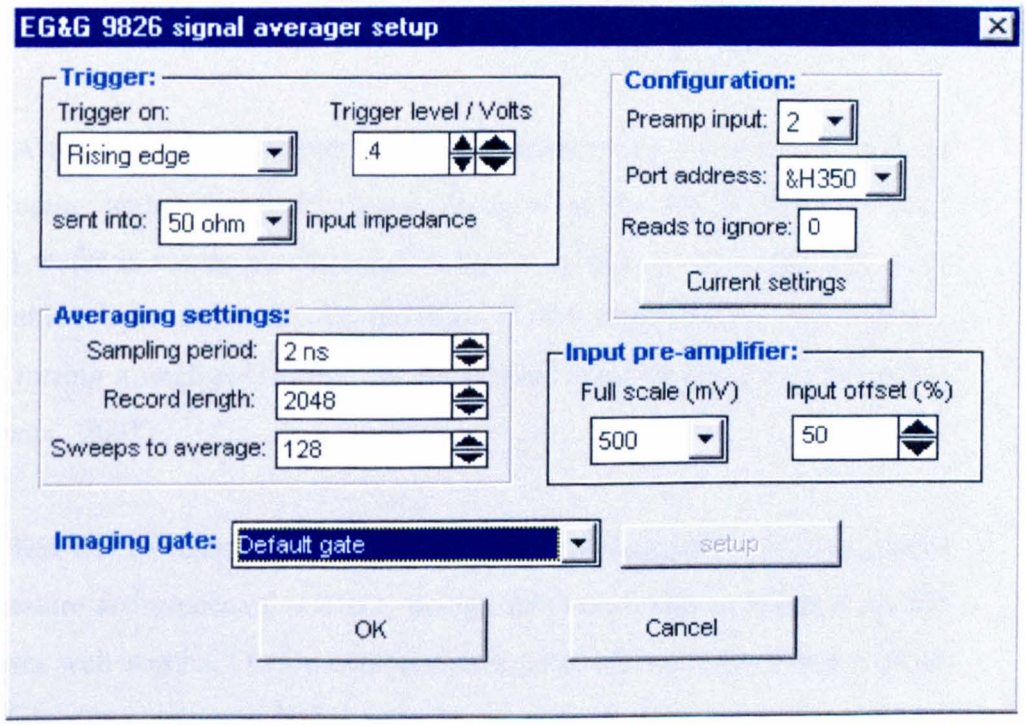

Figure 4.6: Setting up the digitiser parameters with the SCAN program

The most used functionality in the present work was:

- Two-variable plot (*Figure 4.5)* for example, resistance-temperature plots to locate the superconducting transition temperature of the aluminium bolometers, and resistance-magnetic field plots, to evaluate the sheet carrier density of the 2DEG samples.

- Power sweep: the programmable attenuator is set to vary between 0dB and 63dB, with a phonon traces being acquired (*Figure 4.4*), averaged and automatically saved, for each attenuation level.

4.4 Sample Processing

The devices used in the experiments presented here were *n*-type single GaAs/AlGaAs quantum well structures, grown by Molecular Beam Epitaxy (MBE) on the (100) plane of semi-insulating, chromium-free 380μm GaAs substrates, in the facilities of the Nottingham University Molecular Beam Epitaxy Syndicate (NUMBERS).

A two-dimensional electron gas was achieved in the quantum well by side-doping with silicon. The layer structure of the NU667S (12nm well width) wafer is shown in *Figure 4.7*, and is typical of all those used. The superlattice layer improves the mobility of the modulation-doped carriers, while having a negligible effect on the emitted acoustic phonons. (A.J.Kent, *pri.comm.*, 2001)

The device shapes were defined by photolithography, and had room temperature resistances of $\approx 20k\Omega$, though this was found to increase for the narrower well widths. Ohmic contacts were used, allowing the contact metal to diffuse down into the 2DEG in order to minimise the contact resistance. The resistance of the contacts must be low in comparison to the device resistance in order to eliminate the generation of phonons from the contacts due to heating effects. Typical contact resistances achieved with this technique were ~100Ω.

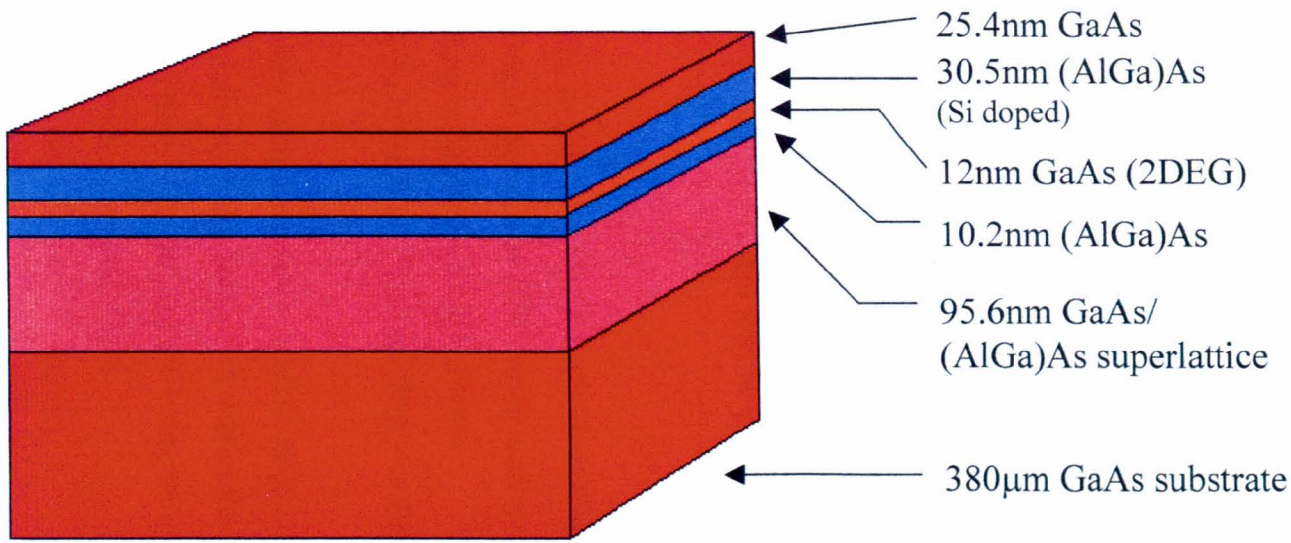

Figure 4.7: Schematic layer diagram of 12nm quantum well wafer (NU667)

A summary of the device manufacture process follows:

4.4.1 Cutting

The first step in the fabrication procedure involves cutting samples of the required size from the MBE-grown wafer. In these experiments, the typical surface dimensions of the samples used was 10mm x 10mm. For (100)-grown GaAs on a 380μm substrate, the cutting process involves cleaving the substrate along a preferential breaking direction of the crystal with a diamond-tipped scriber, in a fume cupboard to protect against GaAs dust.

4.4.2 Cleaning

Prior to commencing the photolithographic mesa etch, the samples undergo a thorough four-stage "EAMI" solvent-clean to remove any dust, grease or other deposits that may be present on the surface of the crystal. This involves:

- Boiling in Ethyl Lactate at 120°C for 10 minutes,
- Heating in Acetone at 70°C for 10 minutes,
- Soaking in Methanol for 10 minutes,
- Soaking in Isopropyl Alcohol (IPA) for 10 minutes.

Between each successive cleaning stage, the samples undergo a two-stage rinse, initially with the solvent in which the cleaning process had just been completed, then with the next solvent, to prevent any cross-contamination occurring between cleaning stages.

An ultrasonic bath was also used as a "pre-clean" before heating the solvent in the first two stages, in order to loosen any surface residue, improving the effectiveness of the cleaning process.

The cleaning procedure is completed by drying the samples with a stream of nitrogen gas and baked at 120°C for 10 minutes to evaporate any excess solvent.

4.4.3 Photolithographic Etch

The structures required to make up devices for these experiments were defined using the technique of photolithography. This well-established process is able to define patterned features of the order of 1μm resolution, this limit being determined by the wavelength of visible light. In order to produce finer structures, electron-beam lithography may be used, however such high-definition was not required in this work.

As shown in *Figure 4.8*, the GaAs wafer is first coated with a photosensitive polymer, or "resist", which is applied to the device using a high-speed spin-coating technique. The devices are then baked before exposure.

To define the device shape, each sample is held in conformal contact with a patterned mask and exposed to collimated ultraviolet light. The masks, 5cm x 5cm glass plates containing an array of structures, as in *Figure 4.9*, were designed using WaveMaker, a PC-based computer-aided design package, and manufactured in the Central Microstructure Facility (CMF) of the Rutherford Appleton Laboratory (RAL), Oxfordshire, UK.

The masks were designed so as to enhance the resulting phonon emission signal, by using square ($1mm^2$) contact pads, well-separated from a 120x50μm rectangular 2DEG channel. The different geometry reduces the contact resistance relative to the device resistance, while the separation ensures that signals from the contacts will be temporally resolved from the device signal.

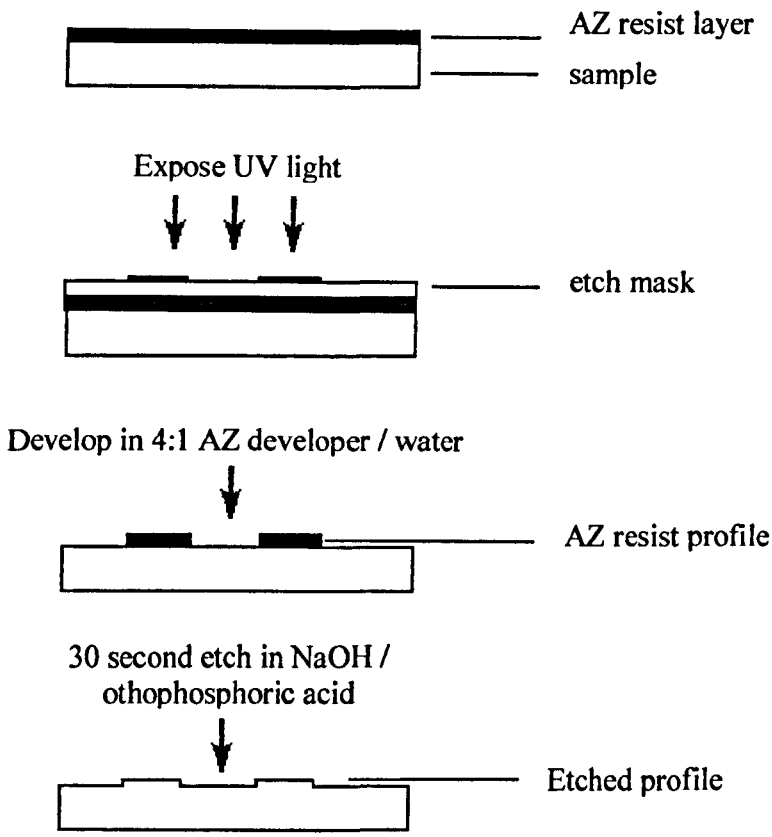

Figure 4.8 : Photolithographic process for etching 2DEG region

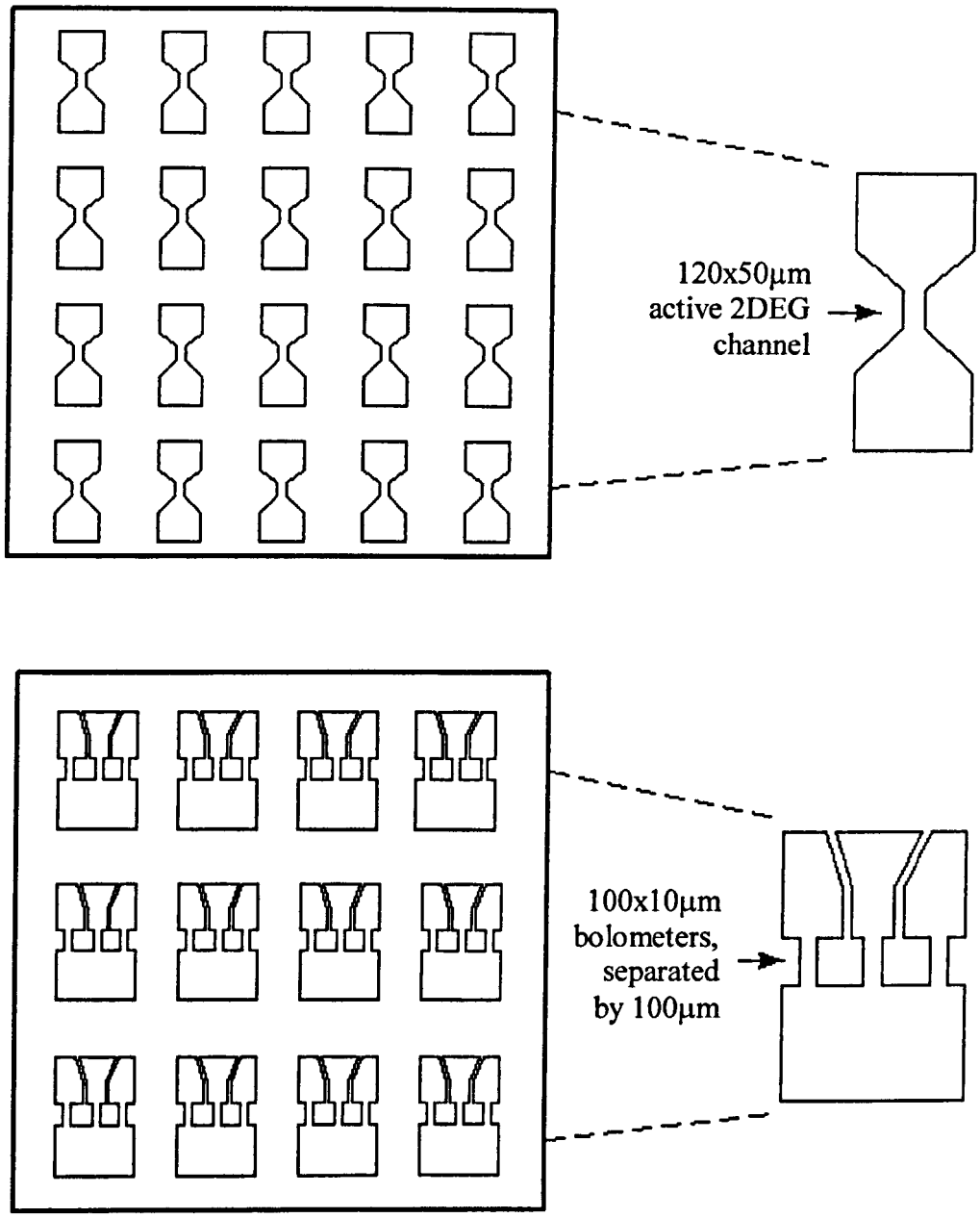

Figure 4.9: Photolithographic masks for (a) 2DEG active region and (b) aluminium bolometer array

After exposure to the ultra-violet light, the samples are developed in a chemical solvent, which selectively dissolves away regions of the resist polymer, conforming either to the masked region, in which case the resist is described as being a *negative* resist, or to the unmasked region (a *positive* resist). To improve the resist profile, a post-develop bake follows.

A wet chemical etch is used to define the structure. A 10:1 ratio of 30% by volume hydrogen-peroxide to 85% orthophosphoric acid produces the required etch depth, given a 30 second etch time.

4.4.4 Evaporation of contacts

The next stage in the sample fabrication process was to define and evaporate metallic contact pads, through which the 2DEG may be electrically pulsed. A region defining the contact areas was defined using resist (*Figure 4.10*), and exposed with UV light as described above. The sample was then placed into an high-vacuum Edwards evaporator and evacuated to a pressure of $\sim 10^{-7}$ Torr.

Layers of contact metal were then deposited onto the samples:

Metal	Thickness
Germanium	60nm
Gold	120nm
Nickel	40nm
Gold (capping layer)	200nm

Table 4.1: Metals used in contact evaporation

The contacts were then annealed, to drive the evaporated metal down into the 2DEG layer of the wafer, creating an ohmic contact. The samples were loaded into a chamber that was first evacuated and then filled with

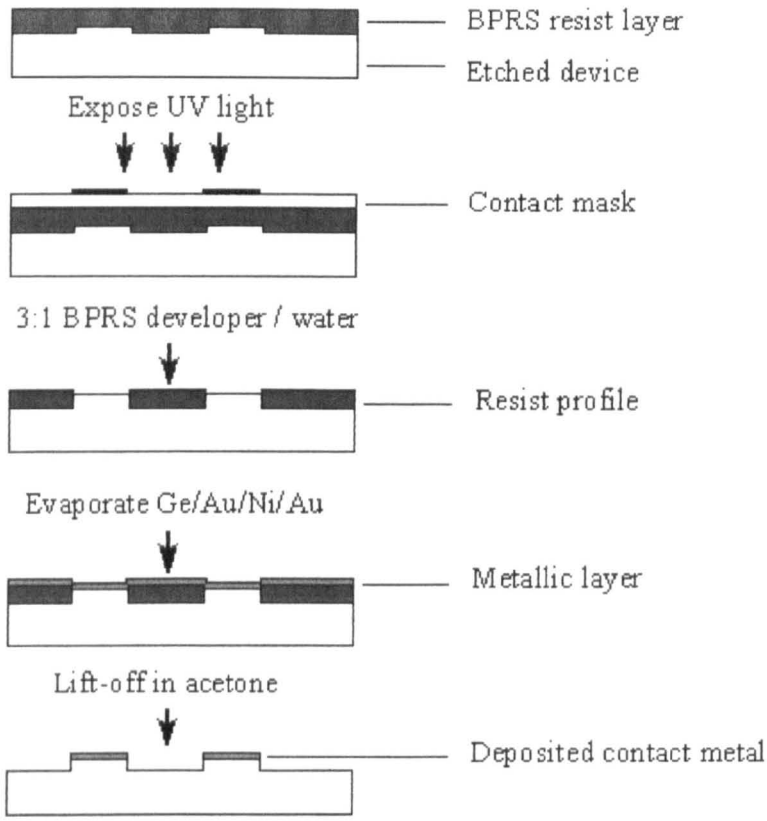

Figure 4.10: Photolithographic process for depositing metallic contacts

nitrogen gas. The chamber temperature was then raised to 450°C over a period of 3 minutes, using a linearly ramped temperature gradient. Upon reaching the peak temperature, the heating element was shut off, with the samples being allowed to cool.

Bolometers must then be evaporated onto the other face of the crystal. To prepare the sample, the surface must first be polished.

4.4.5 Polishing

The wafer substrates have a rough underside, due to the diffusion of indium into the GaAs during the MBE growth process. Therefore they must be polished before the evaporation of bolometers or a metal film on the reverse face of the substrate can be performed.

A two-stage polishing process is carried out using a Multipol rotating-lap polisher. Up to four GaAs samples are mounted onto a metal polishing chuck with melted wax, taking care to ensure that air does not become trapped underneath the samples. The levelling of the samples is further ensured with an autocollimator.

The first polishing stage uses a grooved solder lap, with 6μm diamond paste used as the abrasive agent. Hyprez, a proprietary lubricant, is sprayed onto the lap as it rotates. The polishing is allowed to continue until all the main imperfections and scratches have been removed from the surface, leaving a flat, but dull, finish. Depending on the severity of the indium deposits on the surface of the wafer, this process may take anything from five to twenty minutes.

The second stage of the polishing process uses a cloth lap, with a combined chemical-mechanical action abrasive agent, INSEC FP (Fujimi Abrasives Supply Ltd, Japan), resulting in a mirror-finish to the sample surfaces, achieved in no more than two to three of minutes of polishing. The INSEC agent consists of a powdered suspension of SiO_2 particles in a solution

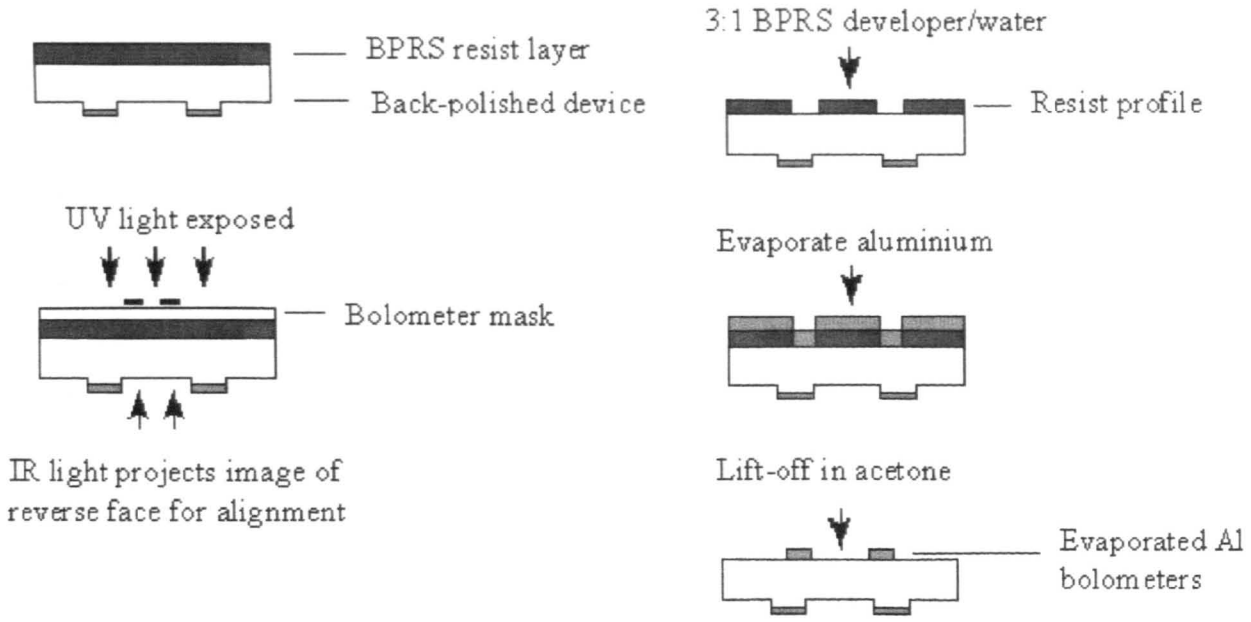

Figure 4.11: Photolithographic process for alignment and depositing of aluminium bolometers

of aqueous sodium sulphate with a chlorous oxidising agent. To form a solution used in the polishing process, this powder is dissolved in distilled water in the ratio 1.15g : 25ml, with further distilled water being used to lubricate the lap as it rotates. Washing the samples with an excess of water immediately on the conclusion of the polishing process is also essential to ensure that further etching is prevented.

Between the two polishing stages, the polishing jig should be cleaned in an ultrasonic bath briefly to prevent diamond-paste damage to the cloth lap used in the INSEC polish.

4.4.6 IR alignment and evaporation of bolometers

To align the bolometer mask with the 2DEG etch and contacts, infra-red alignment is used to illuminate the underside of the sample, as shown in *Figure 4.11*. The mask can then be positioned so that one bolometer channel is positioned directly opposite the 2DEG channel.

By evaporating of the aluminium bolometers at at a higher pressure (10^{-5} Torr) than for the contacts, the superconducting transition temperature of the bolometer is pushed to a higher temperature, ~1.8-2.0K. By selecting a higher transition temperature, the cryostat temperature may be more easily regulated.

4.5 The Phonon Emission Experiment

In the experiments performed for this work, the heat pulse technique was used to observe the emission from a range of *n*-type single quantum well devices, having well widths in the range 3nm to 15nm.

The well parameters are shown in *Table 4.2* below. The 2D electron densities N_s and mobilities μ were calculated from magneto-transport (Shubnikov-de Haas) characteristics. The well widths w could be verified

using cross-sectional transmission electron microscopy (XTEM) measurements.

Wafer No.	*NU665S*	*NU590S*	*NU535S*	*NU667S*	*NU666S*
Well width w (nm)	3.0	5.1	6.8	12.0	15.0
2D electron areal density N_s (10^{15} m^{-2})	1.7	1.7	2.0	3.7	3.6
4.2K mobility μ (m^2 V^{-1} s^{-1})	4.4	6.2	15	48	55

Table 4.2 : Quantum well parameters

Experimental samples were fabricated from each of the wafers, following the techniques described above. A 2DEG active region of dimensions 120μm x 50μm was etched with large, 1mm^2 *n*-type ohmic contacts used to apply heat pulses to the carriers. The contacts were well separated from the active area, in order to reduce the influence of heating effects on the detected signal.

The reverse face of the GaAs substrate was polished and an array of three 100μm x 10μm superconducting aluminium bolometers deposited upon it by vacuum evaporation. One bolometer was positioned directly opposite the device using infrared front-to-back alignment. The other bolometers were positioned at distances of 100nm and 200nm along the [100] direction, corresponding to angles of 14° and 27° to the normal of the 2DEG device.

Each sample was cooled to the superconducting transition temperature of the bolometers, ~1.8K. Electrical pulses of duration ~ 10–20ns were applied to the device contacts to heat the electrons in the 2DEG. Input voltages from 0.01V to 5V were used, with the power dissipated being determined from measurements of the input and reflected pulse heights on the transmission line between the pulse generator and the device:

$$P_{2DEG} = \frac{V_i^2 - V_r^2}{Z_0}$$

where Z_0 is the impedance of the transmission cable, 50Ω.

Similarly the instantaneous 2DEG device resistance R_{2DEG} in response to an input pulse V_i can be obtained by:

$$R_{2DEG} = Z_0\left(\frac{V_i + V_r}{V_i - V_r}\right)$$

By comparing R_{2DEG} with the steady state resistance versus temperature characteristic for the device, an estimate of the electron temperature T_e can be made.

The emitted phonons traverse the GaAs substrate at the speed of sound, v_s, falling on the bolometers, warming them slightly to cause an increase in bolometer resistance. With a constant bias current flowing in the bolometers, this change in resistance is converted to a voltage pulse that may in turn be captured using a high-speed digitiser and signal averager, resulting in a response such as *Figure 4.12*.

The LA and TA peaks are identified by their initial risetimes, calculated from the ballistic phonon transit time across the substrate. The observed peak widths are considerably greater than the duration of the heat pulse used to warm the 2D electrons: after the end of the pulse, the bolometer current decays slowly due to the RC time constant of the circuit.

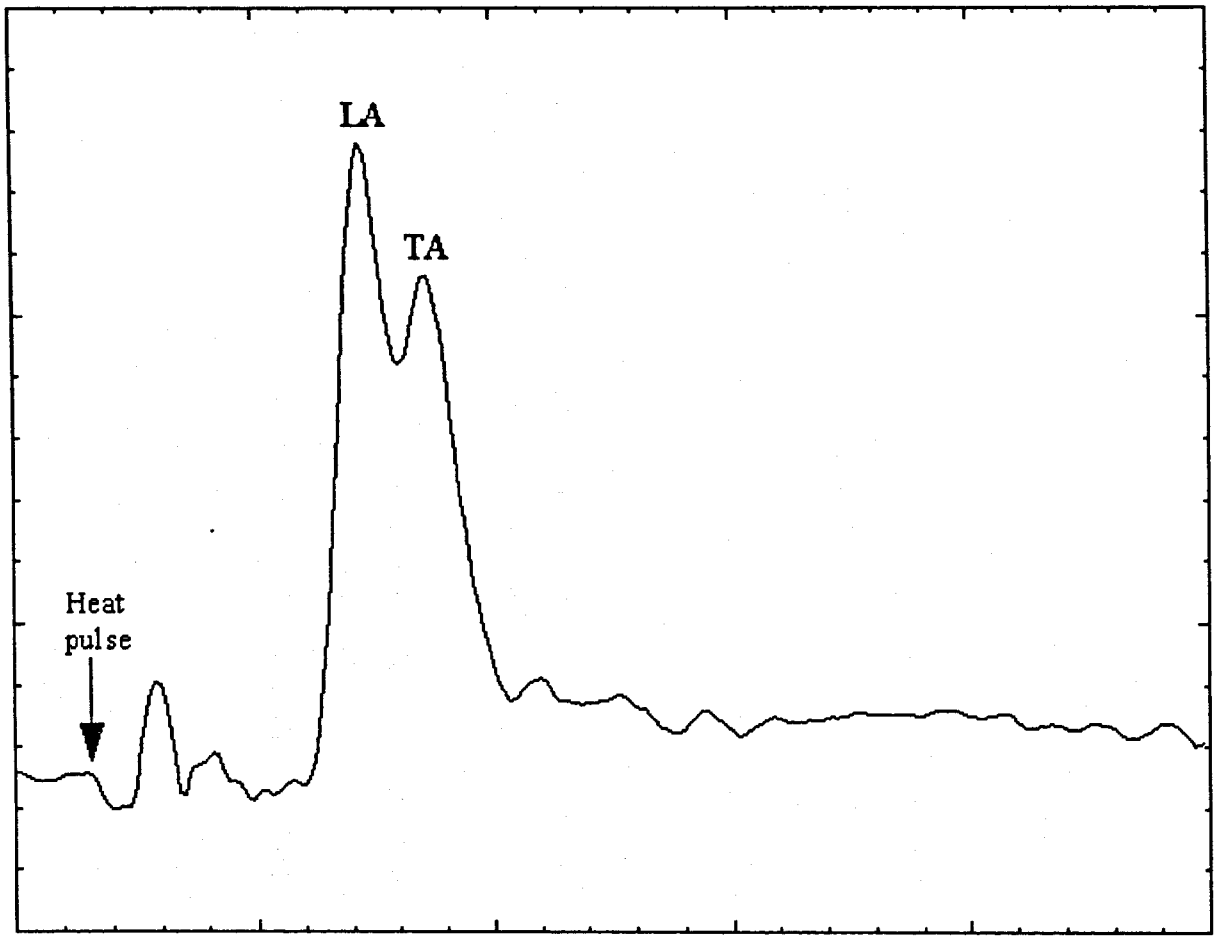

Figure 4.12 : Time-of-flight signal, showing LA and TA phonon mode peaks

4.5.1 Data post-processing with the POSTPROC program

To assist with post-processing the time-of-flight phonon traces, an experimental data analysis program, "POSTPROC" (*Figure 4.13*) was written. For a set of phonon traces saved in a single directory, corresponding to a sweep of the input signal power, the program allows the user to set time-gates corresponding to each phonon peak (ballistic LA, ballistic TA, and optic phonons), along with a "baseline" gate.

The time corresponding to the excitation pulse can be typically be identified in the traces by residues of electrostatic breakthrough that have not been perfectly cancelled by the trace subtraction technique, as shown in *Figure 4.12*. Identification of the times corresponding to the rise and peak of the LA and TA phonon signals was carried out manually with visual assistance from the POSTPROC program, starting from an initial estimate based upon an offset from the excitation pulse time, corresponding to the theoretically calculated ballistic phonon flight times across the GaAs substrate.

Graphs of the phonon signal as a function of input power, or the ratio of the relative modes, can be automatically generated. Routines for trace smoothing, phonon tail estimation and attenuation level (in dB) to input power (in pW/electron) conversion are included.

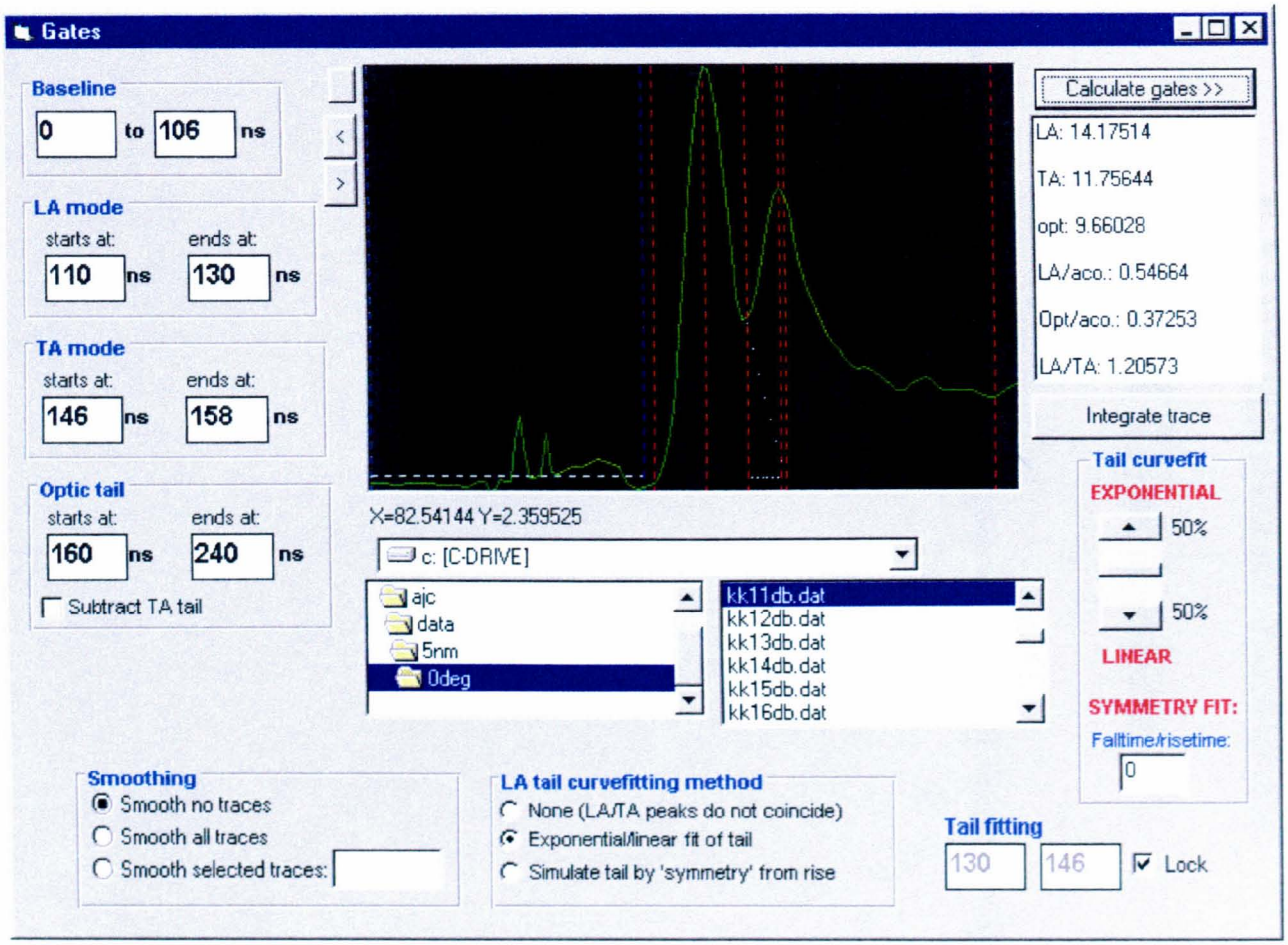

Figure 4.13 : Use of POSTPROC program to post-process phonon signals

Chapter 5
Experimental Results and Discussion

5 Experimental Results and Discussion

5.1 Introduction

Heat pulse experiments to measure acoustic phonon emission have provided vital information about carrier-phonon scattering and hot carrier energy relaxation in two-dimensional electron gases.

In these experiments the carriers in the 2DEG are heated above the crystal lattice temperature through the application of a short electrical pulse. The substrate crystal is of low defect density, and maintained at an equilibrium lattice temperature of ~1.5K. The emitted phonons propagate ballistically across the substrate crystal and are detected by bolometers on the substrate surface opposite the device. The difference between the ballistic times of flight of longitudinal and transverse acoustic phonons across a 380μm-thick GaAs wafer is about 40ns, and so by using electrical pulses shorter than this, the two modes may be temporally resolved. By placing bolometers at different positions on the detector surface, spatial resolution may also be achieved.

The use of heat pulses, therefore, allows information about the carrier-phonon coupling processes to be directly obtained. This is in contrast to the "averaged" nature of the results that are attained using other methods, for example, luminescence spectra or transport techniques.

Several groups (e.g. Chin *et al.*, 1984, Hawker *et al.*, 1992) have used the heat pulse technique to study the energy relaxation of hot two-dimensional electron gases in gallium arsenide heterojunctions. An apparently anomalous feature of their results was that, compared with the transverse acoustic mode, emission of the longitudinal acoustic mode is very weak. For temperatures in the range $5\text{K} < T_e < 50\text{K}$, the deformation potential (which varies linearly with the phonon wavevector q and energy $\hbar\omega$) should be expected to dominate

over the piezoelectric interaction (which varies as q^{-1}) as the main mechanism by which electrons couple to phonons.

This result is confirmed in an initial experiment carried out for the present work. A 2DEG GaAs/(AlGa)As heterojunction (NU1286) was excited with short (~ 20ns) heat pulses of varying power. *Figure 5.1* shows the time-of-flight phonon signal detected by a 100μm x 100μm superconducting aluminium bolometer positioned directly opposite a 120μm x 50μm etched 2DEG active channel, near to the surface of the 380μm thick semi-insulating GaAs substrate. The 2D areal density N_s for the 2DEG was 2.8 x $10^{15}m^{-2}$ .A sharp peak, having a risetime approximately 120ns after the input pulse, is observed, corresponding to the ballistic flight time of TA phonons across the substrate. There is no evidence of an LA response, which would be expected to have a rise-time of ~70ns after the input pulse. The long, diffuse tail that follows the TA peak results from the emission of longitudinal optic phonons, which rapidly decay into high frequency transverse modes.

These measurements are therefore fully consistent with the previous heat pulse studies of the phonon emission from 2DEG GaAs/(AlGa)As heterojunctions as noted above.

In bulk GaAs epilayers, LA mode emission is observed (Kent *et al.*, 1997), in spite of the preferential focusing of TA mode phonon energy towards the 2DEG normal, due to the predicted domination of deformation potential coupling. "Ideal" TA phonons, having their polarisation perpendicular to the phonon wavevector, are forbidden from coupling to the deformation potential. As the sample geometry is the same in both cases, with the bolometer directly opposite the device on a (100) substrate, this difference between the result for bulk GaAs and a 2DEG heterojunction cannot be attributed to

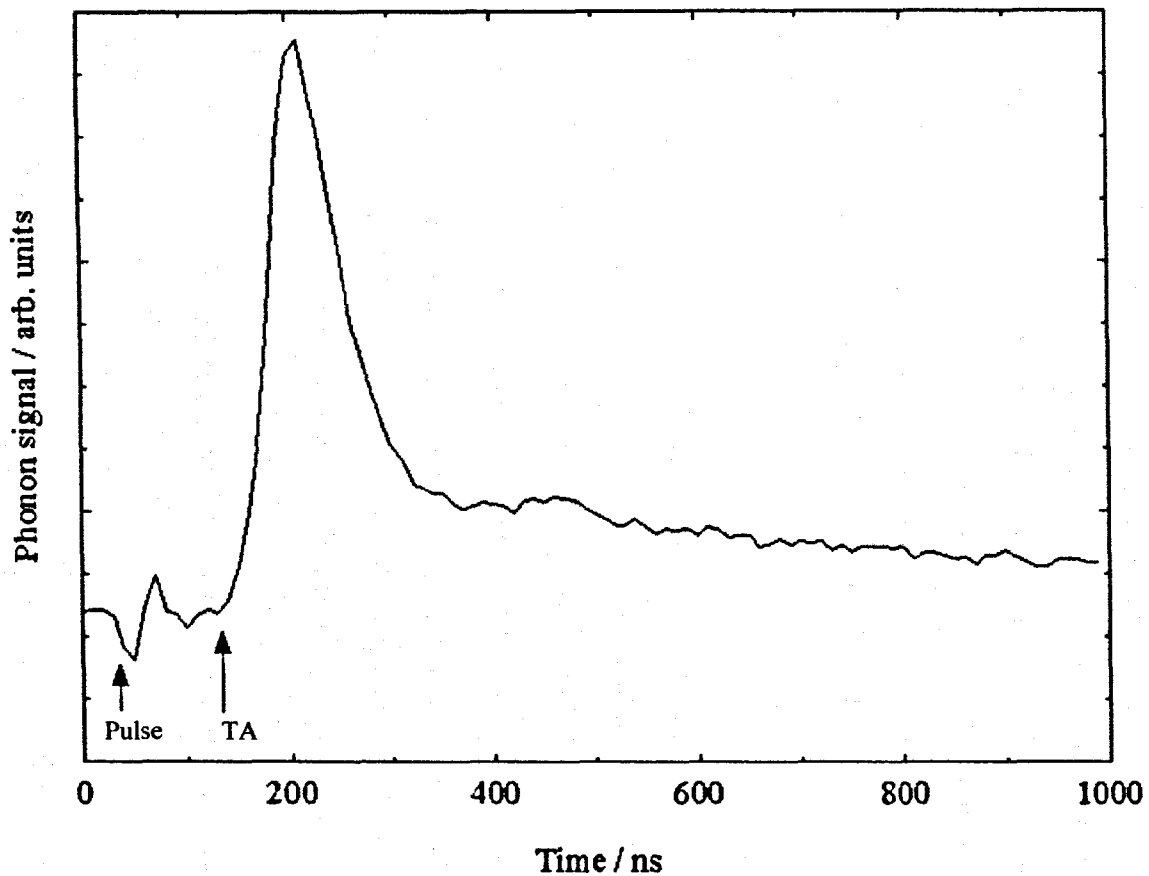

Figure 5.1: Time of flight signal showing phonon emission from a 2DEG heterojunction.
The digitiser is pre-triggered at t=0, the electrical breakthrough of the excitation pulse is indicated as well as the rise time of the TA phonon pulse.

phonon focusing effects alone, as suggested in some earlier studies (Hawker *et al.*, 1992). The absence of the LA mode in the case of the heterojunction must therefore be associated with the nature of the electron confinement in the 2DEG.

It would therefore appear that contrary to earlier theoretical predictions (Vass, 1987), the dominant coupling process for the electron-phonon interaction in a heterojunction for the temperature range 5K < T_e < 50K is the piezoelectric interaction. Theoretical calculations of the electron-phonon coupling matrix elements (*Figure 3.3*) show a crossover between piezoelectric interaction and deformation potential coupling at a phonon wavevector q_c = 1.8 x 10^8 m^{-1}. Above this crossover, electrons are expected to relax their energy predominantly through the emission of deformation-potential coupled LA phonons.

A reason why this behaviour is not observed can be offered by considering energy and momentum conservation requirements, which impose a restriction on the component of the emitted phonon wavevector in the direction normal to the 2DEG plane. The form factor $|F(q_z)|^2$ accounts for momentum conservation in the *z*-direction, perpendicular to the 2DEG, when a phonon is emitted. If the momentum cutoff occurs at a value lower than the matrix element crossover q_c between deformation potential and piezoelectric coupling, suppression of the DP coupling occurs, resulting in the absence of LA modes, which couple far more strongly to the deformation potential than to the piezoelectric interaction.

For a heterojunction, assuming a triangular potential well confinement, $|F(q_z)|^2 = (1 + q_z{}^2 a_0{}^3)^{-3}$ where q_z is the component of the phonon wavevector along the normal to the 2DEG and a_0 is the Fang-Howard parameter, related to the "thickness" of the 2DEG. Typically a_0 = 4nm for a GaAs heterojunction, which means that the electron-phonon interaction is effectively cut off at a phonon wavevector of $q \sim 1 \times 10^8 m^{-1}$ for LA modes.

Comparing this $1/a_0$ cut-off to the wavevector q_c at which the matrix elements for the deformation potential and piezoelectric interaction are equal, it can be seen that the deformation potential is not able to dominate the coupling, due to transitions with high wavevector q being forbidden. In such systems, PZ coupling will be dominant, favouring the emission of TA phonons at small angles normal to the 2DEG.

Strickland (1994, 1996) carried out heat pulse studies of a 2D hole-gas (2DHG) heterojunction grown on a (311A) GaAs substrate. The sample was similar in carrier density and mobility to the 2DEGs used in the experiments discussed above. An enhanced LA mode was observed compared to the 2DEG result, which was attributed to the stronger carrier confinement in 2DHG systems (a_0 = 2nm) compared with 2DEG heterojunctions (a_0 = 4nm). Further studies on a (100) grown 2DHG device also showed an LA response, of smaller intensity to the signal observed from the (311A) 2DHG, owing to the preferential focusing of TA modes over LA modes in the (100) crystal direction.

An alternative method for varying the carrier confinement was employed by Hawker *et al.* (1995), who used heat-pulse experiments to measure the energy loss rate of GaAs/(AlGa)As *n*-type single quantum well structures, having well widths w = 5nm and w = 10nm. The square potential well results in stronger carrier confinement than for an equivalent thickness heterojunction. With a bolometer positioned at 50° to the device normal, longitudinal acoustic mode phonon emission was observed, with a stronger LA response for the narrower well. It should be noted, however, that the choice of bolometer angles coincides with the focusing direction for LA phonons in (100) GaAs. Additionally the samples used had a high 2D carrier density, ($N_s \sim 1.6\text{x}10^{16}\text{m}^{-2}$), which results in enhanced electron-phonon coupling and a weakening of the electron confinement dependence of emission.

5.2 Acoustic Phonon Emission from a 2DEG Quantum Well

An improvement on the approaches used by the Hawker and Strickland groups to vary the carrier confinement is made in the present work, by studying the acoustic phonon emission from a set of five *n*-type quantum wells of varying width: 3.0, 5.1, 6.8, 12.0 and 15.0nm.

The carrier density of the samples is lower than in the Hawker experiments, $N_s \sim 2\text{x}10^{15}\text{m}^{-2}$, corresponding to a Fermi wavevector $k_F = (2\pi N_s)^{1/2} = 1.1\text{x}10^{8}\,\text{m}^{-1}$, resulting in a predicted angular emission "cone" more closely directed towards the 2DEG normal. The angular dependence of emission is considered in more detail than in previous studies, using bolometers positioned at 0°, 14° and 27° to the device normal, each having an angular "capture" normal to the 2DEG of ~1.4°.

The emission experiment was carried out using the method described in the preceding chapter. Phonon time of flight traces were acquired for each quantum well for a wide range of heat pulse input powers, with the data so obtained being processed as described in *4.5.1* above.

The discussion of the acoustic emission data is divided into three main topics:

- The variation of emission with well width w for a constant input power per electron, P_e.
- The variation of emission with well width w for a constant electron temperature T_e.
- The variation of emission with power per electron P_e for a fixed well width w.

5.2.1 The LA to TA Ratio

In order to experimentally observe the lifting of the suppresion of deformation potential coupling as the $1/a_0$ cutoff is relaxed, it is necessary to formulate a means of estimating the DP coupling strength in terms of experimentally measurable quantities.

It can be shown that the ratio of longitudinal to transverse acoustic phonon signal height is a practical experimental indicator of the ratio of DP to PZ-coupled emission. As discussed in Chapter 3 (*Figure 3.16*), the predicted PZ-coupled LA signal at the detectors is negligible in the chosen experimental arrangement. The LA response can therefore be used as a direct measure of the DP emission strength. *Figure 5.2* shows theoretically calculated ratios of LA to TA mode phonon emission as a function of the magnitude of the phonon wavevector, q. The parameters used for the calculation were: quantum well width w = 6.8nm, electron temperature T_e = 10K, lattice temperature T_l = 1.5K, carrier density $N_s = 2.0 \times 10^{15}\text{m}^{-2}$. For comparison, the ratio of total DP-coupled emission to PZ-coupled emission is also plotted. It is observed from the shape of the two curves that the LA:(LA+TA) ratio may be used as a practical means of measuring of the DP coupling strength experimentally.

For small wavevectors q, PZ-coupled emission is dominant, however the LA to (LA+TA) ratio for the total emission into all possible angles does not fall to zero, due to PZ-coupled LA emission. In Chapter 3 (*Figure 3.16*), it was shown that PZ-coupled LA emission should be negligible at the positions corresponding to the detectors used in the experiment. Therefore, if deformation potential coupling is suppressed in the experimental system, the measured LA to (LA+TA) ratio at the bolometers is expected to fall to a value close to zero, as in the case of the DP to (DP+PZ) ratio.

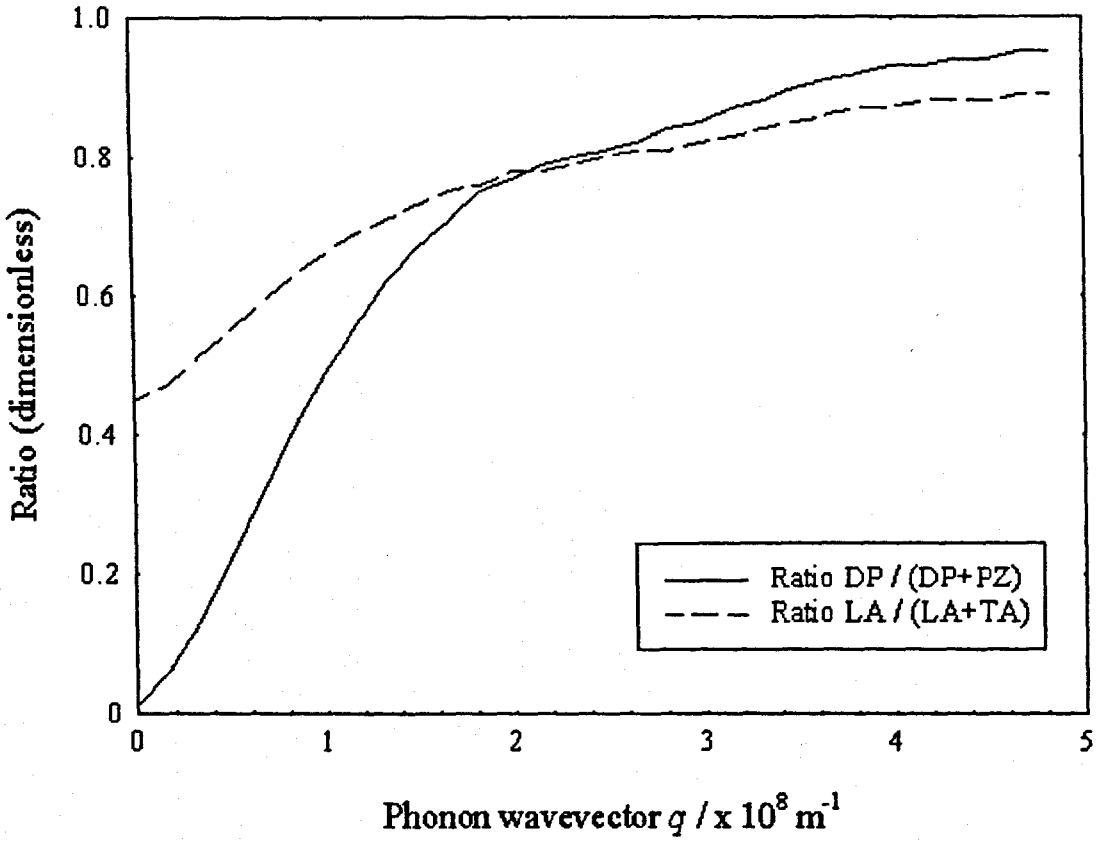

Figure 5.2: Theoretically calculated ratios of LA / (LA+TA) and DP / (DP+PZ) phonon emission from a 6.8nm quantum well.

5.2.2 *Variation of emission with well width at constant power*

Figure 5.3 shows the time-of-flight phonon emission response from the 6.8nm and 15nm quantum wells, for an fixed heat pulse power P_e of 1pW per electron. The detecting bolometer was positioned directly opposite the active 2DEG device. The two sharp peaks observed correspond to the characteristic ballistic flight times of LA phonons (speed $v_s = 5160$ ms^{-1}) and TA phonons ($v_s = 3050$ ms^{-1}) across the 380μm GaAs substrate. LA mode emission can be observed in addition to the TA emission at both well widths. For the 15nm quantum well, this LA response takes the form of a small "shoulder" before the rise of the TA peak, whereas for the 6.8nm well, the longitudinal response is of the same order of magnitude as the contribution from TA phonons.

As for the heterojunction in the preliminary experiment, a broad, dispersive optic phonon tail is observed for higher input powers. The oscillations in this tail are attributed to persistent amplifier ringing that has not been fully cancelled out by the trace subtraction method described in the previous chapter.

The suppression of the DP-coupled LA mode is therefore seen to be lifted for the quantum well samples, due to the stronger carrier confinement compared to heterojunction devices. Additionally, the proportion of LA emission in the total emitted phonon energy is seen to be much larger for the narrow well.

The experimentally measured LA to (LA+TA) emission ratio is shown for all the wells in *Figure 5.4*, along with the theoretically calculated ratio for each well, for an input power of 1pW per electron.

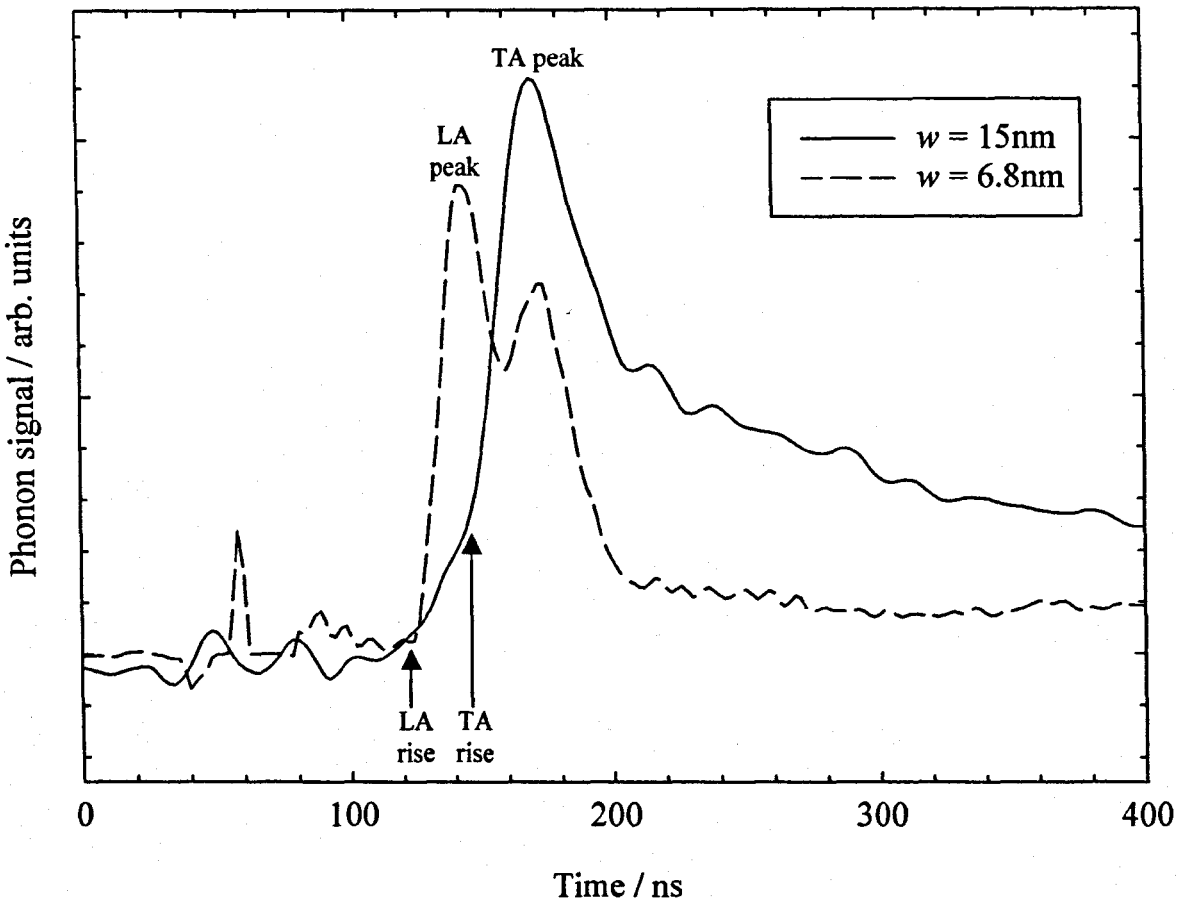

Figure 5.3 : Acoustic phonon emission heat pulse signals from 6.8nm and 15nm quantum wells at an excitation of 1pW/carrier

The margin of error on the experimental measurement is calculated by allowing for a constant measurement inaccuracy of ± 5% (with respect to the largest peak in each case) in evaluating the longitudinal and transverse phonon peak heights. For higher values of the LA to (LA+TA) ratio, where the transverse peak height is small compared to the longitudinal peak, the relative uncertainty in the measurement is therefore increased. An uncertainty has also been applied to the theoretically calculated emission ratio, as only an extremely small fraction of the total number of generated 'virtual phonons' hit the detector region. To reduce this uncertainty would require much longer run-times than were possible in this work.

It is clearly seen that as the well width is narrowed, the LA mode starts to dominate over the TA mode in the acoustic emission response. The theoretical calculation predicts that the LA mode should continue to strengthen as a ratio of the total acoustic emission as the well width is progressively narrowed further, saturating only at very narrow well widths where the $1/a_0$ cutoff occurs at a much higher wavevector q_c than that corresponding to the peak frequency in a Planckian distribution at T_e.

The increasing strength of the LA response with narrowing well width can be attributed to increased phase space for the deformation-potential coupled interaction, due to the lessened effect of the $(1/a_0)$ cutoff as the well width w, and hence a_0, is shortened.

It is seen that the measured ratio LA/(LA+TA) decreases slightly for the 3nm and 5.1nm devices. Two explanations may be put forward for this exception to the general trend of increasing LA intensity with narrower well widths.

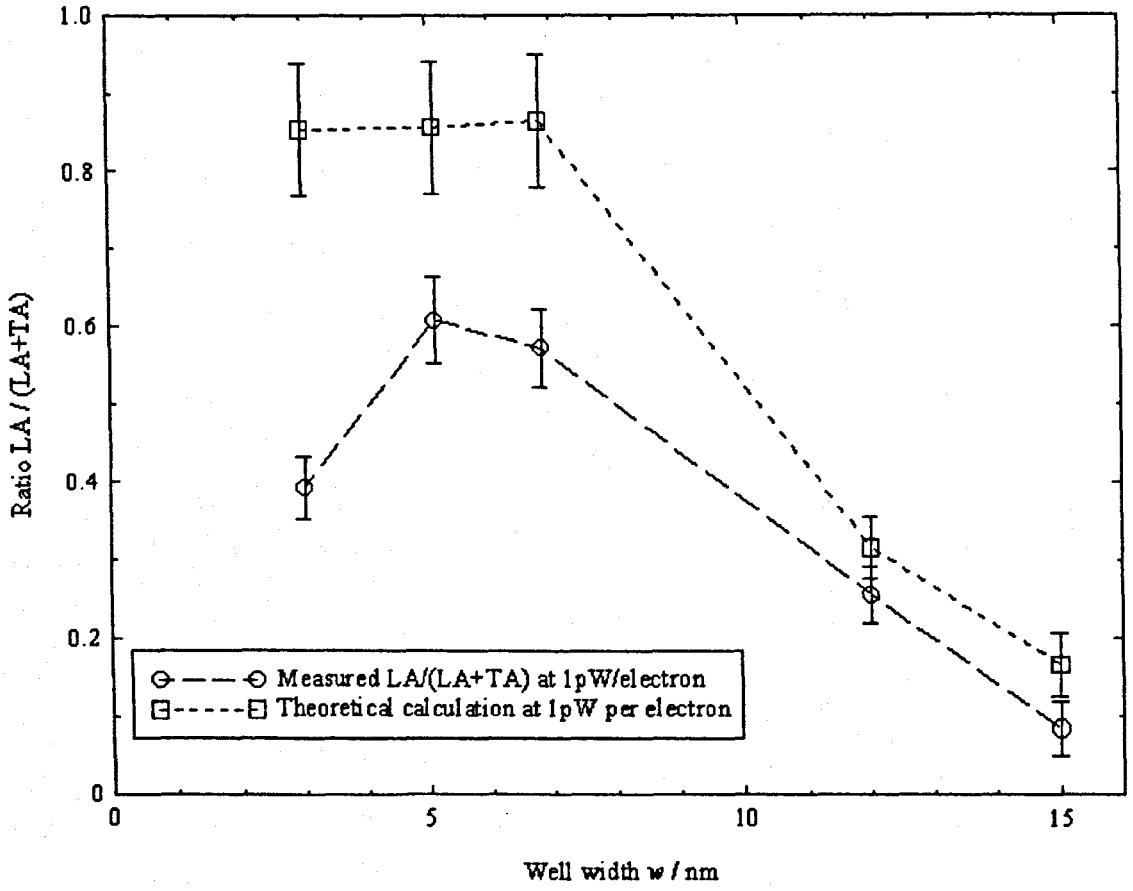

Figure 5.4: Experimentally measured LA/(LA+TA) ratio for detected phonon emission at P_e = 1pW/electron, compared to theoretical calculated values.

Consider first the bound-state form factor $|F(q_z)|^2$ from which the $1/a_0$ cutoff arises: for w = 6nm, calculation shows that the form factor falls to a value of 0.5 for a perpendicular phonon wavevector component of $8\text{x}10^8\text{m}^{-1}$, corresponding to an LA phonon frequency of 700GHz. For well widths below ~6nm, it can therefore be concluded that further narrowing of the well does not increase the LA response further, as the $1/a_0$ cutoff occurs at a frequency much higher than ballistic LA phonon frequencies.

Due to the lower speed of TA modes, the transverse phonon frequency corresponding to this same wavevector is 370GHz. Therefore, for $|F(q_z)|^2$ to fall to a value of 0.5 for a TA phonon frequency of 700GHz, the well width must be further reduced, to 3nm. Therefore, as the well width is narrowed from 6nm to 3nm, the TA phonon response is expected to strengthen further due to the lessening $1/a_0$ cutoff, whereas the LA response is already independent of the cutoff. This results in a small dip in the LA/(LA+TA) ratio at well widths in the 3nm < w < 6nm range, with the LA proportion finally settling to a constant value at narrower widths.

For the case of ballistic acoustic phonons, then, it appears that the effect of the $1/a_0$ cutoff is negated completely once a critical well width is reached. The ratio of LA modes to TA modes below this critical width is, therefore, determined solely by the electron-phonon coupling matrix elements and the phonon focusing factor in the propagation direction.

A second explanation for the dip in the LA/(LA + TA) ratio at low well widths can be offered, in terms of the non-infinite confining potential in a "real" 2DEG quantum well. (Zheng *et al.*, 1997; section *3.5.3* of this thesis) Due to penetration of the electron wavefunction into the GaAs/(AlGa)As barrier, the effective z-direction extent of the 2DEG is larger than the well width, w, i.e. the electron confinement is weakened. This physical limitation

acts to suppress the theoretically predicted increase in the emission into large-wavevector DP-coupled LA modes as the well width is further narrowed.

5.2.3 Variation of emission with power for fixed well width

Figure 5.5 shows the acoustic phonon emission response from the 6.8nm quantum well at three values of the excitation power P_e, measured at the 0° bolometer. Significant emission is observed in both the LA and TA phonon modes. *Figure 5.6* shows the LA and TA pulse heights, plotted on a logarithmic scale as a function of the heat pulse power. In *Figure 5.7*, the corresponding LA/(LA+TA) ratio is shown, with approximate measurement uncertainties in the three main regions of the graph indicated.

For pulse powers $P_{2DEG} > 20$pW per electron, the ratio is fairly constant, due to the dominance of deformation potential coupled emission into both LA and TA modes. For very low pulse powers, the ratio appears to rise towards 1, however this appears to be due to the increased numerical uncertainty in calculating the ratio of two small signals.

The region of most interest occurs between heat pulse powers of 0.5pW $< P_{2DEG} <$10pW per electron. In this power range, the LA/(LA+TA) ratio rises from 0.48 to about 0.6, suggesting a change in the nature of the electron-phonon coupling in the 2DEG.

It is interesting to compare the power dependence of the acoustic phonon emission from the 6.8nm quantum well with the narrower and wider wells used in the experiment.

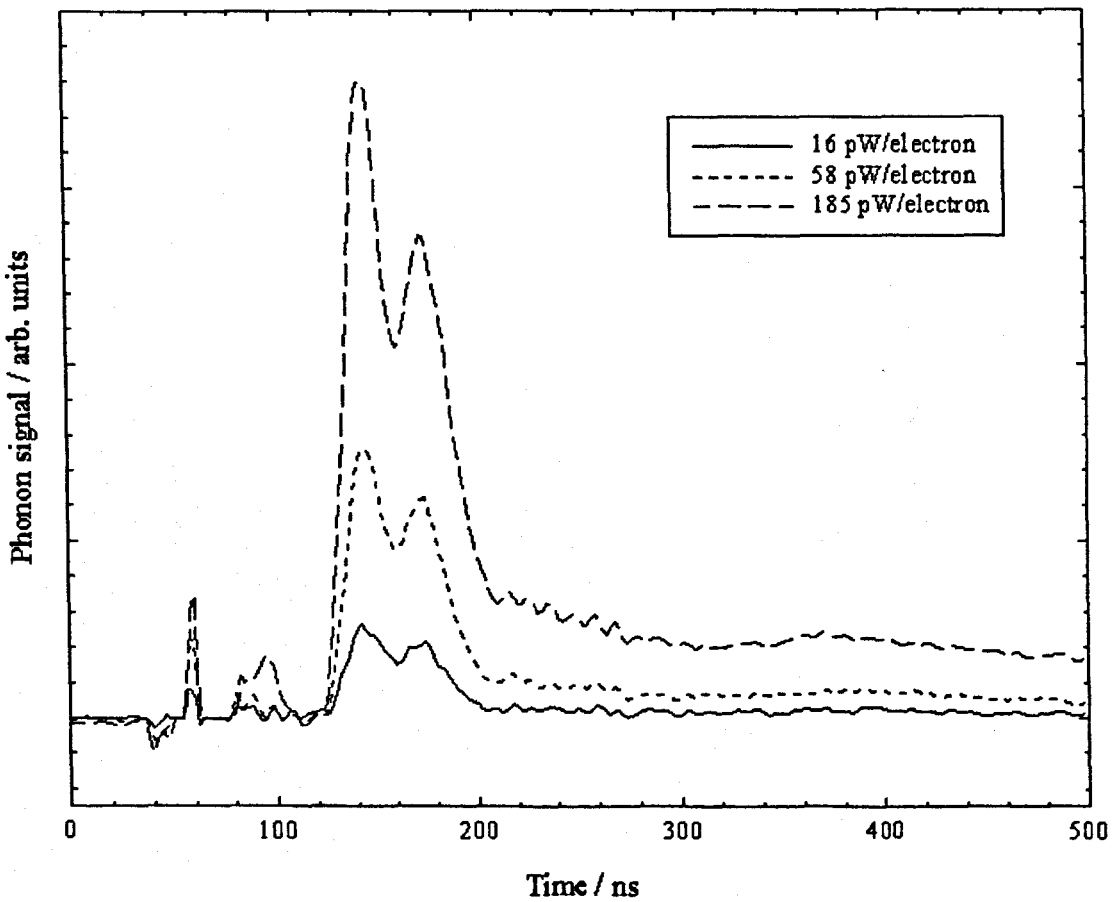

Figure 5.5 : Emission signal from 6.8nm quantum well, detected by 0° bolometer.

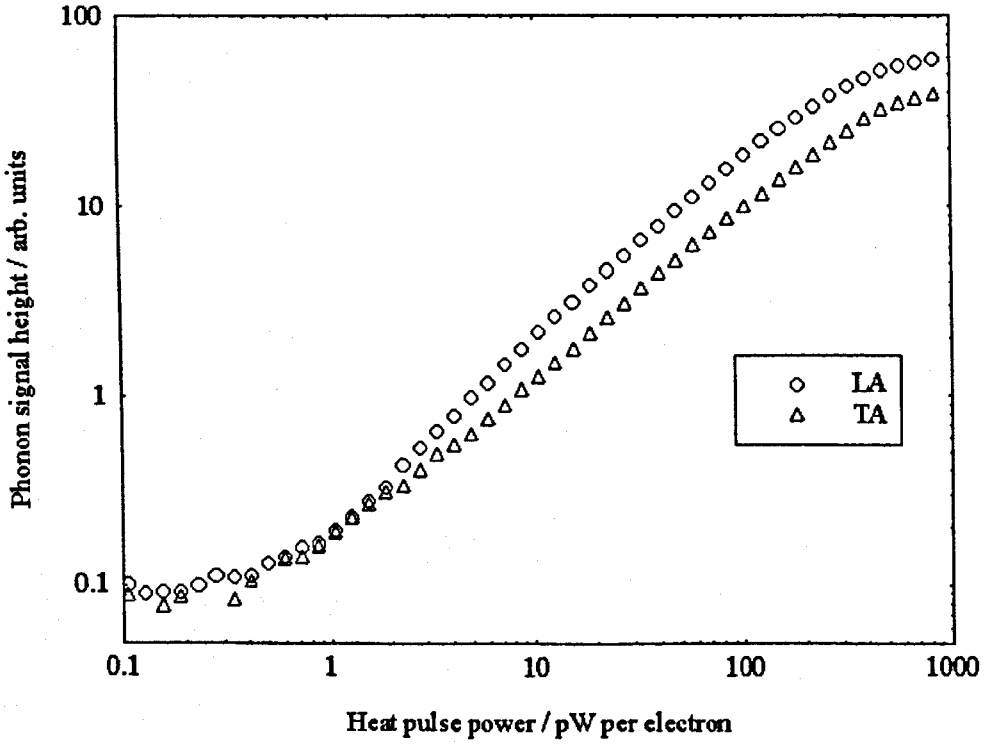

Figure 5.6: LA and TA signal heights for 6.8nm QW as function of heat pulse power

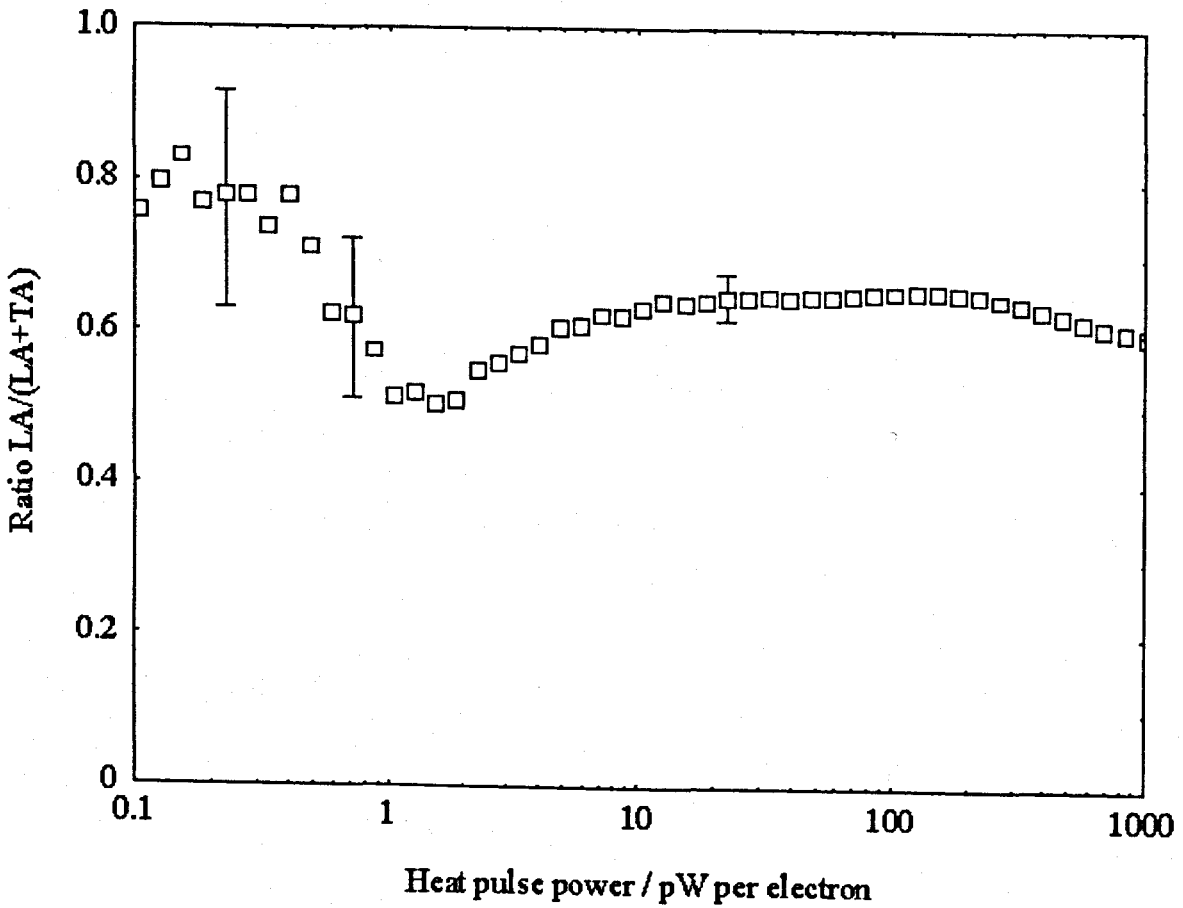

Figure 5.7: LA/(LA+TA) ratio for 6.8nm QW as function of heat pulse power

Figure 5.8 shows the power-dependence of the LA/(LA+TA) emission ratio for the 5.1nm quantum well, again at the opposite bolometer, while *Figure 5.9* shows the power dependence of the 12nm quantum well. Unlike the 6.8nm well, which has a fairly constant LA/(LA+TA) ratio for a wide range of input heat pulse powers, these devices show a trend of increasing or decreasing LA emission over the full range of input powers.

For narrow quantum wells, the LA proportion of emission is shown to increase with increasing power. Here the electron confinement is strong, so that the effect of the $1/a_0$ cutoff is weak over much of the experimental temperature range. For a 5.1nm quantum well, the bound-state form factor $|F(q_z)|^2$ falls to a value of 0.5 for a perpendicular phonon wavevector component $q_c \sim 5.3 \times 10^8 m^{-1}$, which corresponds to an LA phonon frequency of ~450GHz. *Figure 5.10* shows the theoretically calculated DP-coupled LA phonon emission from the 5.1nm quantum well as a function of phonon wavevector q, for a range of electron temperatures T_e.

It can be seen that even at T_e = 50K, electrons couple to a broad range of phonon wavevectors, with little evidence of a $1/a_0$ cutoff. If the $1/a_0$ cutoff is neglected, then DP-coupled emission should increase linearly with q, therefore in this case the observed increase in LA emission with increased power is fully explained by both the full theoretical model and the earlier approaches (e.g. Vass, 1987) that neglected to fully consider the 2D effective thickness.

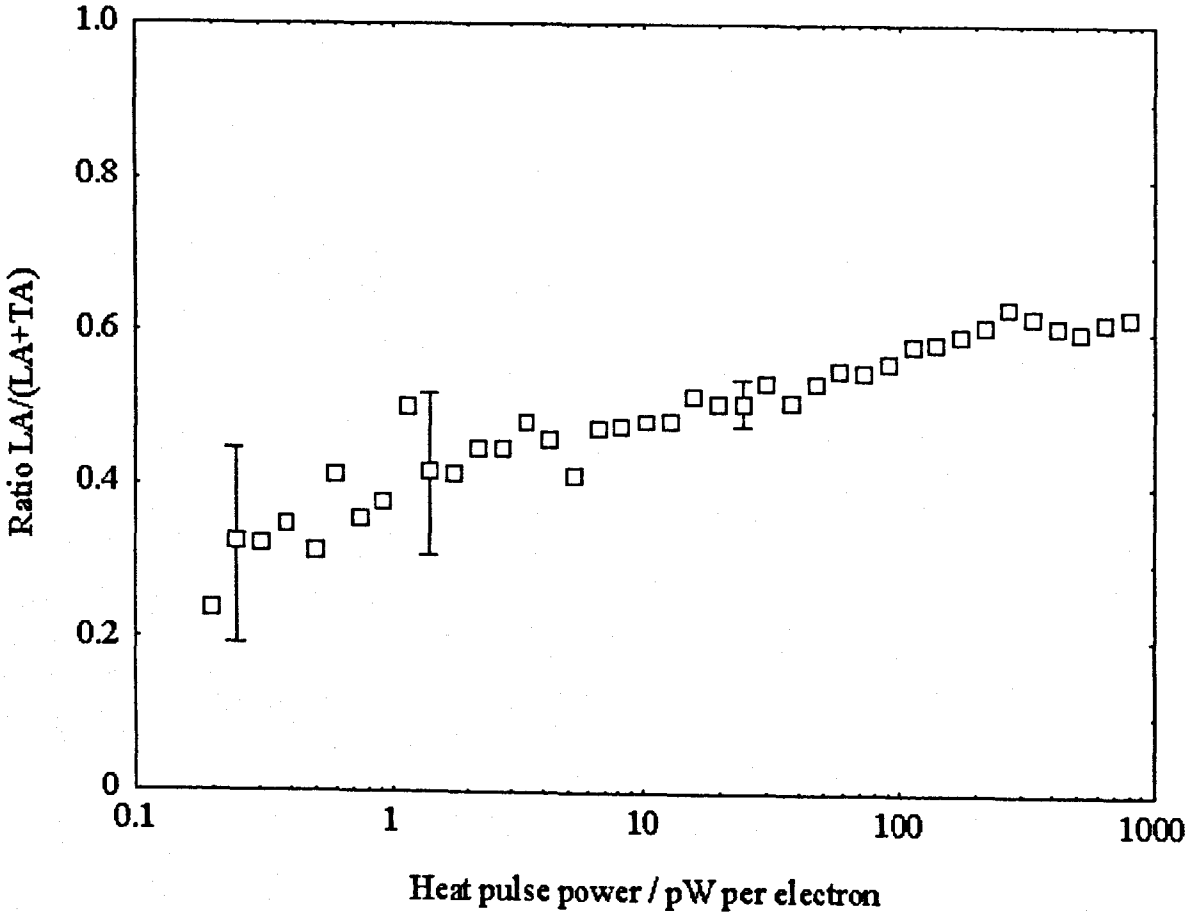

Figure 5.8: LA/(LA+TA) ratio for 5.1nm QW as function of heat pulse power

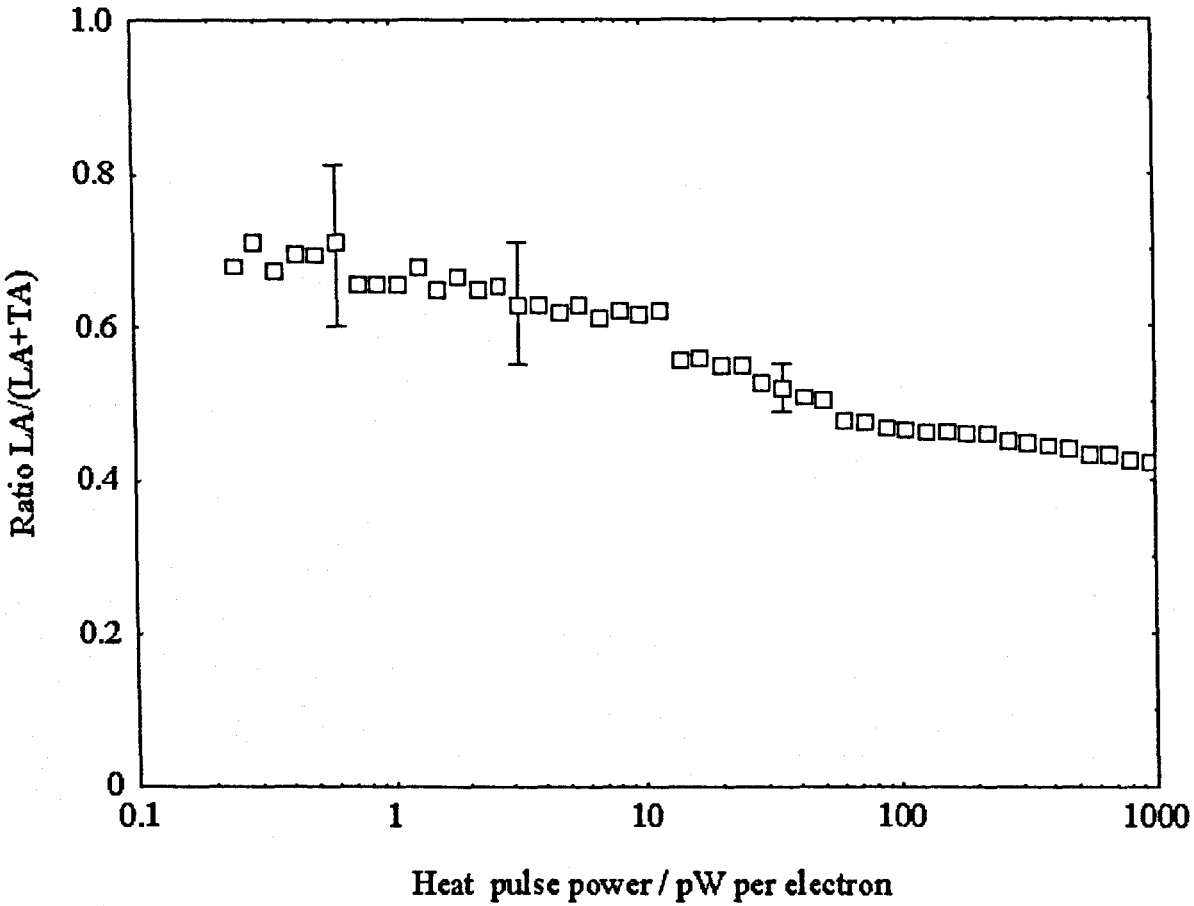

Figure 5.9: LA/(LA+TA) ratio for 12nm QW as function of heat pulse power

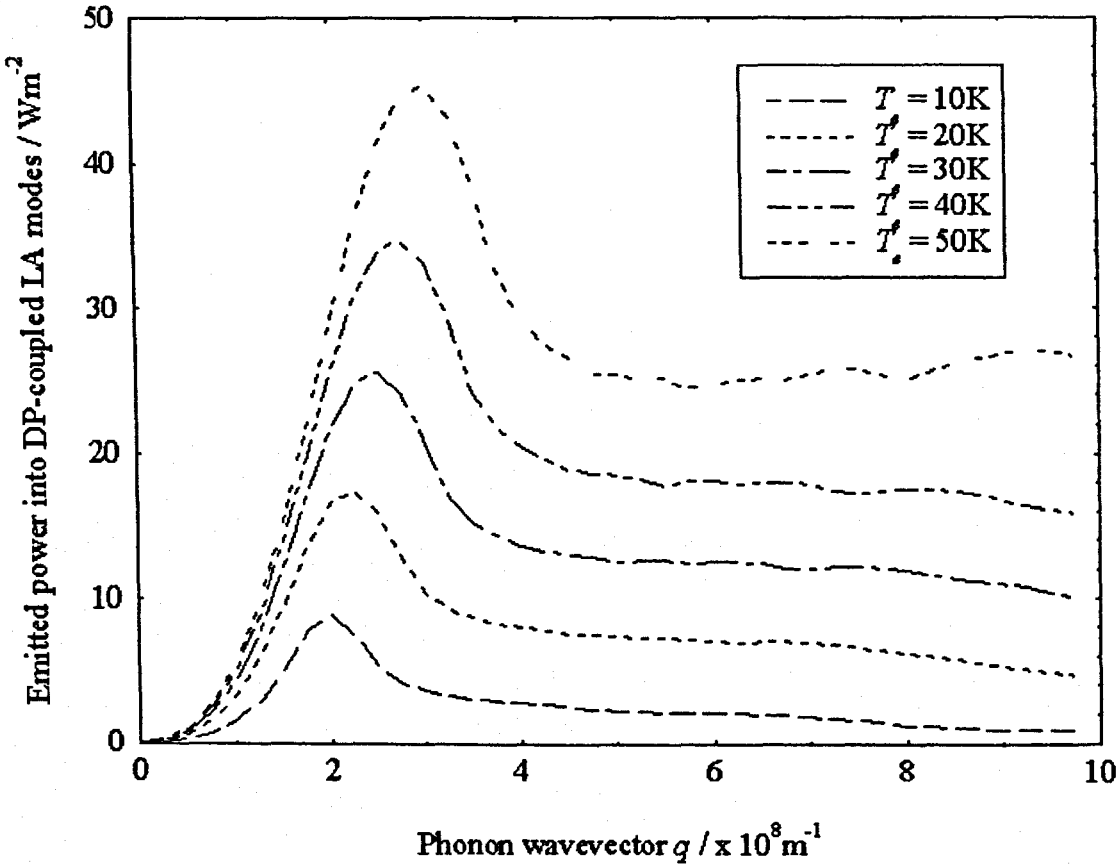

Figure 5.10: q-dependence of DP-coupled LA emission by 5.1nm QW 2DEG

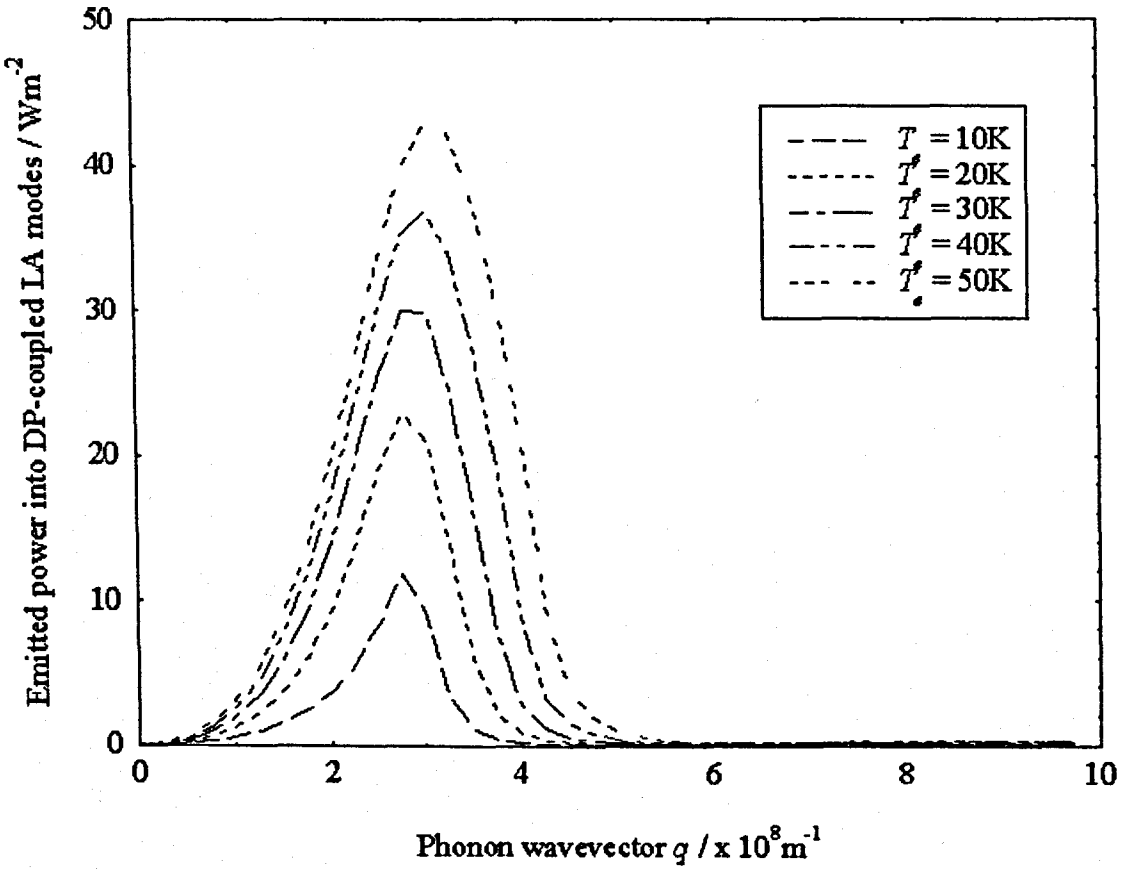

Figure 5.11: q-dependence of DP-coupled LA emission by 5.1nm QW 2DEG

Conversely, for wide quantum wells, a decrease in LA emission is observed as the power is increased. In these wells, electrons are rather more weakly confined, as in the case of a heterojunction. The $1/a_0$ cutoff therefore has a much stronger influence on the electron-phonon coupling in such systems. *Figure 5.11* shows the theoretically calculated q-dependence of the DP-coupled LA phonon emission from the 12nm quantum well, for a range of temperatures between 10K and 50K. The $1/a_0$ cutoff almost completely suppresses any coupling of electrons to phonons having wavevectors q in excess of $5\text{x}10^8\text{m}^{-1}$. At lower temperatures, however, the wavevector peak occurs at a lower value, with a resultant decrease in the proportion of possible electron-phonon couplings that are forbidden by the $1/a_0$ cutoff. The observed experimental increase in LA (and hence DP) emission intensity with decreasing power is therefore justified by theoretical considerations.

5.2.4 Variation of emission with well width at constant temperature

For several reasons, it is also of interest to study the acoustic phonon emission from the quantum well samples at constant electron temperature, in addition to the constant power results already presented. From pulse reflection measurements used to calculate the power dissipated in each quantum well device, it is found that the actual fraction of the input power absorbed by the 2DEG, and consequently the electron temperature that arises from a fixed input power, varies considerably as a function of the well width. Additionally, the crossover from acoustic to optic-dominant phonon emission occurs at a constant thermal energy (and so temperature), and the electron temperature is also a primary variable in the theoretical model of the electron-phonon system.

Figure 5.12 shows the ratio LA/(LA+TA) calculated at the opposite bolometer for each quantum well at a constant electron temperature of $T_e \sim$ 50K, along with the theoretically predicted ratios. Again, strong LA emission is observed, even in the wider wells, due to the less severe form factor cutoff for quantum well devices compared to heterojunctions.

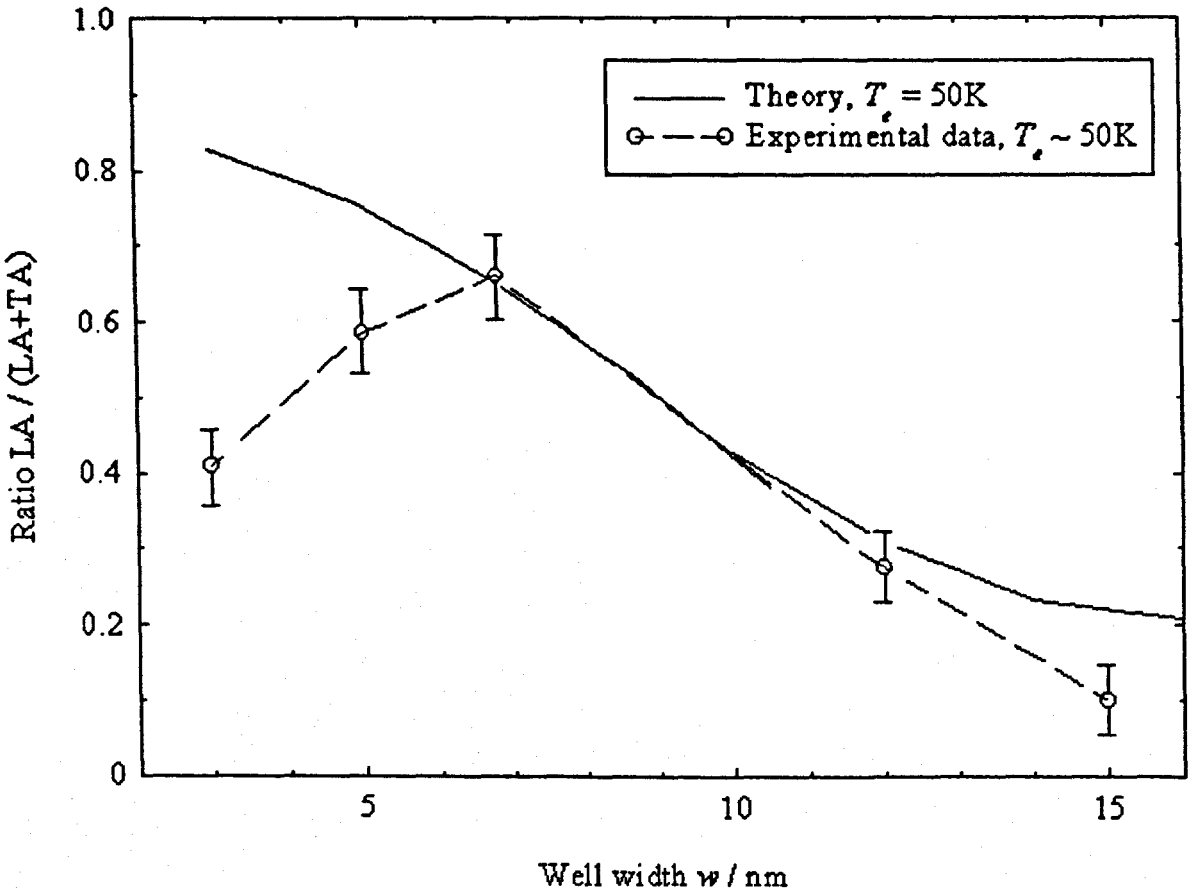

Figure 5.12: Experimentally measured LA/(LA+TA) ratio for phonon emission at T_e = 50K, compared to theoretical calculation.

Comparing the 12nm quantum well with a typical (a_0=4nm) heterojunction, the electron-phonon interaction is effectively cut off for the heterojunction at a wavevector below the crossover of the DP and PZ coupling matrix elements at $q_c \sim 1.8 \times 10^8$ m^{-1}, whereas for the 12nm quantum well significant DP coupling to LA modes is still possible. It is expected that this extra channel for acoustic phonon emission in quantum wells would result in more efficient energy relaxation by warm carriers. This should also increase the power level at which the crossover from acoustic to optic phonon emission that takes place at $T_e \sim$ 50K will occur, as will be discussed in *5.3* below.

Figure 5.13 shows theoretically calculated images of the predicted emission spectra for each quantum well at three carrier temperatures, T_e = 5K, 20K, and 50K. The images represent a 600μm x 600μm area on the detector plane.

Two main features are to be seen in the images: a dominant ring at ~30° corresponding to DP-coupled LA emission, and a pair of horizontal bars above and below the position of the 2DEG active area. These structures are indicative of DP-coupled slow transverse phonon emission. At low temperatures (T_e=5K) only, regions of the intensity corresponding to the diagonal-cross FT structure are observed, indicative of PZ-coupled fast-TA emission. At higher temperatures, these features are completely washed out by the dominant DP coupling. Furthermore, even at low temperatures, these structures do not correspond closely to bolometer positions used in the experiment.

This assertion that the TA phonons arriving at the experimental detectors (i.e. for angles $\vartheta \lesssim 30°$) are coupled almost exclusively by the deformation potential, is significant, as the conventional theory held that TA phonons were only coupled through the piezoelectric interaction; this further emphasises the importance of a "fully-inclusive" approach to the treatment of the theory of the electron-phonon interaction.

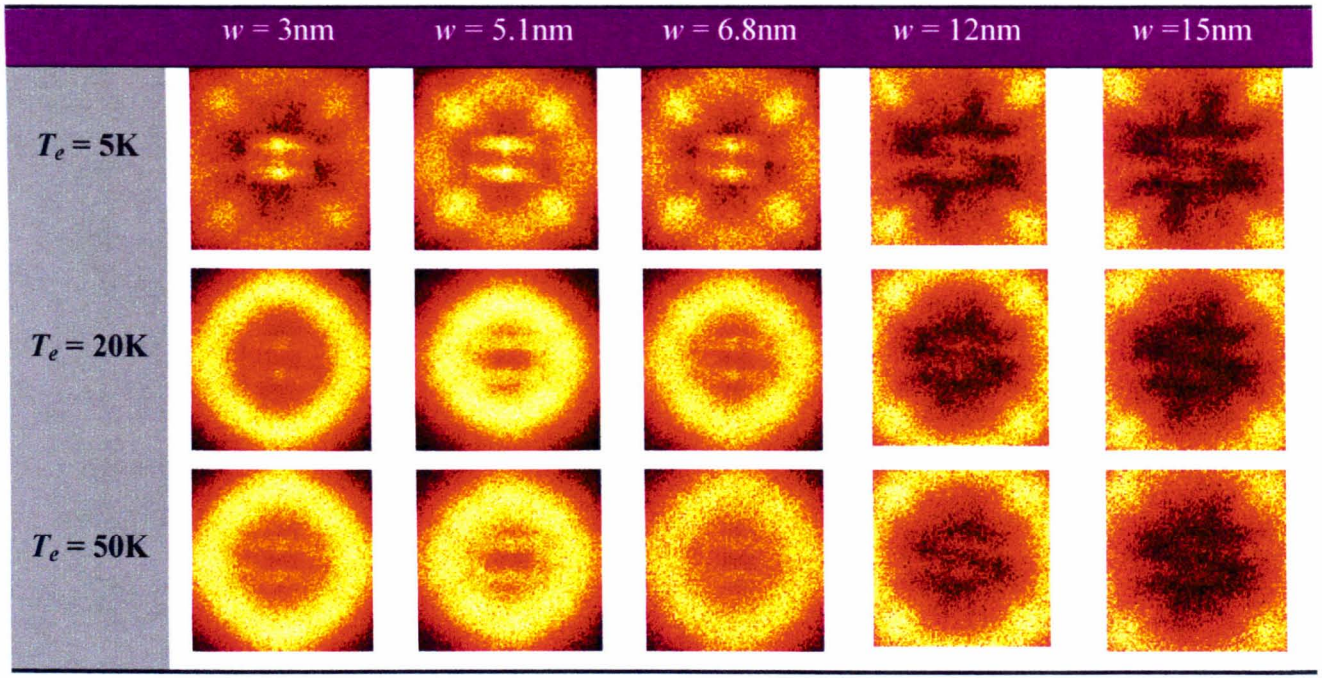

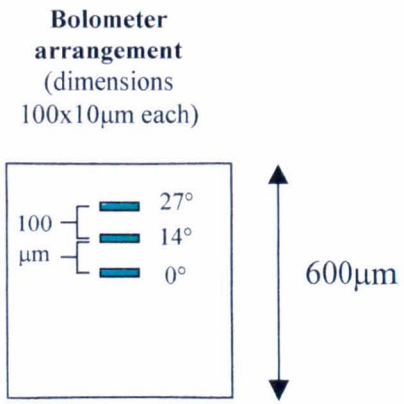

Figure 5.13 : Theoretically calculated phonon emission images from 120μm x 50μm 2DEG source at T_e = 5K, 20K, 50K for well widths used in experimental study.

Further evidence for the significance of the $1/a_0$ cutoff on the phonon spectra comes from comparison of the images for the different wells. Considering the reciprocal well width w^{-1}, it is seen that the wells are clustered into three groups, the 5.1nm and 6.8nm wells forming one group, the 12nm and 15nm wells forming another, while the 3nm well is separated from the others. This grouping is also seen in the angular phonon emission spectra depicted in the images.

The theoretical phonon energy images shown in *Figure 5.13* also indicate that the nature of the emission is expected to change significantly as a function of the angle to the normal of the 2DEG at which the phonon detector is positioned. By placing bolometers some distance along the [110] direction relative to the centre of the 2DEG device, the angular phonon response may be observed experimentally.

Figure 5.14 shows the emission from the 6.8nm quantum well for a sequence of input powers, as measured by the 14° bolometer. Comparing with the response of the opposite bolometer (*Figure 5.5)* an enhancement of the LA mode is observed. *Figure 5.15* shows the LA/(LA+TA) ratio of each well width as observed at the 14° bolometer, along with the theoretically predicted values. The trend of increased LA intensity with narrowing well width that was observed for the 0° bolometer is also seen in this case, though over a smaller range; the "baseline" LA emission is much greater at this angle, consistent with the predictions of phonon focusing theory; as the detector is moved from the [100] direction, a strong TA focusing plane, towards the [111] direction, where the LA is focused.

At the 27° bolometer, the LA mode is seen to strengthen still further, as the detector is positioned close to the focusing "ring" for DP-coupled LA emission (*Figure 3.14*). The total emission power, however, is seen to decrease, with the signal-to-noise ratio making accurate estimation of the LA/TA ratios difficult.

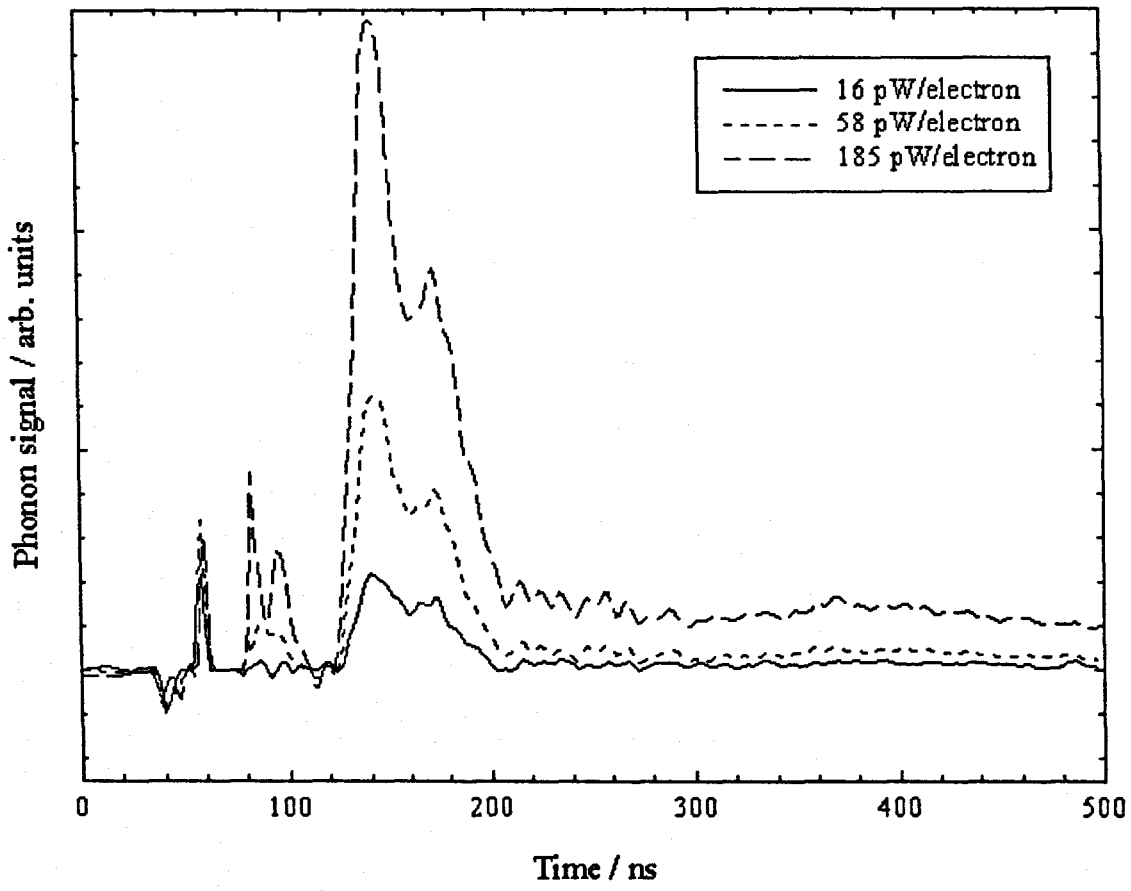

Figure 5.14 : Emission signal from 6.8nm quantum well, detected by 14° bolometer.

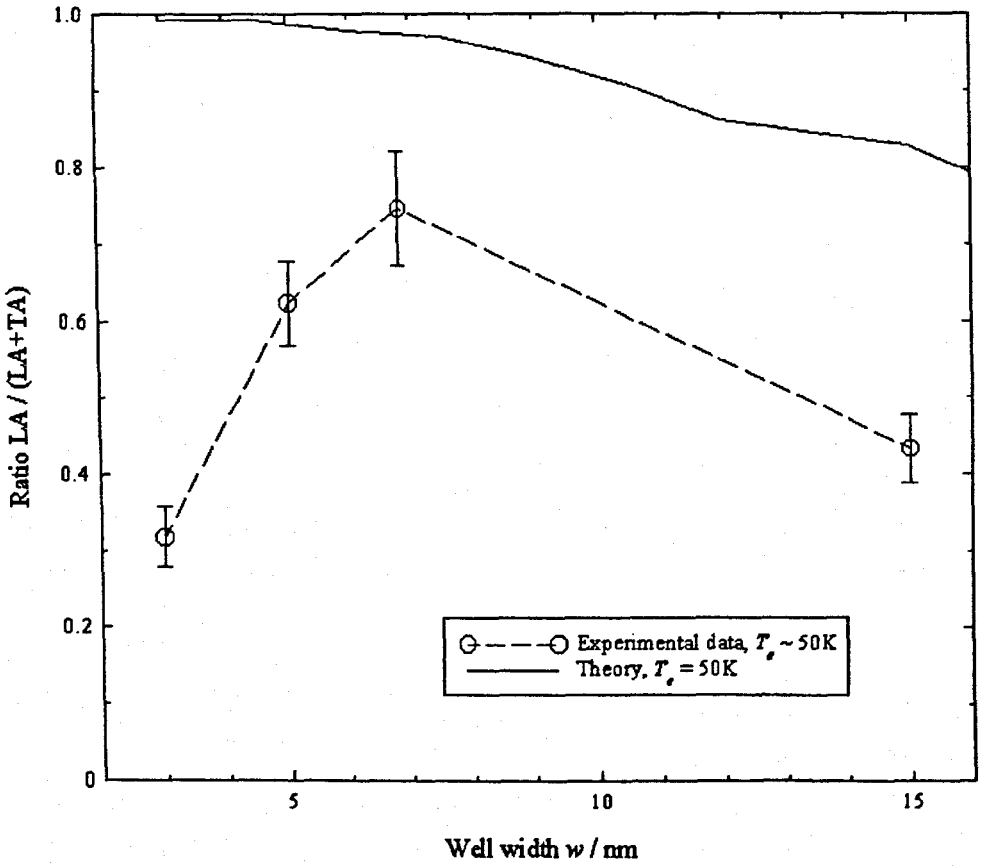

Figure 5.15: Experimentally measured LA/(LA+TA) ratio for detected phonon emission at T_e = 50K at 14° bolometer, compared to theoretical calculation.

The total detected phonon emission energy at both angular bolometers, especially the 27° bolometer, was found, in general, to be significantly lower than that detected at the opposite bolometer. This appears to contradict the predictions of theory, which show that for the 6.8nm quantum well, the total detected emission power should increase as the angle is moved towards the focused LA emission at around 30°. However, as the angle is widened, so the emission becomes more diffuse, with greater attenuation of the emitted phonons due to the longer path length between source and detector, with a subsequent widening of the "time window" in which ballistic phonons arrive at the detector. Sharp ballistic peaks are therefore not observed. It is also expected that there would be an increased probability of phonons being reflected on traversing the substrate and reaching the opposite surface, owing to their angle of inclination.

Figure 5.16 shows further theoretical calculations of the phonon energy emitted by the 6.8nm quantum well at T_e = 5K and T_e = 10K. The dimensions of the image are as in *Figure 5.13*. In each case, the overall energy image is shown, along with the images for DP-only coupling, PZ-only coupling, LA-only emission and TA-only emission.

For the T_e = 5K case, the effects of piezoelectric electron-phonon coupling can clearly be seen in the overall energy image. Transverse acoustic phonon emission arising from both DP- and PZ-coupling contributes to the central region of the image, close to the experimental detector.

At T_e = 10K, deformation potential coupling is already completely dominant. The signal arising from TA phonons in the overall composite image is much smaller than in the 5K case. Furthermore, as noted in the discussion of the angular dependence of emission, the transverse signal that can be observed

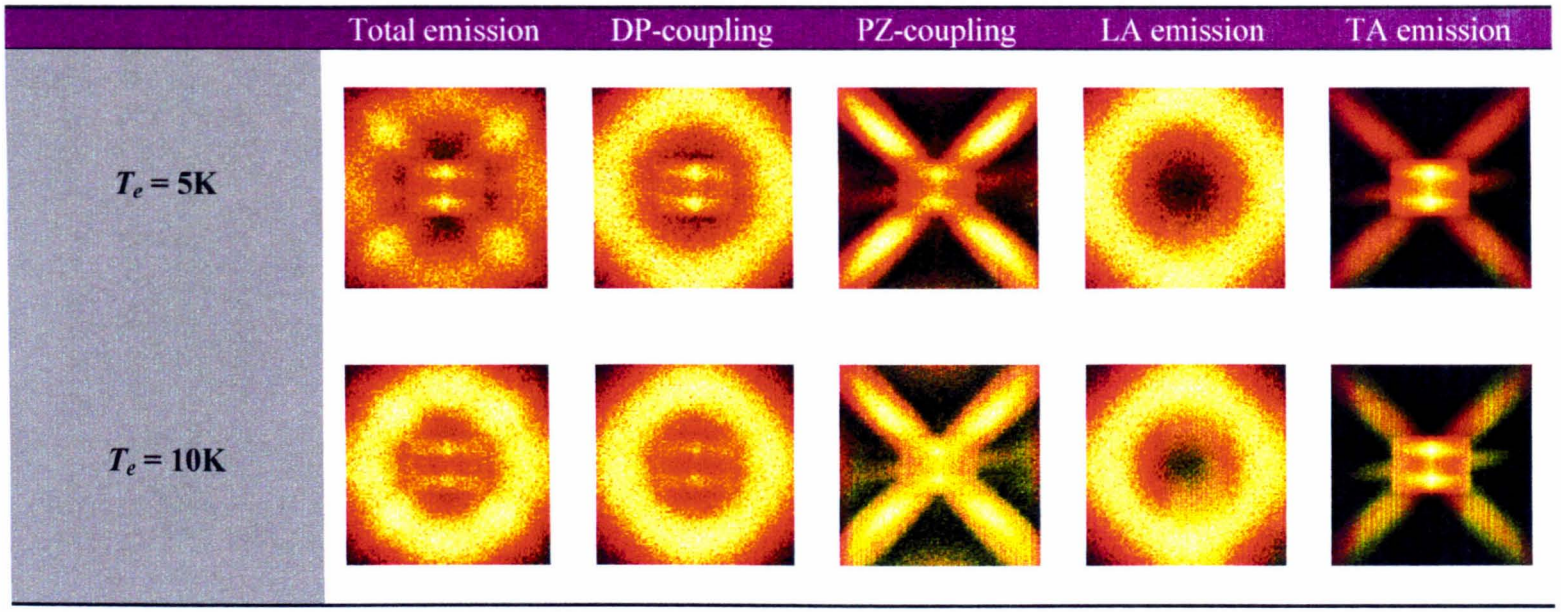

Figure 5.16: Breakdown of emission images into coupling mechanism and phonon modes for 6.8nm QW

has the character of deformation potential coupling.

5.3 Optic Phonon Emission

For electron temperatures below $T_e \sim 40$ K, it has been shown above that deformation-potential coupled acoustic phonon emission is the dominant energy relaxation process for a heated 2DEG with strong electron confinement, e.g. within a square potential well. Previous studies have shown that for systems with weaker electron confinement, e.g. 2DEG heterojunctions, acoustic phonon emission is again the main relaxation process, however the deformation potential coupling is suppressed, so that PZ-coupled TA phonon emission dominates the measured time-of-flight phonon signals.

At higher temperatures, the most prominent feature of the phonon signal is a broad pulse arriving shortly after the ballistic TA signal. This signal is believed to correspond to the emission of longitudinal optic (LO) phonons. Evidence for such emission comes from photoluminescence measurements of the electron energy relaxation rate in the temperature range $30\text{K} < T_e < 100\text{K}$ (Yang *et al.*, 1985), which showed an exponential dependence of the energy loss rate on T_e^{-1}.

Figure 5.17 shows heat pulse phonon emission signals for the $w =$ 6.8nm quantum well at $T_e < 50\text{K}$ and $T_e > 60\text{K}$, corresponding to excitation powers of 3pW and 300pW per electron respectively. The two signals have been normalised so that the total energy emitted into the ballistic LA and TA modes is the same in each case.

The effects of optic phonon emission are evident in the $T_e > 60\text{K}$ signal. The TA peak increases in relative amplitude and shifts to a later arrival time by about 5ns. The long tail that follows the TA peak is also increased in amplitude, compared to the lower power trace.

From Yang *et al.*, the expression for the energy relaxation rate due to optic phonon emission is:

$$P_e = \left(\frac{\hbar\omega_{LO}}{\tau}\right)\exp\left(\frac{-\hbar\omega_{LO}}{kT_0}\right)$$

The longitudinal optic phonons are short lived, rapidly down-converting to large-wavevector transverse acoustic modes, which propagate quasi-diffusively across the GaAs substrate. The LO phonon inverse scattering rate τ was measured to be 3.3ps by Hawker *et al.* (1992) for the case of a 2DEG heterojunction, having carrier density $N_s = 4.5 \times 10^{15}\text{m}^{-2}$ and 4.2K mobility $\mu = 20\ \text{m}^2\text{V}^{-1}\text{s}^{-1}$. The first optic down-conversion products arrive at the detector shortly after the main ballistic TA peak, with the remaining optic phonon energy contributing a long tail to the phonon signal.

The shift from acoustic- to optic-dominated phonon emission occurs due the exponential rise of LO phonon emission at electron temperature $T_e \sim 50\text{K}$. By comparison, the proportion of total emitted phonon power dissipated into acoustic emission is reduced as the electron temperature reaches 50K, due to a "saturation" of acoustic emission due to the $1/a_0$ and $2k_F$ emission cutoffs. At high temperatures T_e , the peak phonon wavevector q in the Planckian distribution shifts to higher values. The proportion of wavevectors that are smaller than the $1/a_0$ and $2k_F$ threshold wavevectors q_c is therefore decreased, resulting in an effective reduction in the phase space for the electron-acoustic phonon interaction above $T_e = 50\text{K}$.

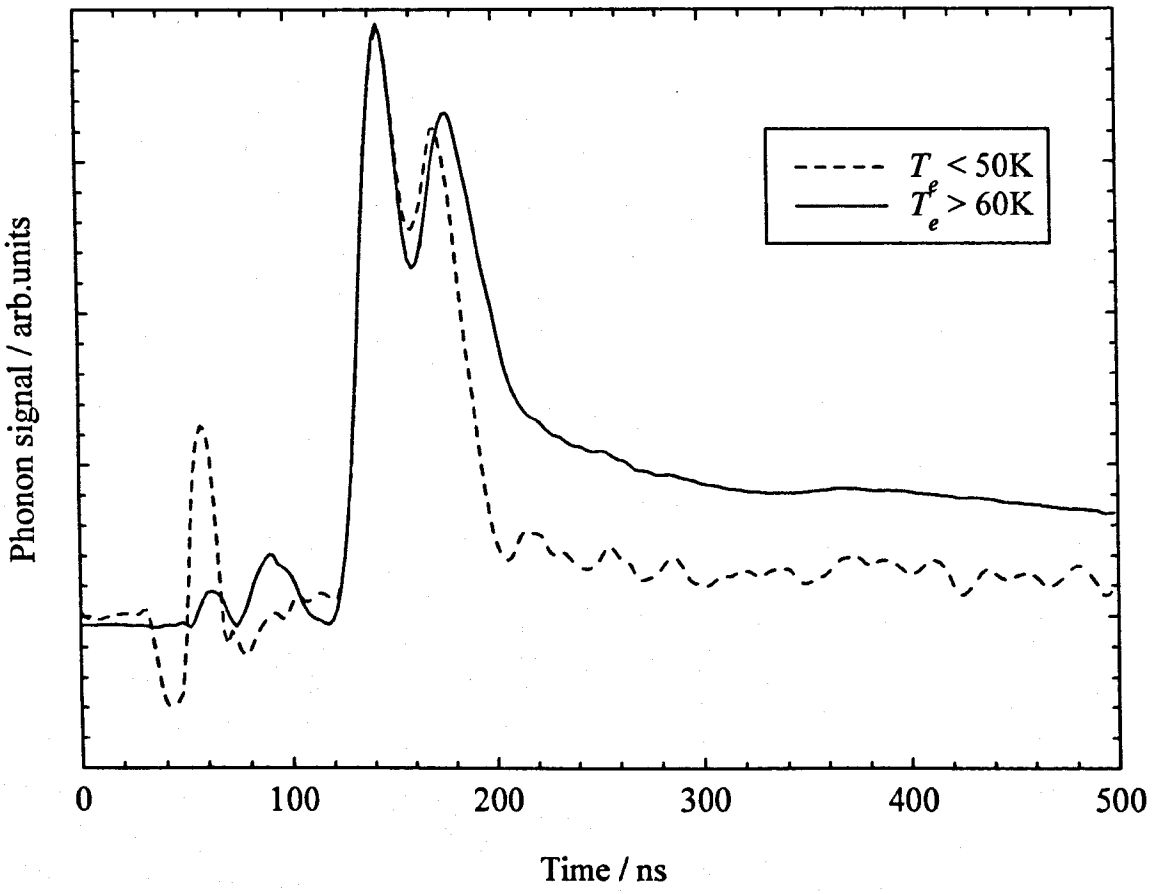

Figure 5.17 : Heat pulse signals for 6.8nm quantum well detected at 0° bolometer for electron temperatures $T_e > 60$K and $T_e < 50$K. The signals have been normalised so that the intensity into the ballistic LA mode is the same in each case.

Heat pulse measurements may be used to measure the power dissipation P_{opt} at which the onset of optic phonon emission occurs, by plotting the total energy relaxation rate into acoustic phonon emission, obtained by integrating the area underneath the time-of-flight phonon signal, as a function of heat pulse power P_{2DEG}. The onset of optic phonon emission is indicated by a large rise in the total energy relaxation rate of the 2DEG, as shown for the 6.8nm quantum well in *Figure 5.18*. For low input powers, the integrated phonon signal rises slowly, having no optic emission component. At the acousto-optic crossover power P_{opt}, the slope of the log-log graph becomes unity, indicating a linear dependence of the signal on heat pulse power.

From *Figure 5.18*, the crossover power for the 6.8nm quantum well is measured to be P_{opt} = 2.1pW per carrier. As discussed above, the emission of deformation-potential coupled acoustic phonons is increased in narrow wells, due to the stronger carrier confinement in the 2DEG which reduces the effect of the interaction cutoffs, to open up phase space for electron scattering. This increase in phase space would be expected to result in an associated increase in the crossover power P_{opt} at which optic emission, becomes the dominant phonon scattering process, with the magnitude of P_{opt} being pushed to a much higher value than that measured for a 2DEG heterojunction.

Strickland (1996) reported an increased optic crossover power for the case of a heated 2DHG heterojunction, at a power of P_{opt} = 50pW per carrier, as compared to the 5pW per carrier measured in a 2DEG heterojunction by Hawker *et al.* (1992). This increase was attributed to the higher carrier effective mass and thus stronger confinement in the 2DHG compared to a 2DEG heterojunction of similar parameters.

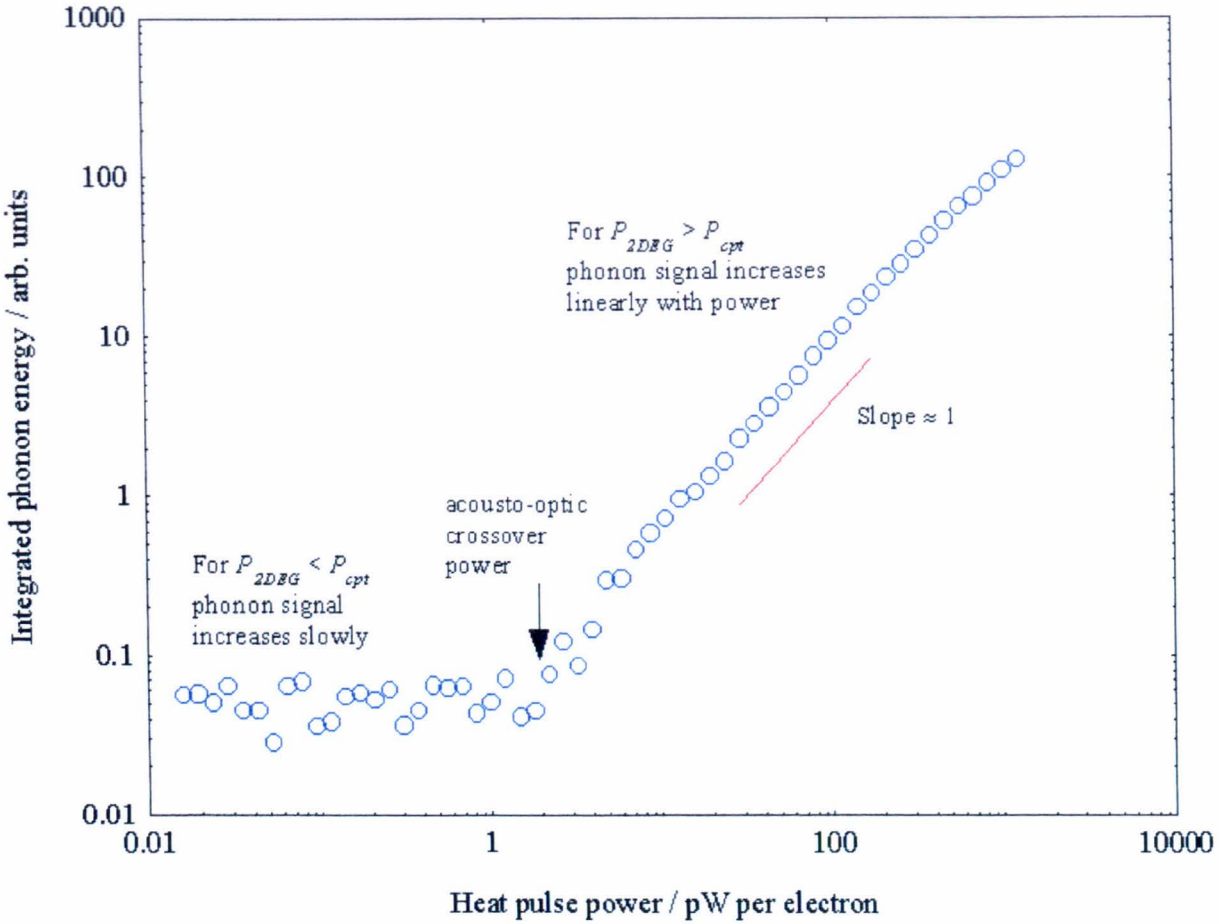

Figure 5.18: Total emitted phonon energy as a function of heat pulse power, showing the onset of optic phonon emission.

The measured crossover for the 6.8nm quantum well, P_{opt} = 2.1pW per carrier, therefore seems rather low, compared to the value reported by the Hawker group, considering the extra phase space for acoustic mode emission in the quantum well. This difference can however be attributed to differences in the method used to measure the crossover power. By selecting as the crossover the point at which the slope of the log-log graph of *Figure 5.18* first increases, the optic onset power is obtained. High resolution heat-pulse measurements of the crossover region by Pentland (2000) suggest that these first indications of optic phonon emission occur at a power about ten times lower than the point at which optic emission begins to become dominant, a value which had been traditionally assigned as the acousto-optic crossover.

Given this approximate rule of thumb, it is seen that the measured values of P_{opt} for the quantum well result in the expected pushing of the acousto-optic crossover to higher powers as the acoustic emission cutoffs are weakened. In the experiments of Strickland, the Hawker group and other previous studies (e.g. Cross *et al.*, 1999), the power identified as P_{opt} can now be more correctly defined as the power at which optic emission becomes the dominant energy relaxation process, rather than the power at which LO phonons are first observed.

Figure 5.19 shows the variation of the acousto-optic crossover the as a function of well width for the quantum well samples studied in this work. The optic onset power has been determined following the technique of Pentland (2000). The crossover power is seen to shift to higher powers as the well width is narrowed. This provides further evidence that in narrow quantum wells, acoustic phonon emission becomes much more effective, owing to the "opening up" of phase space due to the weakening of the $1/a_0$ cutoff.

As a rough approximation, neglecting the effects of electron impingment into the GaAs/(AlGa)As barriers at very narrow well widths, the volume of phase space for acoustic scattering increases as w^{-1}, due to the relaxation of the $1/a_0$ cutoff as w is reduced. At narrow well widths, as

discussed in Chapter 3, the finite confining potential causes an effective widening of the quantum well, and consequently the acoustic phonon emission rate is reduced. The w^{-1} dependence will therefore weaken as $w \to 0$.

The energy loss rate at electron temperatures below 50K also depends on the energy spectrum of the emitted phonons, which is dominated by a peak at the cutoff at $\hbar\omega = \frac{\hbar v_s}{w}$. This second w^{-1} dependence will also weaken as the well becomes very narrow and the phonon energy peak approaches the maximum acoustic phonon frequency.

From these considerations, it may be suggested that the optic crossover power may vary as $P_{opt} \sim w^{-2}$, except at narrow well widths, where the dependence will gradually weaken and tend to a limiting constant value of P_{opt} as the well width $w \to 0$.

From *Figure 5.19*, it is seen that the experimental data and a theoretical calculation of the total acoustic phonon emission power into all angles, wavevectors and modes at 50K agree well with the predicted trend, approximating to $P_{opt} \sim w^{-2}$ for well widths $w > 5$nm, with P_{opt} levelling off as the well is narrowed further. Clearly here it is appropriate to compare the theoretical calculation of emission with the newly defined (onset) value of P_{opt} rather than the traditional (dominant) value, as the calculation does not include an optic contribution.

The experimentally measured values of P_{opt} may therefore be said show good numerical agreement with the theoretical calculation of the total acoustic phonon emission power at $T_e = 50$K for each well. As the well width is increased further, it would be expected that bulk-phonon behaviour should take over, i.e. the optic crossover will tend to a constant value. Further experimentation with wider wells would be necessary to confirm this, especially in view of the somewhat low experimental crossover power measured for the 15nm well.

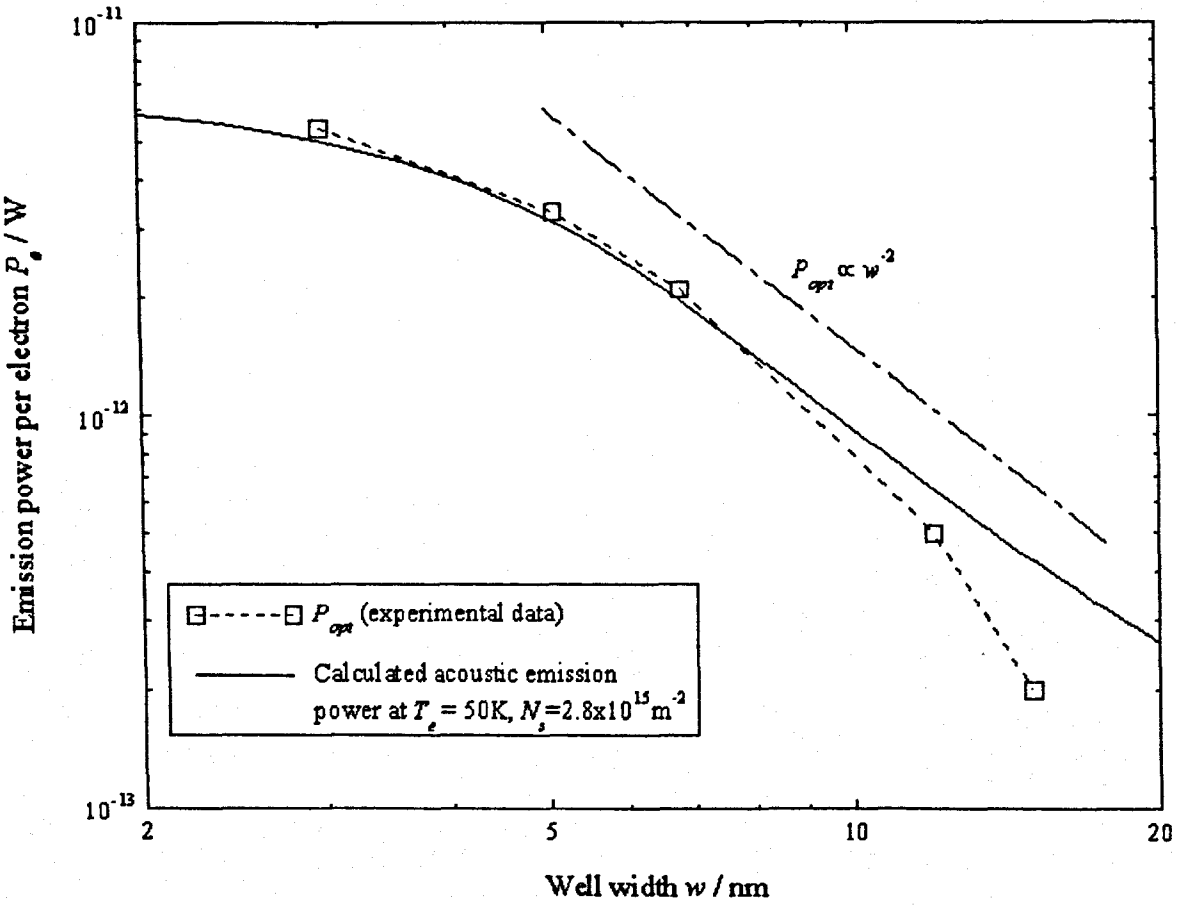

Figure 5.19: Variation of acousto-optic crossover power P_{opt} as a function of well width. Also plotted is the theoretically calculated total acoustic emission power at T_e = 50K.

5.4 Summary

The experiments presented clearly show the significant effect the vertical confinement of the carriers has on the carrier-acoustic phonon coupling. In contrast to heterojunction devices, significant longitudinal acoustic phonon emission is detected from heated 2DEG quantum well devices. The amount of LA emission as a proportion of the total acoustic (LA+TA) emission is larger in the narrower wells. This leads to the conclusion that the weak LA emission in heterojunction and wide wells is partly due to the suppression of the emission of large wavevector (DP coupled) phonons because of the more severe perpendicular momentum cutoff in these systems.

The absence of LA emission in heterojunction devices can therefore be explained primarily in terms of the electron confinement in such devices, which results in a form factor that cuts off the electron-phonon interaction at low phonon wavevectors before DP coupling becomes important. In quantum wells, significant LA emission is observed because the cutoff is much less severe.

Furthermore, from theoretical predictions, it is suggested that the deformation potential also couples most of the emitted TA phonons that are detected at the bolometers in the experiment. Theoretical simulations show that these phonons are largely slow-transverse in character. The piezoelectric interaction couples mainly to fast-TA modes, which are emitted in a diagonal-arm pattern and do not contribute strongly to the detected emission.

At angles further away from the 2DEG normal, the effect of the $1/a_0$ perpendicular cutoff is still evident, from the trend of increasing LA emission as the well width is narrowed. However, this trend is less striking than at the 0° bolometer, as LA focusing affects the emission at wider angles, "washing out" the dependence on the $1/a_0$ cutoff to some extent.

The onset power P_{opt} at which the dominant 2D electron energy relaxation mechanism changes over to optic phonon emission has also been measured as a function of the quantum well width w. It was found that P_{opt} is increased as the well width is narrowed, due to the increased phase space for acoustic phonon emission in these devices. At well widths $w > 5$nm, a relation $P_{opt} \sim w^{-2}$ has been proposed theoretically and experimentally verified, with close numerical agreement between calculated and measured values of P_{opt}. For narrower well widths, it is suggested that P_{opt} tends towards a constant minimum value.

Chapter 6
Conclusions

6 Conclusions

This thesis has provided a detailed account of the effects of electron confinement on the coupling of electrons to phonons in two dimensional electron gases at low temperatures.

The experimental study of the 2D quantum wells showed a significant longitudinal acoustic phonon response for all of the devices studied: this can be attributed to the generally weaker $1/a_0$ effect in QWs compared to heterojunctions. As the well width (effectively the thickness of the quasi-2D sheet) was narrowed, the proportion of LA phonons in the signal increased. At very low well widths (< 4nm) where the electron wavefunction leaks significantly into the barriers of the potential well, the LA proportion of emission is reduced.

As the heat pulse power P_{2DEG} is varied, the LA/(LA+TA) ratio is observed to change, with the dependence varying strongly as a function of well width. For narrow quantum wells, the LA proportion of emission increases with increasing P_{2DEG}, as the peak phonon wavevector shifts to higher values without being affected by the $1/a_0$ cutoff. For wider wells, the opposite dependence is observed: as the heat pulse power is decreased, the LA/(LA+TA) ratio increases. Here the emission is strongly affected by the $1/a_0$ cutoff; reducing the power therefore increases the proportion of phonons in the distribution having wavevectors below the cutoff, resulting in an enhanced LA proportion of emission.

A similar observation is found when studying the transition from acoustic to optic phonon emission. The crossover power P_{opt} is pushed to higher values at low well widths. This can be attributed to a greater number of "pathways" for acoustic phonon emission at low well widths due to the lifting of the suppression of the emission caused by the $1/a_0$ cutoff. For well widths w > 5nm, a $P_{opt} \sim w^{-2}$ dependence of the crossover power is found and explained in terms of the energy and momentum restrictions of the system. Furthermore, the experimental measurements of the optic crossover show the same dependence as theoretical calculations of the total disspiated power into acoustic phonon modes at T_e = 50K.

This result contrasts with work by Al Jawhari *et al.* (1999), which proposes that the dominant mechanism for electron energy relaxation from a hot 2DEG for electron temperatures 20K < T_e < 70K is the exictation of coupled plasmon-optic modes. It is argued that these modes couple to electrons an order of magnitude more strongly than acoustic phonons in this regime, accounting for the discrepancy between theoretically calculated and experimentally measured values of P_{opt} based on acoustic emission only. As discussed in *5.3* above, however, doubt has been cast upon traditional methods of measuring the optic crossover power by Pentland (2000). By taking the first indication of LO emission as the crossover, values of P_{opt} result that match the theory far more closely, as in *Figure 5.19*.

Das Sarma et al. (1988) precict that for a 2DEG quantum well, the crossover between this coupled-mode and optic emission should be essentially independent of well width. The observed w^{-2} dependence of the optic crossover thus provides strong evidence that the coupled plasmon-optic mode is not seen in this work. Further investigation is therefore required to fully understand the 2DEG energy relaxation processes in this temperature regime.

The computer modelled simulation of the theory of the 2DEG system adds much understanding to the experimental results, and illustrates in particular the importance of including in the calculation the effects of screening, matrix element anisotropy, the non-infinite potential well barriers and the finite thickness of the 2D sheet. In each of these cases, particular reference has been made to features in the experimental data that can be uniquely attributed to the effects of each factor. Where specific predictions have been made by the model, e.g. of the optic crossover power P_{opt}, good agreement was found with the experimental data.

In summary, the objectives of the research have been largely accomplished, with the experimental and theoretical findings contributing to a new level of understanding of the energy relaxation processes of 2D electrons in semiconductors at low temperatures.

Appendix A:

Derivation of bound-state form factor for square quantum well

To obtain the bound-state form factor (Toombs *et al.*, 1987) defining the restriction on the z-momentum of an emitted phonon in the electron-phonon interaction, the transition matrix element describing the overlap integral between the initial and final k-states, $M_k^{k'(q,\lambda)} = \int \Psi_{k'}^* V_{e-p} \Psi_k dr$ must be integrated in the z-direction.

For a heterojunction, assuming an approximately triangular confining potential:

$$\Psi_0(z) = \left(\frac{1}{2a_0^3}\right)^{1/2} z \exp(-z/2a_0)$$

where $3a_0$ is the average separation of electrons from the heterointerface.

The exponential form of the ground-state wavefunction makes it a trivial task to perform the integration to obtain the form factor in this case.

For a quantum well, assuming an infinite square potential:

$$\Psi_0(z) = \sqrt{\frac{2}{w}} \sin\left(\frac{\pi z}{w}\right)$$

where w is the quantum well width.

Solving the matrix element integral in this case is considerably more complex, eventually yielding:

$$\left|F(q_z)^2\right| = K^2\left(\sin^2 K + (1-\cos K)^2\right)$$

$$\text{where } K = \left(\frac{1}{q_z w}\right) - \left(\frac{1}{2(q_z w + 2\pi)}\right) - \left(\frac{1}{2(q_z w - 2\pi)}\right)$$

The full derivation is given here:

$$M_k^{k'(q,\lambda)} = \int \Psi_{k'}^{*} V_{e-p} \Psi_k \, dr$$

where $\Psi_k = \Psi_0 \exp(ik \cdot r)$. Since $k - k' = q$:

$$M_k^{k'(q,\lambda)} = \int V_{e-p} \Psi_0^{\,2} \exp(iq_x x)\exp(iq_y y)\exp(iq_z z)\, dr$$

The integral can be split into its in-plane and perpendicular components (the former giving rise to the $2k_F$ cutoff). Solving for the latter by substituting the above expression for Ψ_0 in the case of an infinite square well and expanding $\exp(iq_z z)$ as a sum of sines and cosines, the following is obtained:

$$F(q_z) = \left(\frac{2}{w}\right)\int_0^w \sin^2\left(\frac{\pi z}{w}\right)(\cos q_z z + i \sin q_z z)\, dz$$

The $\sin^2 x$ term can be be replaced using the trigonometric identity: $\sin^2 x = \frac{1}{2}(1 - \cos 2x)$.

Splitting the expression into its real and imaginary components gives:

Real: $\frac{1}{w}\int_0^w \cos q_z z - \cos q_z z \cos\left(\frac{2\pi z}{w}\right) dz$

Imaginary: $\frac{1}{w}\int_0^w \sin q_z z - \sin q_z z \cos\left(\frac{2\pi z}{w}\right) dz$

Another pair of trigonometric substitutions enables the double cosine product in each expression to be replaced:

$$\cos A \cos B = \frac{\cos(A+B)+\cos(A-B)}{2} \quad \sin A \cos B = \frac{\sin(A+B)+\sin(A-B)}{2}$$

For the real term, three simple cosines remain, to be integrated. For the imaginary term, three simple sines result.

The result of these integrations are:

Real term: $\frac{1}{w}\sin q_z w\left[\frac{1}{q_z} - \frac{1}{2\left(q_z+\frac{2\pi}{w}\right)} - \frac{1}{2\left(q_z-\frac{2\pi}{w}\right)}\right]$

Imaginary term: $\frac{1}{w}(1-\cos q_z w)\left[\frac{1}{q_z} - \frac{1}{2\left(q_z+\frac{2\pi}{w}\right)} - \frac{1}{2\left(q_z-\frac{2\pi}{w}\right)}\right]$

Squaring and adding, the final result is obtained:

$$\left|F(q_z)^2\right| = K^2\left(\sin^2 K + (1-\cos K)^2\right)$$

where $K = \left(\frac{1}{q_z w}\right) - \left(\frac{1}{2(q_z w+2\pi)}\right) - \left(\frac{1}{2(q_z w-2\pi)}\right)$

References

A.V.Akimov, L.J.Challis and C.J.Mellor, *Physica B,* **169,** 563 (1991)

H.Al Jawhari, A.G.Kozorezov,M.Sahraoui-Tahar, J.K.Wigmore and C.D.W.Wilkinson, *Physica B,* **263-264,** 211 (1999)

T.Ando, A.B.Fowler and F.Stern, *Rev.Mod.Phys.*, **54,** 437 (1982)

J.Bardeen and W.Shockley, *Phys.Rev.*, **80** 72 (1950)

M.A.Chin, V.Narayanamurti, H.L.Stormer and J.C.M.Hwang, in *Phonon Scattering in Condensed Matter,* eds. W.Eisenmenger, K.Lassmann and S.Döttinger (Springer: Berlin), 328 (1984)

A.J.Cross, A.J.Kent, P.Hawker, D.Lehmann, Cz.Jasiukiewicz and M.Henini, *Physica B,* **263-264,** 526 (1999)

S.Das Sarma, J.K.Jain and R.Jalabert, *Phys.Rev.B,* **37,** 4560 (1988)

A.G.Every, *Phys.Rev.Lett.*, **42,** 1065 (1979)

A.G.Every, *Phys.Rev.B,* **22,** 1746 (1980)

A.G.Every and A.K.McCurdy, *Phys.Rev.B,* **36,** 1432 (1987)

F.F.Fang and A.B.Fowler, *J.Appl.Phys.*, **41** 1825 (1970)

W.Gancza and T.Paszkiewicz, *Comp.Phys.Commun.*, **85,** 423 (1995)

I.Gorczya and J.Krupski, *Phys.Rev.B,* **52,** 11248 (1995)

P.Hawker, *PhD thesis,* University of Nottingham (1990)

P.Hawker, A.J.Kent, O.H.Hughes and L.J.Challis, *Semicond.Sci.Technol.*, **7** B29 (1992)

P.Hawker, A.J.Kent, N.Hauser and C.Jagadish, *Semicond.Sci.Technol.*, **10,** 601 (1995)

P.Hawker, C.Jagadish and M.R.Melloch, *Physica B*, **219 & 220**, 62 (1996)

R.A.Hopfel, E.Vass and E.Gornik, *Solid State Commun.* **49**, 501 (1984)

A.R.Hutson and D.C.White, *J.Appl.Phys.*, 33, 40 (1962)

Cz.Jasiukiewicz and V.Karpus, *Semicond.Sci.Technol.*, **11**, 1777 (1996)

Cz.Jasiukiewicz, D.Lehmann, A.J.Kent, A.J.Cross and P.Hawker, *Physica B*, **263-264**, 183 (1999)

A.J.Kent, A.J.Cross, P.Hawker and M.Henini, *Phys.Stat.Sol.*, **204**, 230 (1997)

A.J.Kent, in *Hot Electrons in Semiconductors: Physics and Devices*, ed. N.Balkan (Oxford University Press, Oxford), 81 (1998)

P.G.Klemens, in *Solid State Physics*, vol 7, eds. F.Seitz and D.Turnbull (Academic Press, New York) (1958)

H.J.Maris, *J.Acoust.Soc.Am.*, **50**, 812 (1971)

A.Naylor, *PhD thesis*, University of Nottingham (1998)

G.A.Northrop, *Comp.Phys.Commun.*, **28**, 103 (1982)

I.A.Pentland, *PhD thesis,* University of Nottingham (2000)

M.Rothenfusser, L.Köster and W.Dietsche, *Phys.Rev.B,* **34**, 5518 (1986)

J.Shah, A.Pinczuk, H.L.Stormer,A.C.Gossard and W.Weigmann, *Appl.Phys.Lett.* **42**, 55 (1983)

F.Stern and W.E.Howard, *Phys.Rev.*, **163**, 816 (1967)

K.R.Strickland, R.E.George, M.Henini and A.J.Kent, *Semicond.Sci.Technol.*, **9**, 786 (1994)

R.E.Strickland, *PhD thesis*, University of Nottingham (1996)

S.Tamura, *Phys.Rev.B*, **30**, 849 (1984)

B.Taylor, H.J.Maris and C.Elbaum, *Phys.Rev.Lett.*, **23**, 416 (1969)

G.A.Toombs, F.W.Sheard, D.Neilson and L.J.Challis, *Solid State Commun.*, **64**, 577 (1987)

F.T.Vasko and V.V.Mitin, *Phys.Rev.B*, **52**, 1500 (1995)

E.Vass, *Solid State Commun.*, **61**, 127 (1987)

A.J.Vickers, *Phys.Rev.B*, **46**, 13315 (1992)

R.J.von Gutfeld and A.H.Nethercot Jr, *Phys.Rev.Lett.*, **12**, 641 (1964)

W.Walukiewicz, *Phys Rev.B*, **37**, 8530 (1988)

A.K.M.Wennberg, S.N.Ytterboe, C.M.Gould, H.M.Bozler, J.Klem and H.Morkoç, *Phys.Rev.B*, **34**, 4409

A.Wixforth, J.Scriba, M.Wassermeir, J.P.Kotthaus, G.Weimann and W.Schlapp, *Phys.Rev.B*, **40**, 7874 (1989)

C.H.Yang, J.M.Carson-Swindle, S.A.Lyon and J.M.Worlock, *Phys.Rev.Lett.*, **55**, 2359 (1985)

Z.Xin,F.F.Ouali,L.J.Challis,B.Salce and T.S.Cheng, *Physica B*, **220**, 56 (1996)

Y.Zheng, T.Lu, Y.Wang, X.Wu, C.Zhang and W.Su, *Semicond.Sci.Technol.*, **12**, 296 (1997)